



Contents lists available at ScienceDirect

Progress in Retinal and Eye Research

journal homepage: www.elsevier.com/locate/preteyeres

Adaptive optics imaging of the human retina

Stephen A. Burns^{*,1}, Ann E. Elsner¹, Kaitlyn A. Sapoznik¹, Raymond L. Warner¹, Thomas J. Gast¹

800E. Atwater S, School of Optometry, Indiana University, Bloomington, IN, United States

ARTICLE INFO

Keywords:

Retina
Imaging
Retinal degenerations
Vascular disease
Ophthalmoscopy
Photoreceptors
Blood flow

ABSTRACT

Adaptive Optics (AO) retinal imaging has provided revolutionary tools to scientists and clinicians for studying retinal structure and function in the living eye. From animal models to clinical patients, AO imaging is changing the way scientists are approaching the study of the retina. By providing cellular and subcellular details without the need for histology, it is now possible to perform large scale studies as well as to understand how an individual retina changes over time. Because AO retinal imaging is non-invasive and when performed with near-IR wavelengths both safe and easily tolerated by patients, it holds promise for being incorporated into clinical trials providing cell specific approaches to monitoring diseases and therapeutic interventions. AO is being used to enhance the ability of OCT, fluorescence imaging, and reflectance imaging. By incorporating imaging that is sensitive to differences in the scattering properties of retinal tissue, it is especially sensitive to disease, which can drastically impact retinal tissue properties.

This review examines human AO retinal imaging with a concentration on the use of the Adaptive Optics Scanning Laser Ophthalmoscope (AOSLO). It first covers the background and the overall approaches to human AO retinal imaging, and the technology involved, and then concentrates on using AO retinal imaging to study the structure and function of the retina.

1. Introduction and background

Adaptive Optics (AO) retinal imaging is changing the way we look at the retina in an intact living eye. AO retinal imaging can provide optical resolutions of 2 μm or less in the living human eye and this resolution is sufficient to make measurements of cellular and sub-cellular details of normal retina structure and function that were previously only achieved in either post-mortem tissue (Fig. 1) or in non-human physiological preparations. Further, AO retinal imaging is a powerful tool for the investigation of disease mechanisms and is providing candidate biomarkers for more sensitive outcome measures for clinical interventions. AO retinal imaging has been developing over a number of years, and despite steady increases in the use of a commercial AO system and growing number of research groups now providing research grade data, penetration into widespread clinical use faces a number of remaining hurdles (Marcos et al., 2017). This review concentrates on human retinal imaging with AO, and the main thrust is on using the Adaptive Optics Scanning Laser Ophthalmoscope (AOSLO) to make these measurements. Complementary imaging modalities and a comparison of the unique capabilities, along with sample findings, are also briefly described.

1.1. Background

Early measurements of the *in vivo* optical properties of retinal tissues were based on the careful analysis of spectral and directional reflectance averaged over 1–2 degrees of retina (Berendschot et al., 2003, 2010; Burns et al., 1995b; Delori, 1988; Delori and Pflibsen, 1989; Krauskopf, 1965; Rushton, 1958). These measurements provided insights into the structure and physiology of the retina, allowing construction of detailed models of light-tissue interaction in the retina, but did not provide information at smaller scales that could readily be related to local retinal changes in disease. The development of imaging based techniques for studying retinal reflectance was developed during the 1980's, first with the development of multi-wavelength video reflectometers for measuring photopigment bleaching and regeneration (Faulkner and Kemp, 1984), and then with the development of the scanning laser ophthalmoscope (SLO) by Webb and colleagues (Mainster et al., 1982; Webb et al., 1980). An early alternative term for the SLO was the laser scanning fundus image (LSF) (Plesch et al., 1987) and the laser scanning tomographic scanner (Dreher et al., 1989), but modern systems use a wide variety of light sources, including non-laser based sources such as superluminescent diodes (SLDs) and the SLO terminology is used as a generic term for these systems. The SLO,

* Corresponding author.

E-mail address: staburns@indiana.edu (S.A. Burns).¹ Percentage of work contributed by each author in the production of the manuscript is as follows: Burns, 75%; Elsner 10; Gast 5%; Sapoznik 5%; Warner 5%.<https://doi.org/10.1016/j.preteyeres.2018.08.002>

Received 4 June 2018; Received in revised form 22 August 2018; Accepted 24 August 2018

1350-9462/ © 2018 The Authors. Published by Elsevier Ltd. This is an open access article under the CC BY-NC-ND license (<http://creativecommons.org/licenses/by-nc-nd/4.0/>).

Abbreviations

AO	Adaptive optics	LCD	Liquid crystal display
AO-OCT	Adaptive optics optical coherence tomography	MEMS	Microelectromechanical systems
AOSLO	Adaptive optics scanning laser ophthalmoscope	NA	Numerical aperture
CAO	Computational adaptive optics	OCT	Optical coherence tomography
CCD	Charge coupled device	OCTA	Optical coherence tomography angiography
CMOS	Complementary metal oxide semiconductor	PSF	Point spread function
CNS	Central nervous system	ROI	Region of interest
cSLO	Confocal scanning laser ophthalmoscope	RPE	Retinal pigment epithelium
FFT	Fast Fourier transform	SAO	Sensorless adaptive optics
HAO	Hardware adaptive optics	SH	Shack Hartmann wavefront sensor
LC	Liquid crystal	SLO	Scanning laser ophthalmoscope or scanning light ophthalmoscope

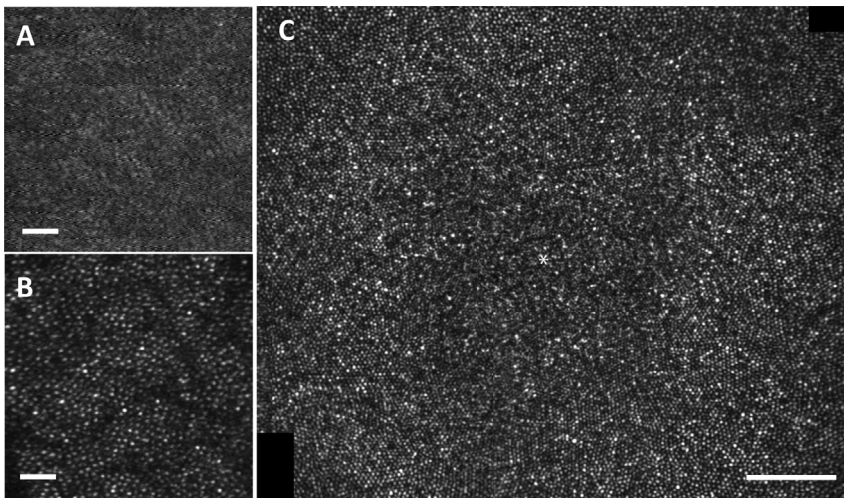


Fig. 1. An example of AOSLO image of the retina. A: A small region of parafoveal retina imaged with an AOSLO that has been adjusted for best focus but without adaptive optics compensation of high order aberrations. While some cones are visible as low contrast spots, not all are visible. B: The same region of the retina, with the AO control loop activated, showing all cones within this region. C: A montage of foveal confocal AOSLO images showing the cone mosaic across the central retina. The location of highest cone density is marked with an asterisk. All scale bars 50 μm .

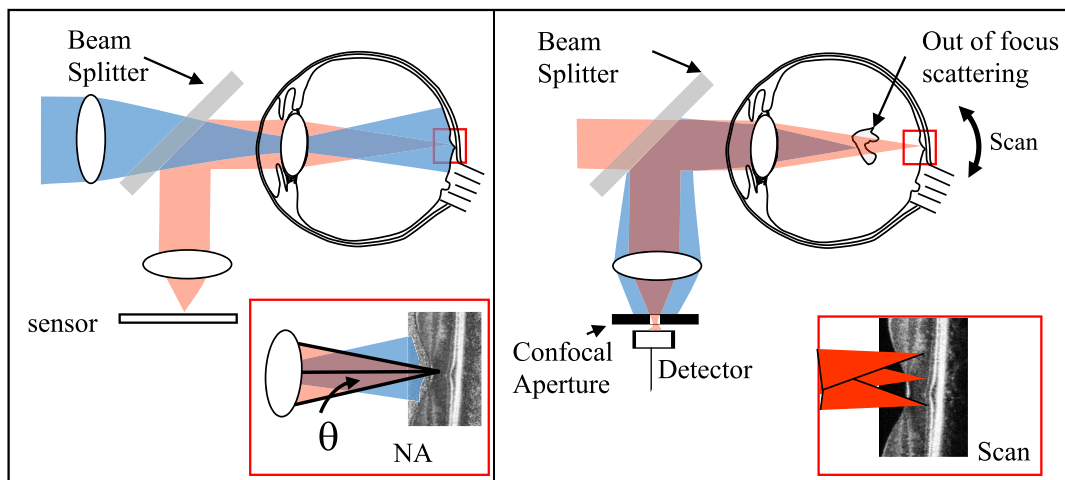


Fig. 2. A schematic comparison of flood illuminated and scanning confocal imaging systems. Left: In a flood illuminated system the entire region of interest of the retina is illuminated simultaneously (blue). The illumination light enters the eye through a relatively small region of the pupil. Light returning from the retina (pink) is passed through the optical system and imaged onto an areas sensor, such as a camera, optically conjugate to the plane of focus. Light scattered within the eye (not shown), falls on the camera, but is out of focus. Left Inset: Resolution for a diffraction limited imaging system is controlled by the angle (θ) the pupil subtends with respect to the retina, that is the sine of the radius of the pupil divided by the distance between the retina and pupil. Right: a confocal imaging system illuminates the retina by scanning a small spot of light focused onto the retina (inset). Light returning from the sample is then separated from the input light by a beam splitter, and refocused onto a confocal aperture. Because the confocal aperture is optically conjugate to the point of focus of the imaging beam, all of the light backscattered from the focus of the beam is re-imaged at the aperture and therefore passes through the aperture to the detector, generating a series of signals, each corresponding to a particular retinal location, and thus forms an image. Light scattered from objects that lie elsewhere (blue) is not focused at the aperture and does not contribute to the image. Thus a confocal system provides “optical sectioning” and increased contrast, being insensitive to out of focus light. Right Inset: To create an image of the entire region of interest the imaging system scans the retina, building up a view of the retina one point at a time.

because it scanned a focused beam across the retina, could use highly sensitive detectors, such as photomultiplier tubes (PMTs). The use of scanning to sweep a small focused spot across the retina had the additional advantage of restricting the illumination of the retina at any point in time to a single retinal region, improving control of scattered light (Fig. 2) and thus further improving on the precision of reflectance measurements. The development of the confocal SLO (cSLO), by introducing a retinal conjugate stop in the detection channel (Fig. 2, see below) allowed further control of the influence of scattered light, allowing the experimenter to choose images based on direct backscatter or from multiply scattered light (Elsner et al., 1996, 1998b, 2000, 2001). This improved control further enhanced measurement of photopigment and other retinal pigments (Elsner et al., 1992b; Elsner et al., 1996; Norren and van der Kraats, 1989). However the resolution of these imaging systems, while an improvement over spot or film reflectometers, were still not able to provide cellular level details, due to the limitations of resolution imposed by the optical quality of the eye.

1.2. Resolution

Ideally the resolution of an imaging system is set by the numerical aperture of the system

$$NA = n \sin(\theta) \quad (1)$$

where NA is the numerical aperture, n is the index of refraction of the medium, and θ is the angle subtended by the distance from the pupil center to the pupil margin as viewed from the retina (Fig. 2). That is, it is the angle that the distance from the pupil center to the edge subtends when viewed from the retina. For the eye the NA is about 0.23 for a maximally dilated pupil. For such a system the theoretical optical resolution according to the Rayleigh criterion is then determined by the pupil size, wavelength, and focal length

$$r = 0.61\lambda/NA \quad (2)$$

where r is the resolution, λ the imaging wavelength, and NA is the numerical aperture. A confocal system can improve on this somewhat due to the re-imaging of the tissue onto an aperture (Sredar et al., 2018; Webb, 1996; Wilson and Carlini, 1987).

1.3. Optical aberrations of the optics of the human eye

While equations (1) and (2) indicate that for a near infrared wavelength the human pupil size limits the achievable lateral resolution to about $2\ \mu\text{m}$, this limit is not reached because the eye is not diffraction limited even for monochromatic light.

The inability to provide diffraction limited performance arises from the presence of optical imperfections in the eye. These imperfections, termed optical wavefront aberrations, mean that for an eye focused at distance, parallel rays of light entering the eye at different pupil positions strike the retina at different retinal locations. That is, a distant light source is blurred due to the presence of monochromatic wavefront aberrations. The existence of these aberrations has been recognized since the 1800's (Helmholtz, 1866). Campbell and Green demonstrated that monochromatic wavefront aberrations degraded resolution in the human eye for pupil diameters larger than about 2 mm (Campbell and Green, 1965). Because the resolution of a diffraction limited optical system is proportional to the numerical aperture of the optical system (equation (2)), this limitation of resolution by aberrations present for pupil sizes larger than 2 mm is significant (Donnelly and Roorda, 2003). Increasing the pupil size from 2 mm to 8 mm would increase the resolution of a diffraction limited eye by a factor of 4x, but it does not (Campbell and Green, 1965). As a result, both vision and the quality of retinal images are not as sharp as they could be. There are two main classes of optical aberrations, chromatic and monochromatic aberrations. Chromatic aberration arises because the eye has a different index of refraction for different wavelengths of light, and thus the focal length

of the eye varies with wavelength. This is called axial chromatic aberration. The differing focal length results in a chromatic difference in magnification which in turn produces a shift in the position of objects of different wavelength compositions that is a function of the object's distance from the optical axis of the eye. This chromatic shift in position is termed lateral or transverse chromatic aberration (Bedford and Wysecki, 1957; Zhang et al., 1991b) (see Section 2.6.1.2).

The monochromatic aberrations of the eye arise from a number of sources, including variations in the shape of the tear film, cornea, and lens. The interaction of these sources of aberrations is not simple, and in fact the normal cornea and lens seem to have evolved in a way that either one in isolation generates more aberrations than the combination (Artal and Guirao, 1998; Artal et al., 2001). This compensation appears to have a role in making the optics of the eye more robust to an individual's anatomical variations, for instance in the location of the fovea relative to the optical axis of the eye (Artal et al., 2006; Kelly et al., 2004) since the two have different developmental mechanisms (Hendrickson and Yuodelis, 1984).

Because of the presence of monochromatic aberrations, improving the resolution of retinal measurements required the development of techniques that improved spatial resolution. That is, new technologies were needed to measure spatial frequencies in the retinal images that are not transmitted through the *in vivo* optics due to the eye's aberrations. Early approaches to bypassing this limitation used interference fringes to generate patterns on the retina (Arnulf and Dupuy, 1960; Sekiguchi et al., 1993; Westheimer, 1960; Williams, 1985). These techniques were later enhanced by the use of computational approaches for measuring and overcoming the aberrations of the eye based on analysis of the spatial distribution of light returning from the retina. By measuring the point spread function (PSF) of the eye in single and double pass configurations (Marcos et al., 1996, 1997) or by measuring the speckle pattern in the pupil of the eye (Marcos et al., 1998) it is possible to determine the spatial statistics of the reflecting surface. While these early methods provided non-invasive estimates of cone photoreceptor spacing that agreed well with histology, and retinal densitometry (Marcos et al., 1997), they were difficult to perform, especially in eyes with degraded optics, and therefore the techniques were supplanted by improving imaging methods.

Direct imaging of the retina at cellular resolution started in the latter part of the previous century. The easiest cells to visualize in the human retina are the cone photoreceptors. Normal cones guide light primarily from the pupil of the eye, and return the light back through the pupil (Blokland and Norren, 1986; Burns et al., 1995a; Gorrand and Delori, 1995). While only a fraction of the light shining on a human fundus is returned, the cones provide a relatively large proportion of the light remitted from the retina back through the pupil. This means the cones have a relatively high contrast, which in turn allowed direct imaging of the cones by simply using a flood illuminated fundus camera (Fig. 2), but with a small field to limit the amount of stray light (Miller et al., 1996). Wade (Wade and Fitzke, 1998) used the improved contrast provided by an SLO compared to a fundus camera, together with robust image processing to also image cones in normal eyes. Unfortunately, these direct, non-AO images seem to be restricted to eyes with relatively few aberrations, and to more peripheral portions of the retina where the cones are larger in diameter and less dense, and interspersed with rods that usually guide light more broadly (Van Loo and Enoch, 1975), resulting in a high contrast of the cones. To image cones or other retinal cells at high resolution in a broader population required controlling for the optical properties of the eyes beyond just spherical and astigmatic corrections. That is, methods that correct for imperfect optical conditions by adapting the systems optical properties to any target that is being imaged was needed, and this is the role of AO.

1.4. Adaptive optics

The foundations of adaptive optics retinal imaging were laid at the

University of Heidelberg (Bille et al., 1990; Dreher et al., 1989). Building on earlier work in astronomy (Babcock, 1953; Beckers, 1993; Gonsalves, 1982) and using an SLO (Plesch et al., 1987) developed shortly after Webb's invention of the SLO (Webb et al., 1980, 1987), the Heidelberg group demonstrated that incorporating a deformable mirror into an SLO could improve retinal images (Dreher et al., 1989). A deformable mirror works by changing the surface shape under experimental control. By properly changing the shape, the beam of light entering the eye can be changed such that it compensates for the distortion of the eye's optics. The initial degree of improvement was limited by the limited range of shapes of the mirror, and thus the improvement in image quality was restricted to primarily defocus and astigmatism because the mirror had only 6 segments with 13 electrodes (Dreher et al., 1989). In addition, the mirror shape had to be varied by the experimenter; i.e., it was open loop, since there was not a way to measure the optical performance of the system. A path to better control was addressed the following year when the group incorporated a technique for measuring the wavefront using a Shack Hartmann (SH) wavefront sensor (see below) and coupled this with the SLO and deformable mirror (Bille et al., 1990). Using this improved wavefront information they could correct the image with the mirror shape, iterating to achieve an optimum. However, the system was still limited by the quality of the instrumentation; the mirror was the same as used by Dreher, and the SH sensor generated only 25 measurements across the pupil of the human eye, severely limiting the ability to measure high order aberrations. Nevertheless, these early studies established the promise for the advancements to come. The group next improved the wavefront sensor (Liang et al., 1994) by incorporating 49 measurements across the pupil. The SH wavefront sensor quickly became widely used for measuring optical quality of the eye, supplanting other psychophysical (Howland and Howland, 1977; Ivanoff, 1946; Webb et al., 1992) and optical (Walsh and Charman, 1985; Walsh et al., 1984) techniques.

The first systematic AO assisted measurements demonstrating improvement of both visual performance and *in vivo* imaging of human

cone photoreceptors (Liang et al., 1997) were achieved by using a higher resolution SH wavefront sensor (217 measurements across the pupil) coupled to an improved deformable mirror with 37 actuators). This new system allowed successful correction of higher order aberrations. Since these early studies, active adaptive optics retinal imaging has also moved to AOSLO systems (Roorda et al., 2002) further improving the quantification of retinal structure and function. These advances have arisen from both hardware and software improvements, including wavefront sensing and control, as well as improved imaging system designs and the ability of AO to aid most mechanisms for generating tissue contrast through specialized system or detection designs. In the next section we discussed the underlying platform for AO retinal imaging, as well as some of the advances that are driving the field forward.

2. Adaptive optics retinal imaging systems

2.1. Background

Modern AO retinal imaging systems now typically use a wavefront sensor coupled with a wavefront shaping device, usually a deformable mirror that changes the wavefront of a beam of light under computer control. This combination of a wavefront sensor and wavefront shaping through hardware is sometimes referred to as hardware AO (HAO) to distinguish it from alternative approaches like Sensorless AO (SAO) that can eliminate the need for a wavefront sensor and computational AO (CAO) which eliminates the need for both the wavefront sensor and wavefront shaping. These alternative approaches can be thought of as steps in moving the system complexity from hardware to software. All three approaches are shown in schematic form in Fig. 3. We start with HAO systems since these are the most widely used for human imaging. The SAO and CAO approaches are described below.

At its simplest an HAO retinal imaging system involves two main subsystems (Fig. 3, left). The first subsystem is the imaging system. When appropriately implemented almost any type of optical imaging

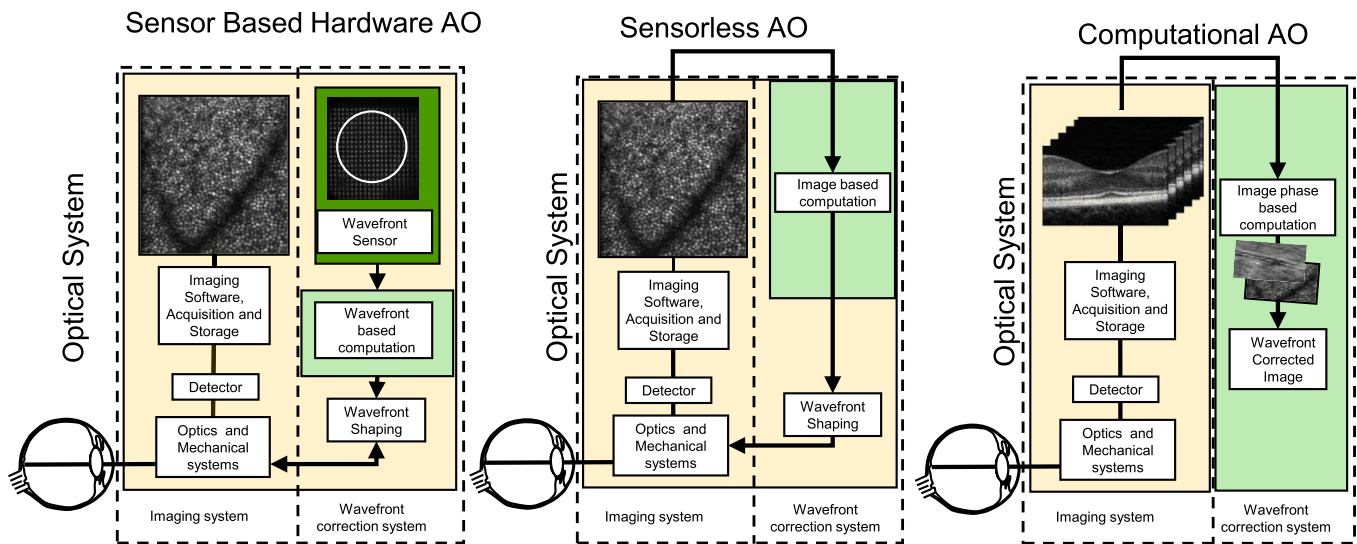


Fig. 3. Schematic diagram of the three main classes of AO systems. Left: hardware based AO (HAO system). For HAO there are two primary components, the imaging system and the wavefront correction system. In the HAO system the control loop includes a wavefront sensor, such as the Shack Hartman sensor, which measures the optical aberrations. These measurement are fed back to the wavefront shaping system, such as by altering the shape of a deformable mirror, which in turn alters the optical properties of the imaging and detecting channels as both the imaging beam and the detecting beam are affected by the wavefront shaping. The wavefront is then measured again, and another correction is made, with measuring and corrections repeating until the noise level of the measuring and correcting system are reached. Center: Sensorless AO (SAO). For SAO the wavefront sensor is eliminated and the properties of the image itself are used to provide an input to the control loop. The system computes an image quality metric for each loop of the control algorithm, and the wavefront shaping device is then altered, the result measured, and the loop iterates until it converges on a diffraction limited image. Right: Computational AO (CAO) goes even further in reducing the hardware by omitting the wavefront shaping device and the need to iterate a control algorithm while imaging. The data are collected using a phase sensitive measurement, and an algorithm then computationally converges on the required wavefront correction. This correction is then implemented as a digital filter applied to the input image.

can be assisted by AO. Thus, while the early systems were either flood illuminated (classic camera) systems (Liang et al., 1997; Rha et al., 2006; Roorda and Williams, 1999) or scanning confocal systems (Bille et al., 1990; Burns et al., 2002; Dreher et al., 1989; Roorda et al., 2002), current systems use almost any imaging approach, including flood illumination (Bedggood and Metha, 2014; Choi et al., 2011; Jacob et al., 2017), raster or line scanning laser ophthalmoscopes (Hammer et al., 2006; Lu et al., 2016a; Mujat et al., 2009; Muller and Elsner, 2018; Muller et al., 2015) and optical coherence tomography (OCT) (Hermann et al., 2004; Zawadzki et al., 2005; Zhang et al., 2005). The second major component is a mechanism for sensing and correcting the wavefront aberrations of the eye. This component is most commonly implemented using a combination of software for control computations and hardware for wavefront sensing and correcting operating in a closed loop (Fernandez et al., 2001). Not shown in Fig. 3, is a third component that is comprised of the suite of tools oriented towards the imaging technician and the clinician/researcher, including the handling of displays, database functions, and processing of the final output of the imaging system.

2.2. Wavefront sensor based AO systems

Systems that measure the optics of the eye using a wavefront sensor, and then correct the wavefront of the eye using a hardware based wavefront corrector, are the most commonly used systems in AO retinal imaging. They have the advantage of robustness and relative simplicity of software and operation, but at the cost of increased hardware complexity. We will first cover the basic components of the sensor based AO systems in some detail, and then briefly present some of the alternatives that are being pursued, finishing with a discussion of the strengths and weaknesses of the different approaches.

2.2.1. Measurements of aberrations

The wavefront error of an imaging system is a fundamental measure of the system's ability to form an accurate image of an object that is limited only by diffraction of light. There are basically two ways to determine the wavefront error. Because most systems cannot make full coherent measurements of light, they instead detect intensity, thus determining the wavefront error becomes a problem in phase retrieval (Fienup, 1982; Gonsalves, 1982, 1983). This can be performed either computationally or by using a wavefront sensor, although the computational approaches typically require more stability than is present in the human eye, and thus incoherent computational wavefront determination (Booth et al., 2002; Jian et al., 2014; Marsh et al., 2003) has not played a major role in retinal imaging.

Techniques for determining the wavefront aberrations of the eye are typically based on the simple observation that in a diffraction limited imaging system different points in the pupil focus to the same location in the image plane. In the presence of optical aberrations, this is not the case, instead each pupil position has a slightly different view of the retina. Similarly light returning from a given point on the retina exits the eye at slightly different angles for different pupil locations. Most wavefront sensors for the human eye depend on this principle (Howland and Howland, 1977; Ivanoff, 1947; Smirnov, 1961). While the early measurements of the eye's wavefront aberrations used psychophysical measurements, the development of the Shack Hartmann wavefront sensor (Liang et al., 1994; Platt and Shack, 2001; Shack and Platt, 1971) greatly simplified the measurement of ocular aberrations.

2.2.1.1. The Shack-Hartmann sensor. The Shack-Hartmann sensor provides a simple and robust way to quantify wavefront aberrations. Basically a SH wavefront sensor is an array of small lenses (lenslets) arranged such that each one focuses collimated light onto an area sensor, typically a CCD or CMOS camera. In the typical implementation the retina of the eye is illuminated by a point source of light. This light produces a small bright spot on the retina which in turn acts as a light source, the beacon, for the SH sensor. If the eye had no aberrations and was in perfect focus, then light exiting the pupil would consist of a bundle of parallel rays exiting the eye, as shown for an ideal lens (Fig. 4A). This light is then re-imaged back onto the SH sensor, which is typically optically conjugate to the eye's pupil. Each lenslet in the array would then focus light into a spot on the optical axis of the lenslet creating a series of spots on the CCD (Fig. 4B). However, if there are aberrations, the rays originating from the beacon are not parallel as they exit the eye (Fig. 4C). When the pupil is then re-imaged onto the wavefront sensor, each lenslet forms an image on the sensor surface. The location of the bright spot on the sensor for each lenslet depends on the local slope of the wavefront across the lenslet, and for this reason the SH sensor is a slope sensor, being sensitive to the spatial derivative of the wavefront. Typically an algorithm (Prieto et al., 2000) will then compute the centroid of each of these spots, which can usually be computed to roughly one tenth of the pixel dimensions. Thus these deviations are computed rapidly and continuously via the control software. There are two general classes of control algorithm. The first class uses a series of smooth functions to approximate the wavefront. These are often Zernike polynomials and then the coefficients of the polynomials are input to the control algorithm. This first class of controls is referred to as modal controls. The second class are local controls, and these use the local slopes of the wavefront to directly control the wavefront shaping device. Both classes of control can vary

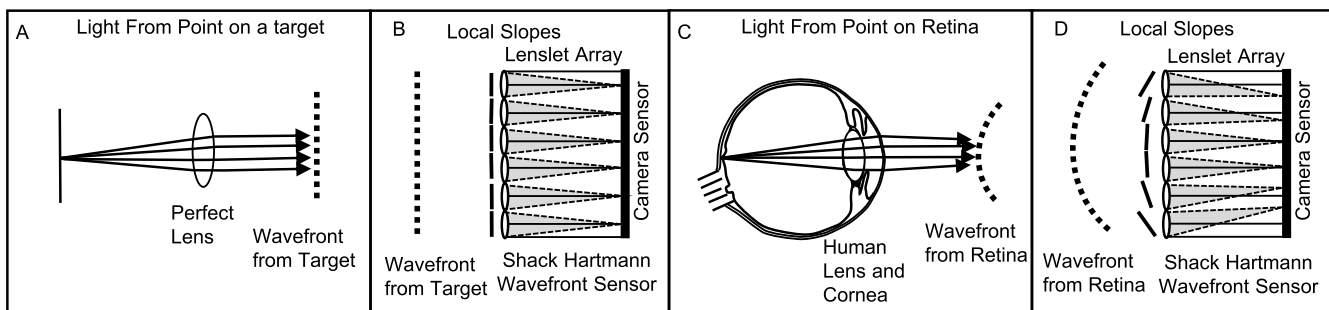


Fig. 4. Operation of the Shack-Hartmann (SH) sensor. A: for a light source located at the focus of a perfect, diffraction limited lens, light will emerge from the lens perfectly collimated (all rays parallel). B: These parallel rays then come to an array of small lenses (lenslets) with an imaging sensor located one focal length behind the lenslets. Because the wavefront at each lenslet is flat, and orthogonal to the optical axis of the lens, each lenslet will produce a diffraction limited spot along its own optical axis on the image sensor. C: For a real eye, if a spot is imaged on the retina, light from that spot does not emerge from the eye perfectly collimated, but instead the rays vary with pupil location. This produces a non-flat wavefront. D: When this wavefront is reimaged at the SH sensor, each lenslet then has a wavefront impinging on it from slightly different angles. Since a lens produces an image offset from the optical axis at an angle proportional to the input angle, this means that a series of spots will be formed on the sensor, where the displacement of the spot relative to the optical axis of the lens will be proportional to the slope of the wavefront seen by each lenslet.

the focus of the system to image a particular layer of the retina.

2.2.1.2. Other wavefront sensors. While the SH sensor is the most widely used in retinal imaging due to its simplicity and efficiency, the limited spatial resolution could be a problem in the presence of high spatial frequency aberrations. Thus, other sensors have been investigated for the eye. For instance the pyramid sensor (Chamot et al., 2006; Iglesias et al., 2002; Lombardo and Lombardo, 2009; Ragazzoni, 1996) computes optical phase over the whole pupil, as do interferometric methods, such as a shearing interferometers (Lombardo and Lombardo, 2009). However, these alternative wavefront sensing methods have not been widely adopted primarily due to added complexity, plus they often require that relatively more light be dedicated to the wavefront sensing. In general most of the light returning from the retina is sent to the imaging detectors, rather than using a larger proportion for small improvements in the precision of wavefront correction.

2.2.2. Hardware correctors for aberrations

The purpose of a hardware aberration corrector is to vary the time delay (optical path length) of light over space. This can be done in reflection or transmission mode, the only requirement being that the corrector can vary the delay over space. The corrector is often placed conjugate to the pupil of the eye, but this is not a requirement. While the requirements of a wavefront corrector to provide diffraction limited performance have been systematically investigated (Dalimier and Dainty, 2005; Doble et al., 2007; Miller et al., 2005) few actual wavefront correctors meet all of the desired specifications and trade-offs must be made according to the application. Wavefront correctors are characterized primarily by their spatial resolution, as well as by the amplitude of the aberrations that they can correct (the stroke). However other factors are important, including speed, reflectivity (or transmissivity), surface quality, polarization properties, linearity of the control of the wavefront, and independence of control from location to location across the corrector. In this section we discuss some of the types of wavefront correctors and their limitations.

2.2.2.1. Liquid crystal phase plates. Liquid crystals (LCs) are composed of oriented molecules which have a different index of refraction in one direction compared to another. Typically the orientation of these molecules can be altered by an electric field applied as a function of position, and thus the time delay for light passing through them can be varied over space. If a liquid crystal display (LCD) display is set up to change only the phase and not the amplitude, then they can be used as an LC phase modulator, varying the delay of light over space. This allows them to be used as wavefront correctors (Muramatsu et al., 1997; Shirai et al., 2000, 2009; Thibos and Bradley, 1997). While the total delay that can be programmed into an LC array is small, the high spatial resolution of modern LC phase modulators, allows them to be used with phase-unwrapping, similar to Fresnel lenses. The strength of the LC phase plates is that they can correct wave aberration with high spatial frequency, are easily programmed, and are relatively inexpensive. However they have a number of important limitations which have restricted their use in general purpose retinal imaging systems. First, they are highly wavelength dependent. This occurs because phase unwrapping requires that an appropriate number of waves of delay be introduced at each phase wrapping location, and this varies with the wavelength being used. Second, they need to be used with polarized light. Both the cornea (Cope et al., 1978; Van Blokland and Verhelst, 1987) and the retina exhibit birefringence (Blokland, 1986b; Blokland and Norren, 1986), and thus the polarization of light returning from the eye can be rotated relative to the input light and exhibits individual differences (Elsner et al., 2007). This can decrease the light efficiency of the imaging system for some retinal structures as well as limits the flexibility of the imaging system. Nevertheless, for well specified problems liquid crystal phase plates can be a cost-effective, flexible means for controlling wavefront aberrations.

2.2.2.2. Deformable mirrors. The most widely used types of wavefront correcting devices are deformable mirrors. These include piezo-electric deformation of glass (Chamot et al., 2006; Liang et al., 1997), microelectromechanical (MEMS) mirrors (Burns et al., 2007; Doble and Williams, 2004; Doble et al., 2002; Zhang et al., 2006), electrostatic (Vdovin and Sarro, 1995), and electromagnetic (Fernandez et al., 2006b; Zou et al., 2008) mirrors. The piezoelectric mirrors work by using piezoelectric stacks to deform a glass surface. These have largely been replaced for ophthalmic imaging due to their high cost. Further, they generate only a relatively small deformation in their surface shape (called the stroke of the deformable mirror), limiting their use in a wide range of eyes. The MEMS mirrors have a high actuator count, but limited amounts of stroke that can be imposed. MEMS mirrors are less expensive than some alternatives, and while diffraction from the electrodes had been a previous problem, modern MEMS deformable mirrors have much better surface quality than early generations. Electromagnetic deformable mirrors have excellent surface properties and large strokes, thus most recently developed AO systems for human imaging use electromagnetic mirrors (Dubra et al., 2011; Gomez-Vieyra et al.; Gray et al., 2006). However high stroke, high actuator count mirrors are currently expensive. One alternative combines a lower actuator count, high stroke mirror with a high actuator low stroke MEMS mirror (termed a woofer tweeter arrangement) (Chen et al., 2007; Li et al., 2010a; Zou et al., 2008). A second alternative is to simply pass the imaging and return beam twice across a MEMS deformable mirror (termed a wavefront doubler) (Webb et al., 2004). Both of these alternative approaches can be cost effective since the MEMS mirrors have a strong cost advantage. The performance of both a woofer tweeter design (Ferguson et al., 2010; Zou et al., 2008) and a doubler design (Lammer et al., 2016) have been proven in long term clinical applications. The advantage is that this approach is among the cheapest for clinical systems, since the MEMS mirrors are much less expensive than electromagnetic mirrors but this design comes at the cost of an additional set of pupil relay optics.

2.2.2.3. Programmable lenses. Another approach to reduce the demand of the wavefront corrector is to couple a lower stroke high spatial frequency wavefront corrector with either a badal optometer, which requires moving parts, or a programmable lens. The badal optometer can be used to bring the eye to the best focus, decreasing the demand on the wavefront corrector so its limited stroke is not used correcting refractive errors. This approach can provide excellent imaging performance (Burns et al., 2007). Since defocus is typically the largest optical aberration in the population, this can greatly increase usefulness of a system at relatively low cost. The disadvantage is that it adds another mechanical system to an already complex imaging system. An alternative to the badal optometer is a programmable lens (Jian et al., 2016) which can change shape in response to an applied voltage. By placing such a lens at a pupil conjugate plane the ametropia of a subject can be corrected without changing the magnification, leaving the deformable mirror to correct higher order aberrations.

2.3. Sensorless AO (SAO)

SAO does away with the need for a wavefront sensor by using the image itself to provide an estimate of wavefront quality. This is practical because in an AO system the quality of the image is related to the aberrations. Thus, if the wavefront shaping system is stochastically varied and image quality monitored, the image can be improved (Hofer et al., 2011; Vorontsov and Sivokon, 1998; Wong et al., 2015; Zommer et al., 2006). The choice of image quality metric is fundamental for this approach. The simplest metric for a confocal imaging system or a two photon system is simply image brightness, since the compactness of the point spread function of the system determines how much light passes through the confocal stop, or generates two photon fluorescence and thus brightness is directly related to image quality. This metric can

produce images of the photoreceptors and other bright structures (Hofer et al., 2011). This simple metric runs into problems if one is not trying to focus on the brightest layers of the retina. To avoid this problem more complex image quality metrics can be used (Debarre et al., 2007; Jian et al., 2016; Polans et al., 2017; Zhou et al., 2015). A second concern for SAO in the human eye is the speed of convergence. Typically many iterations of the control loop are required because the search space is relatively large, encompassing aberrations of at least four orders. The search time can be decreased by using a modal approach and weighting the most important aberrations (such as defocus and astigmatism) more highly. However, aberrations change quickly (Diaz-Santana et al., 2003; Hofer et al., 2001; Yu et al., 2015) especially in individuals with dry eye, and this has limited the practicality of SAO imaging. However, SAO is still under rapid development (Ju et al., 2017; Polans et al., 2017; Wen et al., 2018; Wong et al., 2015; Zhou et al., 2015) and has wide applications in animal imaging and microscopy where the increased convergence time is not as critical. SAO does have advantages. First, and perhaps most obviously is that it is less complex optically, and all of the light budget is devoted to imaging. Second, it requires less calibration, and it will converge on the best image quality and is not susceptible to differences between the imaging optics and the wavefront sensing optics (Sulai and Dubra, 2014). Third, it is robust to slight changes that may alter the spatial relation between wavefront sensor and imaging beam.

2.4. Computational AO (CAO)

CAO (Liu et al., 2017b) simplifies the hardware even more. Early computational techniques used approaches such as deconvolution (Catlin and Dainty, 2002; Christou et al., 2004; Iglesias and Artal, 2000) that are intensity based, and they often combined the images with information from a wavefront sensor to improve the computations. However, as HAO systems improved to regularly reach diffraction limited performance the need for deconvolution techniques decreased. Currently, most CAO imaging uses techniques that capture both the amplitude and phase of light returning from the retina, such as OCT, combined with computational approaches, to reach the diffraction limit. The important feature for CAO is that the imaging system must be able to measure the impact of aberration deviated light on the image. That is, in HAO the deformable mirror control adjusts the light entering the eye to an angle for each pupil entry position which, after being deviated by the aberrations of the eye, cause the rays to strike the same retinal location. In computational AO this is not done. On illumination of the retina, light from different locations in the pupil will strike different location on the retina. When light is scattered back through the pupil from these multiple location it will exit the pupil at different angles, and the total phase delay for a given ray depends on the total transit time. Thus, from the measured phase and amplitude the impact of aberrations can be minimized (Jian et al., 2016). No AO hardware is required and no hardware control loop is required (Fig. 3). The computations typically require iteration and use either global image sharpness optimization (Adie et al., 2012; Hillmann et al., 2016) similar to that used for SAO, or an approach that uses a digital subdivision of the light where the signal for different positions in the pupil conjugate are calculated and the displacement between these locations at the retina are used, similar to how an SH sensor works (Kumar et al., 2013, 2015). Because the phase and amplitude are known, these iterative approaches can apply digital filters to improve the images in post-processing. In fact, by varying an applied phase, for instance a spherical wave, computational AO can be refocused to different retinal layers, a limitation for HAO. The advantages are obviously the lower hardware burden, the potential for increased field sizes and depth discrimination, and the fact that rapid advancements in computational power will continue to improve the utility of these techniques. The disadvantages arise from two main factors. First, the system being imaged must be phase stable (Shemonski et al., 2014) within the imaging time required,

because the image itself is being used to make the computations, changes in aberrations occurring within that time frame will degrade the ability to correct the image. For out of focus objects, where the beam is large, a scanned systems will need to use multiple scans to sample all the light, and thus high speeds are important (Shemonski et al., 2014). Additionally, the phase stability requirements also apply to the hardware. Traditionally HAO systems have made major efforts to stabilize phase with relatively complex optical designs. OCT systems have been less demanding. However there are ongoing efforts to also use computational methods to correct phase instabilities (Liu et al., 2017b), although if the data are insufficiently sampled this may require more data. Second, the signal to noise must be excellent. Overall, computational AO is very promising, but it does require that the imaging hardware is fast, and signals are strong, and it is not clear how well this can be translated to more difficult patient imaging situations. In summary, this is a rapidly developing field, but it is important to note that at the current time the need for high speed imaging negates the cost advantage of eliminating the deformable mirror.

2.5. Requirements for accurate AO correction in a population

There are a number of challenges that affect imaging a broad cross-section of the human population. A factor that has slowed the development of AO retinal imaging is the need to first understand these challenges across patients, and then to generate robust approaches to deal with them.

The first issue is the speed at which aberrations vary in the eye. Early systems had either no ability to deal with temporal variations (Burns et al., 2002) or were relatively slow, which included sequential time periods for sensing and correcting aberrations and then imaging. Variations in aberrations arise from accommodative changes, pulsatile changes in both the anterior and posterior segment, and changes in cornea and the tear film (Collins et al., 1995; Diaz-Santana et al., 2003; Gruppeta et al., 2005; Hampson and Mallen, 2012; Nirmaier et al., 2003). Temporal variations in aberrations have their highest amplitude at relatively low temporal frequencies and decrease in amplitude at about 4 dB per octave (Hofer et al., 2001). Nevertheless, wavefront fluctuations extend to quite high frequencies and an improvement in AO image quality has been observed for AO systems running their correction loop at 100 Hz (Yu et al., 2015). In people with dry eye there are rapid localized changes in the tear meniscus, and this can cause a control loop tuned for normal eyes to be less stable between blinks. Finally, the issue of pupil size and shape becomes important. Older subjects have smaller pupils (Winn et al., 1994); and the shape of the clear aperture can be irregular due to both opacification of the lens, cataract, and the shape of the opening in the posterior capsule after capsulotomy post cataract surgery. Dealing with pupil size and shape can be handled by either restricting the pupil to a size that fits within the open aperture for each eye, or by using more complex automated procedures for AO control (de Castro et al., 2017). These problems are equally critical for SAO and CAO. SAO requires stability within the time period for image improvement, and CAO requires phase stability over the entire time a given region of the retina is being illuminated.

2.6. Types of imaging systems

AO is really a technology platform for minimizing the impact of optical aberrations of the eye on any measurement. This means it can be combined with almost any imaging or psychophysical studies. A discussion of broader issues for AO vision and retinal imaging systems has recently been published (Marcos et al., 2017), Section 2 concentrates on an overview of AO retinal imaging methods.

2.6.1. AO flood illuminated imaging

The most straightforward approach to AO assisted retinal imaging is to couple a high magnification fundus camera (Fig. 2) with a wavefront

sensor and a deformable mirror. Thus, flood illuminated AO systems provided some of the first systematic studies of retinal properties, particularly the cone photoreceptors (Liang et al., 1997). This approach is the basis of a commercial AO retinal imaging system, the RTX-1 (Imagine Eyes, Orsay France). Flood illuminated systems have been used for extensive analysis of both cone photoreceptors (Le Gargasson et al., 2001; Liang et al., 1997; Roorda and Williams, 1999) (Hofer et al., 2005; Legras et al., 2018; Lombardo et al., 2013c; Soliman et al., 2016; Supriya et al., 2015; Xue et al., 2007) and vasculature (Bedggood and Metha, 2014; Koch et al., 2014; Lerme et al., 2014).

An important advantage of AO imaging with a flood illuminated system is that the entire retinal image is typically acquired in times on the order of a few msec. Thus, a single image is minimally affected by eye movement, providing a non-distorted view of the retina. Scanning techniques such as AOSLO and AOCT systems build images up over time by scanning the illumination spot, and thus there can be shear within an image. An additional advantage of flood illuminated systems is that they can provide very high frame rates with high sensitivity, especially for a small field (Bedggood and Metha, 2012a; b; Bedggood and Metha, 2013). However, many research instruments have transitioned away from flood illumination, because they typically have lower contrast due to the inclusion of multiply scattered light from most of the retina and choroid, especially at longer wavelengths (Elsner et al., 1996).

2.6.2. AOSLO imaging

2.6.2.1. Variation of detection apertures and modes of imaging.

Coupling a scanning laser ophthalmoscope with AO (AOSLO) increases contrast relative to flood illumination, and allows flexibility in controlling the portion of light returning from the retina that makes up the retinal image. Thus modern AOSLO designs allow detection of both singly scattered and multiply scattered light (Chui et al., 2012b, 2013; Elsner et al., 1998b, 2000; Scoles et al., 2013; Sulai et al., 2014). In addition the AOSLO can be used with other contrast mechanisms, including single photon (Morgan et al., 2009; Rossi et al., 2013) and multiphoton (Hunter et al., 2011; Sharma et al., 2016) fluorescence and even fluorescence lifetime imaging (Feeks and Hunter, 2017). These technologies allow the AOSLO to provide information on specific molecular events and because of this are in rapid development. While the use of single photon fluorescence is being used in humans for studying the retinal pigmented epithelium (RPE) (Morgan et al., 2009; Rossi et al., 2013; Tam et al., 2016) (see below), multi-photon and fluorescence lifetime based techniques are not deployed in humans, but

may be important in the future (Dysli et al., 2017; Schwarz et al., 2016).

When an AOSLO is used for confocal imaging (sometimes referred to as a cAOSLO) an aperture is placed conjugate to the retina (Fig. 2). The system optics image the illumination source onto the retina as a very small spot, collect the light remitted from the retina back through the pupil, and then image the retina onto an aperture. The aperture limits the light reaching the detector to light that originates from near the center of the focused point spread function (PSF). As a result confocal imaging systems primarily detect light backscattered from the center of the PSF in the plane of focus and minimize contributions from out of focus scattering objects as well as light that is forward scattered from the focal plane or multiply scattered within the eye. This has two advantages. First, it increases contrast for objects at the plane of focus, and second, it is sensitive to changes in the refractive index, and less sensitive to absorption contrast (Elsner et al., 1992b). An SLO typically requires a mechanism to change the location of the imaging beam on the retina over time, that is, to scan the beam. The scanning optics and the associated data acquisition builds up an image sequentially from a series of points (Webb, 1984, 1996) lines (Benedetti et al., 1992; Hammer et al., 2003; Koester, 1980) (Benedetti et al., 1992) or other patterns (Muller et al., 2015; Webb and Rogomentich, 1995). The SLO also has the benefit of being able to use intrinsic fluorescence as a contrast mechanism allowing measurements of RPE cells (Morgan et al., 2009; Rossi et al., 2013) and by using extrinsic fluorophores allowing visualization of RPE cells (Tam et al., 2016) and retinal vasculature (Chui et al., 2014b; Dubow et al., 2014; Pinhas et al., 2013). For retinal vessel measurements however the use of dye has been primarily replaced by the use of multiply scattered light to generate contrast.

Multiply scattered light (Elsner et al., 2000, 2001) AOSLO images are a type of dark field imaging (Fig. 5). In typical *trans*-illumination microscopy the image is formed by light that is transmitted through the sample and forms the image. Light that is more broadly diffracted or refracted by the tissue is blocked by an imaging stop (Fig. 5A). In this case the overall field is bright since most of the light is undeviated, and features are seen as variable decrements in the brightness on an otherwise bright background. The contrast arises from absorption or scattering of light out of the imaging stop. In dark field microscopy (Fig. 5B) an optical stop blocks the directly transmitted light and passes light that has been more widely deviated. In this case the image is dominated by structures that deviate the light, seen against a dark background. This deviation of the light arises primarily from diffraction and refraction, and thus a dark field image tends to emphasize local changes in the index of refraction of tissues. The SLO is similar, except it

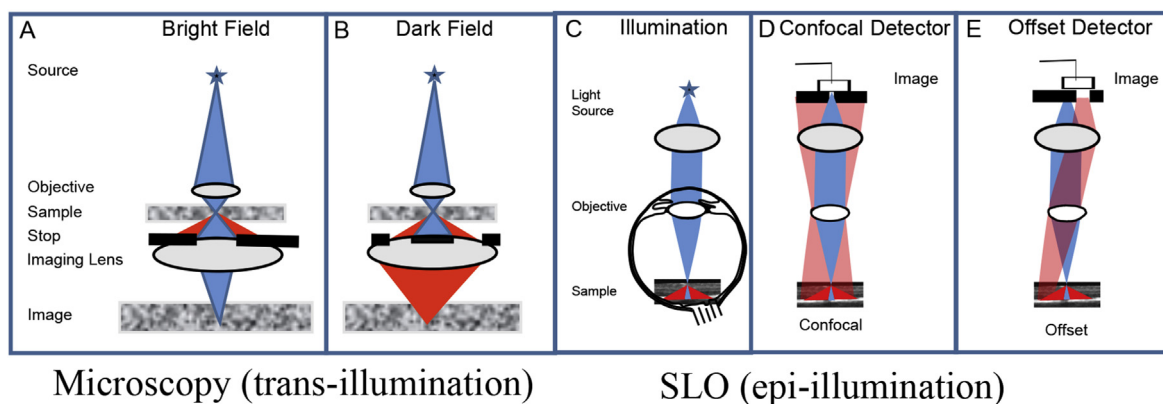


Fig. 5. Comparison of bright field and dark field imaging in microscopy and in retinal imaging. A: dark field transmission microscopy passes light through the target and objects are typically seen as decrements on a bright background. B: In dark field microscopy an annular stop blocks undeviated light but passes more deviated light, showing objects as bright on a dark background. C: An SLO works in epi-illumination, which means the illumination and sensing are both from the same side, in this case the human pupil. Here some light is forward scattered at high angles from the focal spot (red triangle) D: Confocal imaging with an SLO puts an aperture conjugate to the focused spot of the illumination, and thus only light that is coming from the focal volume is detected. E: In multiply scattered light imaging, the directly backscattered light is blocked by a stop and the aperture, here a displaced aperture, lets through light that has been forward scattered and then scattered a second time and returned through the aperture, similar to the dark field microscopy and thus multiply scattered light imaging can reveal translucent structures.

works in epi-illumination mode; that is, the image is built up from light that comes back in the same direction as the illumination. Confocal images are built up by illuminating the retina with a scanning beam (Fig. 5C). After interacting with the retina some of this light is directly backscattered towards the pupil, and some is forward scattered by diffraction or otherwise deviated into a broader cone (red triangle). This light then strikes other reflective retinal structures. For the retina this is any retinal structure that backscatters light into the pupil (Delori and Pflibsen, 1989). When a confocal aperture is used (Fig. 5D), light that is backscattered from the plane of focus, through the pupil and focused through the confocal aperture (Fig. 2) reaches the detector and contributes to the image. Light that is forward scattered is mostly eliminated from the image by the confocal aperture. With an offset aperture or other non-confocal aperture configuration (Fig. 5E), light directly backscattered is blocked by the aperture, but light that has been forward scattered and exits the pupil at the appropriate range of angles passes through the offset aperture and is detected. Confocal images provide high contrast and sensitivity to backscattered light, and displacing the aperture or using other aperture configurations that sample the skirts of the PSF provides images of translucent structures, just as in dark field transillumination imaging. This distinction is important, because the two types of images use different parts of the light emerging from the pupil, and thus they can be collected simultaneously (Sapoznik et al., 2018). Because of the range of aperture configurations available, and the strong dependence of scattering angle on cell size and morphology, simply changing the shape and location of the aperture can provide different information about the retina (Fig. 5). Here we see a small arteriole from a diabetic patient. All images were collected from the same 3 s acquisition. The system uses two illumination channels, with one of the channels using three detectors. Channel 1 uses a confocal aperture (Fig. 6A), and two non-confocal apertures, one from a half-annulus, with the inner and outer radii set to collect light that is

horizontally scattered (Fig. 6D) and the other collecting the rest of the multiply scattered light (Fig. 6E). Channel 2 uses an offset aperture at a slightly different wavelength (Fig. 6B). The information from each detection aperture varies. Examples include combining information over space, as in Fig. 6F which shows the computed contrast between images C and D, or over time, which emphasizes the motion of the blood cells by computing the time variation within the 3 s acquisition for the offset aperture image. The time-varying image is called variously a standard error image, variance image, vascular or perfusion map and arises from the motion of the blood cells.

A number of techniques for collecting multiply scattered light are currently used. Offset aperture imaging tends to provide enhancement of structures that are scattering light in one direction and is easy to implement using a single additional detection channel and a pinhole that can be placed in a fixed position relative to the center of the PSF. Split detection (Sulai et al., 2014) uses a sharp edge or knife edge to deviate light falling outside the center of the PSF into two additional detectors (one for each direction). From these detectors the local contrast for scatter orthogonal to the edge can be computed. Using a spatially variable mask (Sapoznik et al., 2018) allows almost any aperture shape to be used, increasing flexibility and light efficiency but also complexity. The programmable aperture can quantify the angular scattering properties of tissues, although the exact geometric relation between the location of the focus in the tissue and the second (or multiple) scattering structures is not well controlled. In the normal retina, it is the moving blood cells that scatter light over the largest angles (Sapoznik et al., 2018). In the AOSLO multiply scattered light imaging provides excellent contrast for blood vessels (Chui et al., 2012b), mural cells (Chui et al., 2013), inner segments of cones (Cunefare et al., 2016; Langlo et al., 2016), and ganglion cells (Rossi et al., 2017; Sapoznik et al., 2018). The resolution of this type of imaging arises from the movement of the focused imaging beam across

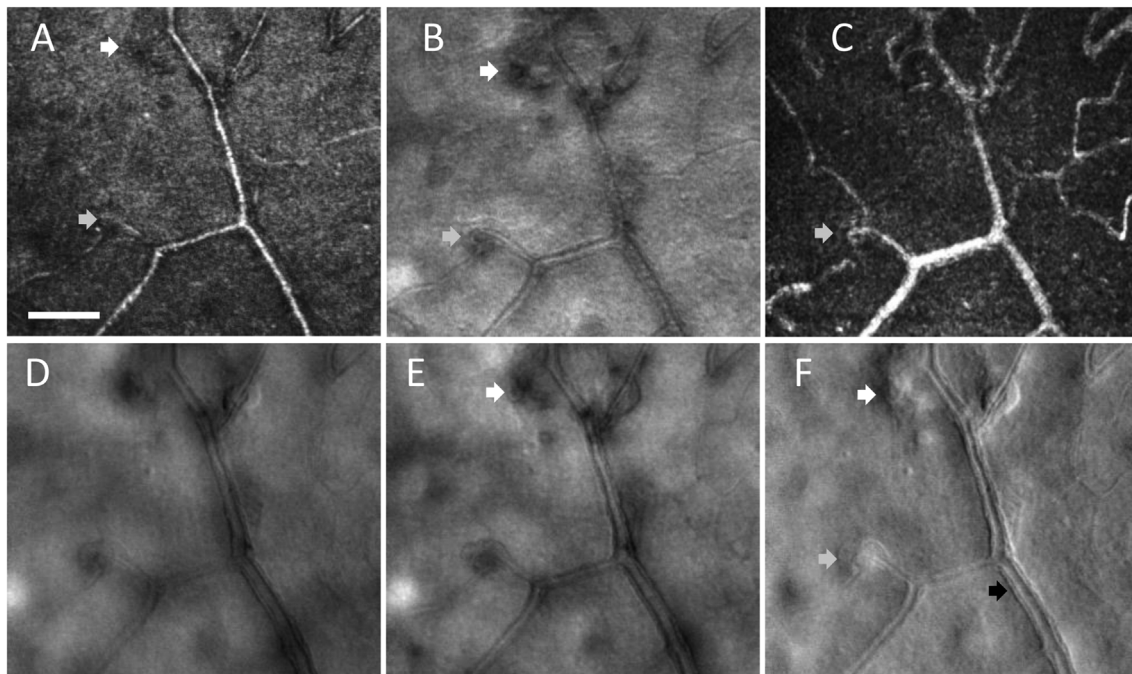


Fig. 6. Retinal capillary remodeling and edema in a diabetic subject showing capabilities of different imaging modes used simultaneously. A: Retinal capillaries imaged using a confocal aperture with a 2x Airy disc (AD) pinhole. B: The same capillaries imaged using an offset aperture with a 10x AD aperture displaced 6 AD diameters. C: A perfusion map of the same capillaries. The perfusion map is computed from variations in intensity that arise from blood flowing through the capillaries. D: Half annulus image. E: Complement of the half annulus image (Sapoznik et al., 2018). F: The same capillaries in a contrast image computed as $(D-E)/(D+E)$. The contrast of various features changes with the mode of imaging. A capillary loop and surrounding area of edema (gray arrows) are least visible in the confocal image and most visible in the vascular map (C) or offset aperture image (B). A larger area of edema (white arrow) is readily detected in most of the images, but shows different characteristics, across imaging modes. Vascular walls are visible in capillaries, and best seen in the contrast image (F: black arrow). Scale bar 100 μm .

retinal features. High spatial frequency information is generated only at the focus of the beam. Thus, multiply scattered light imaging does not have the confocal advantage for lateral resolution (Webb, 1996; Wilson and Carlini, 1987), but can achieve diffraction limited non-confocal resolution.

2.6.2.2. AOSLO imaging: the role of wavelength and polarization. Most AOSLO systems use reflective optics (Burns et al., 2007; Ferguson et al., 2010; Gomez-Vieyra et al., 2009; Morgan et al., 2008; Roorda et al., 2002; Zhang et al., 2006, 2015a), although refractive elements can be used (Burns et al., 2007; Felberer et al., 2014). The major advantage of reflective designs is their wavelength versatility, allowing simultaneous use of multiple wavelengths (Grieve et al., 2006). However, for confocal imaging retinal contrast is primarily generated from the change in the index of refraction at interfaces, with absorption playing a minimal role. Thus, for confocal imaging, there are not strong differences in retinal appearance with wavelength, although resolution is inversely related to wavelength. However, other imaging modes are wavelength dependent. Thus AOSLO systems can be readily adapted for fluorescence imaging of both endogenous (Morgan et al., 2009; Song et al., 2014) and exogenous (Dubow et al., 2014) fluorophores, and for identifying bleachable photopigment using retinal densitometry (Hofer et al., 2005; Roorda et al., 2001; Tuten et al., 2017). However to date there has not been much work using multiply scattered light, which tends to be more sensitive to absorption by retinal pigments (Elsner et al., 1992a; Remky et al., 1996). One disadvantage of using multiple wavelengths simultaneously is the impact of the eye's chromatic aberration (Bedford and Wyszecki, 1957). Chromatic aberrations arise from the difference in the index of refraction of the eye with wavelength (dispersion). While each ocular component has a slightly different variation in dispersion with wavelength (Sivak and Mandelman, 1982) the eye's overall chromatic aberration is dominated by the dispersion of water and changes rapidly with wavelength at the short wavelength end of the spectrum and more slowly at longer wavelengths (Atchison and Smith, 2005; Howarth and Bradley, 1986; Sivak and Mandelman, 1982). The difference in focus with wavelength of the eye is relatively fixed between individuals (Howarth and Bradley, 1986) and thus can be compensated by varying the focus of individual light sources in the illumination system or by using an achromatizing lens (Fernandez et al., 2006a; Lewis et al., 1982; Powell, 1981). However the difference in focal length also causes

a change in magnification with changes in wavelength, and this is expressed in the eye as transverse chromatic aberration (Sincich et al., 2016; Zhang et al., 1991a). Because the relative alignment of the different optical elements of the eye differs across individuals, transverse chromatic aberration varies between individuals (Marcos et al., 2001).

The interaction of retinal tissues with light is also polarization dependent. This polarization dependence can be used to enhance or minimize contributions to an image from different retinal tissues. In general, light returning from the cones is highly polarization preserving (Blokland, 1986a; Burns et al., 1995b) whereas light that has been multiply scattered is depolarized (Burns et al., 2003; Mellem-Kairala et al., 2005). In addition, the nerve fiber layer and Henle fibers of the retina exhibit form birefringence (Brink, 1991; Knighton et al., 1998; Sommer et al., 1984) allowing polarization sensitive techniques to provide improved quantification (Bueno, 2000; Dreher and Reiter, 1992; Sommer et al., 1984). That is, imaging polarimetry can be used to selectively emphasize different features of the retina (Bueno, 2000; Burns et al., 2003; Dreher et al., 1992; Twietmeyer et al., 2008). This has been used with SLO (Miura et al., 2017; VanNasdale et al., 2011, 2012) and OCT (Cense et al., 2018; de Boer and Milner, 2002; Pircher et al., 2004) imaging. This has been applied less in AO imaging, although it is clear that polarimetry can be used to increase cone contrast by suppressing scattered light (Song et al., 2008, 2010) and with AO-OCT (Cense et al., 2009, 2018; Kurokawa et al., 2010) to better understand tissue properties and detect RPE scattering (Baumann et al., 2009).

2.6.3. AO-OCT imaging

AO-OCT for the human retina was first demonstrated more than ten years ago (Drexler et al., 2004; Hermann et al., 2004; Zhang et al., 2005) and is now starting to play a major role in scientific investigations of the retina. The large dynamic range of OCT, as well as the ability to restrict processing to specific depth resolved structures allows improved visualization of cells at numerous levels. The principles of OCT and the advantages of AO-OCT have been fully reviewed in recent years (Jonnal et al., 2016; Kashani et al., 2017; Pircher and Zawadzki, 2017). There are two major strengths for AO-OCT. First, it combines the advantage of increased lateral resolution afforded by AO assisted imaging, with the ability of using partial coherence interferometry to provide depth information (Fercher et al., 1988), the second advantage

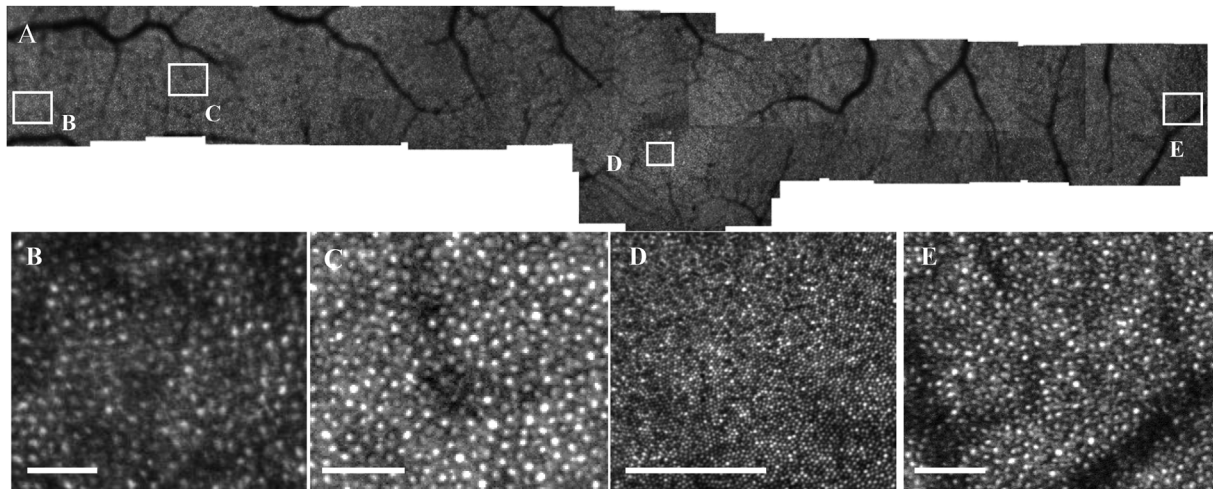


Fig. 7. Rapid Acquisition of sequential AOSLO images using beam steering to build a montage that maps the cones from $+10$ to -10° in a 34 year old male. Images were collected as averages of 100 frames per grab. After each video sequence the system displaced the beam by 1° , and acquired the next, generating a 22×3 degree montage in about 12 min. After this a more densely sampled foveal array was collected at a digital resolution of 0.67 mm/pixel , again using an automated sequence taking about 3 min. A: Image quality is good into the temporal retina out to 10° (box and panel E), and in the foveal center (box and panel D), as well as at 10° in the nasal retina (C). Image quality decreases somewhat at the edge of the steering field (box and panel B) requiring moving the fixation target. Scale bars $50 \mu\text{m}$.

is that it provides both optical amplitude and phase measurements. Thus, when imaging in the living eye, if there is a sufficiently strong change in index of refraction from two or more nearby surfaces, the distance between them can be measured to 10s of nanometers, which has allowed measurements of biological processes such as the daily growth and phagocytosis of the cone outer segments (Jonnal et al., 2012; Kocaoglu et al., 2016). As a coherent imaging technique AO-OCT is sensitive to scattered light from nearby structures that can interfere, generating complex interference patterns, known as speckle noise or simple speckle. Because speckle has a wide range of spatial frequencies, care is needed to avoid spurious identification of retinal features. Speckle is typically minimized by using frame averaging, that is averaging across b-scans, because even small motion changes the speckle structure (Fercher and Briers, 1981). Thus the combination of motion in the whole eye, with fluctuations in the illumination, as well as in cells and organelles allows improved visualization of multiple retinal structures, including ganglion cells (Liu et al., 2017c), RPE cells (Liu et al., 2016) and the choriocapillaris (Chu et al., 2017). Currently AO-OCT data acquisition rates are lower than AOSLO acquisition rates, making the stabilization (Kocaoglu et al., 2014; Zawadzki et al., 2014) or post acquisition correction of eye motion even more important than it is for AOSLO imaging. However an advantage for the AO-OCT alignment is that it can stabilize images in all three dimensions (axial as well as lateral) and has excellent axial resolution to pinpoint individual cells. A main disadvantage is related to the main advantage: the coherence detection limits the wavelength range and limits the use of multiply scattered light.

2.7. Future of AO systems

To date the HAO systems are the most widespread systems in use for human clinical AO retinal imaging. HAO systems work with eyes that have changes in aberrations occurring over relatively short time periods (for instance due to tear film instability) and can still require images with some degree of cataract, intraocular lenses and irregularly shaped posterior capsulotomies, all of which can increase scatter considerably. They also tend to be robust, with systems able to go long periods (years) without recalibration. In addition research systems regularly use multiple imaging modes simultaneously (Fig. 6). HAO systems also continue to improve in speed of both the wavefront control loop and the imaging. The speed of convergence and the incorporation of features such as wide field steering and direct automated steering (Huang et al., 2012) for montaging allow the rapid acquisition of large regions of

retina (Fig. 7), and the incorporation of real time image based tracking (Zhang et al., 2015a) for rapid montaging overcomes some of the limitations of the small retinal region that a single deformable mirror system can correct at any instant in time. There have been a number of attempts to expand the spatial extent over which AO can improve an image, primarily by the application of multi-conjugate AO. The multiple refracting surfaces of the eye restrict the range of angles that can be corrected with a single mirror because that single mirror can approximate the aberrations only for rays that pass through the same aberrating surfaces. The angle over which the aberrations are essentially identical is known as the isoplanatic angle, and for humans is on the order of 2° (Bedggood et al., 2006, 2008). For larger angles a second wavefront corrector can be used. By placing this optically conjugate to a different plane within the eye, the two mirrors can increase the angle of diffraction limited performance. This has been used in the eye (Popovic et al., 2011; Thaug et al., 2009) but the major limitation is the cost and complexity of the systems.

For SAO the primary advantage is the elimination of the hardware based wavefront sensor, and to some extent the ability to locally counter non-common path aberrations, because it is the image itself which is being optimized. At the current time there are two primary disadvantages. The first is the requirement for high speeds. The image improvement is strongly dependent on a strong and relatively stationary signal so that the control algorithm can improve the image over multiple iterations in the optimization loop. The requirement for a strong signal is difficult when imaging a layer or tissue that does not have a strong index of refraction change or contains structures that scatter light laterally and do not guide it, e.g. the inner plexiform layer. The second is the need for a relatively stable image over the time scale of the search for an optimum image quality. In patients with tear film or vitreous fluctuations this may prove difficult. For the first issues however, using SAO with OCT, which can computationally provide rapid feedback for image optimization on a strongly reflecting layer, while also providing data from a weakly reflecting layer SAO is more effective however the focus will not be optimal for the weaker layer. However, the total cost of the SH sensor is relatively minor given the low cost of CMOS imaging chips.

For CAO the questions of the breadth of application are the major concern. CAO has the advantage of putting most of the cost into the main output, the imaging system. The major strength is the versatility of being able to digitally focus and to vary the computed aberration correction post acquisition. In addition, because CAO is compatible with OCT, it is well situated to benefit from changes in technology that

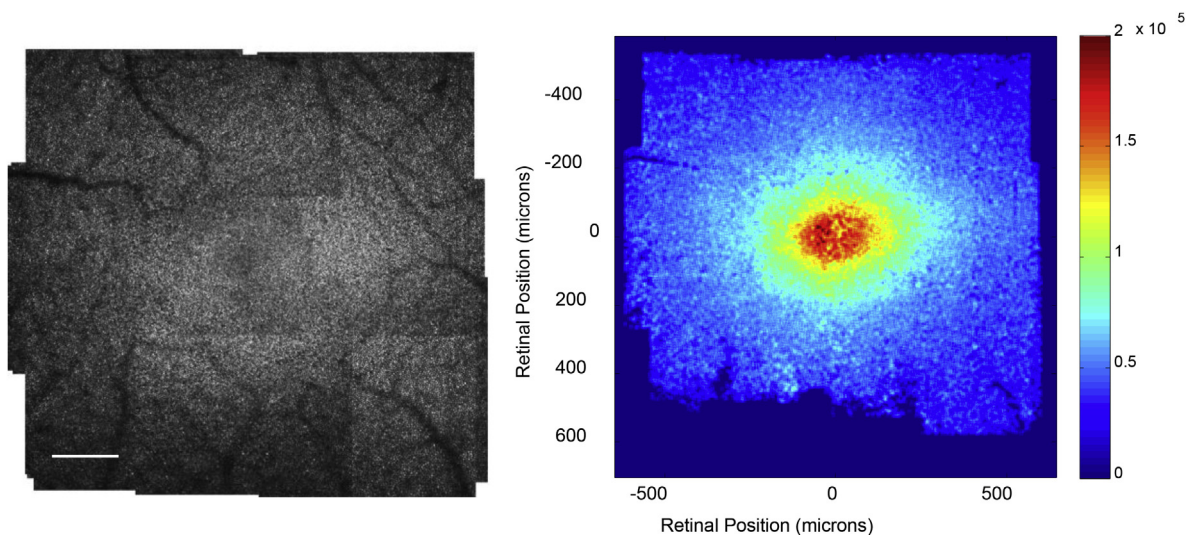


Fig. 8. Left: Montage of AOSLO cone photoreceptor images obtained over the central 1 mm of the retina in a normal subject. Right: Cone density plot, based on semi-automated identification of all cones in the image on the left. The density plot shows the horizontal/vertical asymmetry in cone packing density. Scale bar 250 μm .

are driven by the economic push for higher speed and better light sources and the continued decline in cost for computation, CAO has major strengths. What is not clear is how applicable to the clinical environment CAO will be. All data that overlap regions of interest must be collected within the time over which the phase errors of the eye are stable. In a normal, near emmetropic eyes this is achievable with fast imaging hardware. However it may be more difficult in patients with large refractive errors, or retinal problems especially those such as retinal detachments and cystoid macular edema or choroidal neovascularization which typically cause very thick retinas which vary rapidly over space and typically occur in older patients with instability of the tear film and decreased fixation stability.

3. AO based measurements of retinal structure

One of the major goals for *in vivo* imaging is to improve our understanding of retinal structure and how it is affected by biological variables such as age and sex as well as by disease processes. High resolution of AO retinal imaging provides a critical bridge between histological and animal studies in both the normal and abnormal retina.

3.1. Photoreceptors

While the initial application of AO retinal imaging was aimed at improving measurements of retinal thickness (Bille et al., 1990; Dreher et al., 1989), it was the systematic identification and quantification of cone photoreceptors that proved the value of AO imaging (Choi et al., 2005; Chui et al., 2008b, 2008c; Li and Roorda, 2007; Liang et al., 1997; Roorda et al., 2001; Roorda and Williams, 1999). Cone photoreceptors were some of the first retinal cells systematically studied using AO retinal imaging. The cones show the expected variation in packing density with retinal position (Chui et al., 2008a, 2008b; Liang et al., 1997; Song et al., 2011b), being the most densely packed in the center of the fovea, and decreasing systematically with increasing retinal eccentricity (Figs. 7 and 8). Recent improvements in AO retinal imaging has also allowed rod photoreceptor imaging (Dubra et al., 2011; Merino et al., 2011), although population statistics are not fully available.

3.1.1. Quantifying photoreceptor density and packing geometry

In a normal young adult the cone photoreceptor mosaic is densely packed in the foveal center and stable over time (Bruce et al., 2015; Pallikaris et al., 2003). There are multiple approaches to quantifying the spatial distribution of the cone photoreceptors, and the choice of technique is driven by the information that is desired. One of the most reliable, but labor intensive, approaches is to use a semi-automated procedure (Chui et al., 2008a, 2008b; Li and Roorda, 2007) in which

candidate cones are identified automatically, and checked by an experienced grader to eliminate computer errors. This approach provides stable identification over time and across instruments (Chui et al., 2008b; Song et al., 2011a). Modern algorithms are improving on the original filter based algorithms (Cunefare et al., 2016, 2017; Miyagawa et al., 2017) and can deal with multiply scattered light images of cones as well (Liu et al., 2017a). The need for operator free quantification of photoreceptor packing is being driven by the need to improve clinical evaluations and especially to provide stable, reliable, operator independent estimates of cone packing density across clinics for intervention trials.

In normal individuals the cone photoreceptor array is packed in a manner close to that expected for hexagonal close packing, with every cone surrounded by six nearest neighbors. A potential method to detect early or subtle damage to cones is to quantify the regularity of cone distribution, particularly given that there are large individual differences among normal subjects in the density and spatial distribution of cones (Section 3.1.2). This regularity can be disrupted by diseases such as diabetes, even when the density of cones is within normal limits (Lammer et al., 2016; Nesper et al., 2017). Thus, a number of approaches to characterizing the cone array have been applied including Fourier analysis, Voronoi nearest neighbor analysis, and density recovery functions or local spatial averaging. For the fast Fourier transform (FFT) analysis (Fig. 9) small regions of the photoreceptor array are analyzed using a two dimensional Fourier transform of the region of interest. The FFT analysis calculates the variation in contrast in an image as a function of spatial frequency and orientation. When cones are packed densely there should be a concentration of high frequency information at the cone spacing frequency. Thus, in Fig. 9C we see that in the two dimensional FFT there is a ring of increased spatial power with a clear hexagonal shape. If a radial average is calculated as a function of distance from the center (which represents a spatial frequency of zero), there is a clear shoulder in the power spectrum at the frequency of the cone spacing (Fig. 9D, arrow). This ring is commonly termed Yellott's ring (Yellott, 1982) and represents the fundamental spacing of the photoreceptors. The advantage of the FFT approach is that there is no need to identify the center of each photoreceptor and it is therefore quick and not susceptible to individual differences in grading. However it can be insensitive to small irregularities or individually missing photoreceptors (Cooper et al., 2016) and for noisy images Yellott's ring may not be readily identified.

Voronoi diagrams are calculated based on the relative location of the centers of the cones (Fig. 10). Cones are identified and the centers located. Coordinates of cone centers are used as the input data for the analysis. The distance from each point in the image to the nearest cone is then calculated and these distances used to partition the image into Voronoi cells. The number of sides for the Voronoi cells gives an

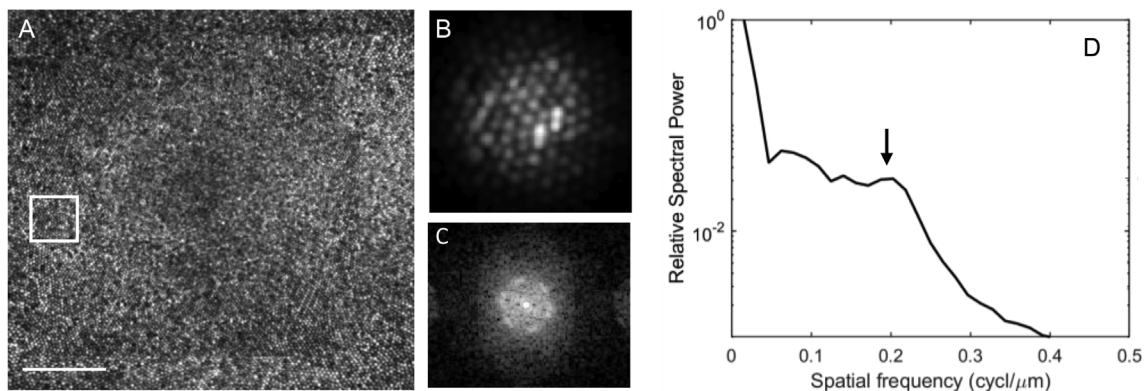


Fig. 9. Fourier analysis of cone frequency. A: an expanded view of the central region of Fig. 6 (scale bar 25) μm . Spatial frequency analysis analyzes a small regions of cones (white box), B: the selected region, multiplied by a spatial mask to avoid windowing artifacts C: the log magnitude of the Fourier transform of the area. D: the radially averaged log power of the Fourier transform showing the spatial frequency of the cone sampling array (Yellott's ring, arrow). Scale bar 50 μm .

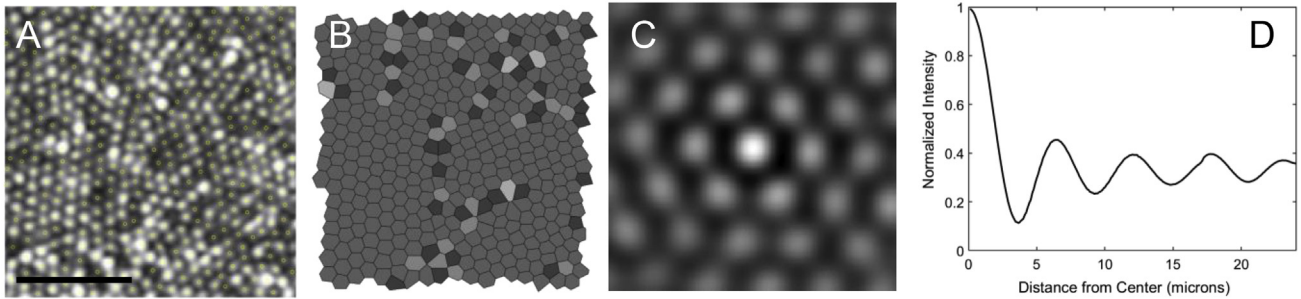


Fig. 10. Comparison of Voronoi analysis and local spatial average analysis. A: A group of cones. B: Voronoi analysis of the data in A. Here hexagonal regions are marked in a mid-gray. This region has a high degree of hexagonality (78% of regions). C: Local cone spatial average of the same region. This represents the average surround of all the cones in the analyzed region. Here we see that the array is uniform out to several rings of nearest neighbors. D: The radial average of the local cone spatial average, showing the regularity of the sampling array over this region. Scale bar 10 μm .

estimate of the type of packing. In a perfect hexagonal array, 100 percent of the cones would have six nearest neighbors, and in some regions of the normal retina hexagonal packing is high (Fig. 10B). Because it provides a measure of the packing regularity as well as the spacing Voronoi analysis is widely used for characterizing the cone mosaic (Cooper et al., 2016; Curcio and Sloan, 1992; Li and Roorda, 2007; Lombardo et al., 2013c, 2014b).

The density recovery function (Cooper et al., 2016; Rodieck, 1991; Roorda and Williams, 1999) and local cone spatial average (Sawides et al., 2017a) are closely related, although they supply slightly different information. For both measures the location of cones are identified as in Voronoi analysis. For the density recovery function the distances between all cones is computed, and the shortest distances for each cone is averaged, giving an estimate of the minimum inter-cone distance. For the local cone average (Fig. 10C) a region of interest around each identified cone is extracted, and then the local cone spatial average is simply the average of all ROI's. The advantage of these measures over the Voronoi analysis is that not every cone needs to be identified, allowing a more conservative algorithm for cone identification to be used, trading off sensitivity for specificity. For the local spatial average the analysis provides a snapshot of the average local environment for each cone, so additional calculations can be made, including spacing (Fig. 10D), local orientation and orientation anisotropy (Sawides et al., 2017a).

While high quality histological data (Curcio et al., 1987, 1990; PandaJonas et al., 1995) are available, the ability to make measurements in targeted subject groups is not possible with histology. AO measurements of cone distribution in normal individuals agree well with histology (Chui et al., 2008b, 2008c; Legras et al., 2018; Liang et al., 1997; Song et al., 2011b; Zhang et al., 2015b) and there is an

increasing understanding of the sources of individual variations both across the retina and between individuals. Thus, the distribution of cones decreases more gradually moving from the fovea into the periphery along the horizontal meridians than the vertical meridians (Chui et al., 2008a, 2008b; Legras et al., 2018; Li et al., 2010b; Lombardo et al., 2013a, 2013c; Sawides et al., 2017a; Song et al., 2011a; Zhang et al., 2015b) (Fig. 8). As a result isodensity contours are elongated along the horizontal direction of the normal retina (Chui et al., 2008a; Legras et al., 2018; Lombardo et al., 2013c; Obata and Yanagi, 2014; Sawides et al., 2017a; Song et al., 2011b; Zhang et al., 2015b), consistent with slightly higher acuities along this meridian (Woog and Legras, 2018). However, because acuity does not require a uniformly dense array of photoreceptors, the relation of cone sampling density to visual acuity is complex (Putnam et al., 2005; Wilk et al., 2017) and density is not a good predictor of cone acuity loss in retinal disease.

While the spacing of the cone sampling mosaic varies smoothly across the macula in most individuals, there are second order effects. That is, when the spectral types of cones are identified, the spatial distribution is not a regularly alternating array like a CCD chip, but has clumps of similar spectral classes (Hofer et al., 2005). Similarly the overall packing of the sampling array shows local clustering (Sawides et al., 2017a). The regularity of sampling decreases as one moves into the periphery (Li and Roorda, 2007; Wells-Gray et al., 2016), perhaps due to the increasing influence of rods being inserted into the cone sampling array (Fig. 11), as well as the influence of restrictions to retinal rearrangements imposed by the presence of the retinal vasculature.

3.1.2. Individual variation in cone photoreceptor packing density

There are large individual variations in the number of cones. While

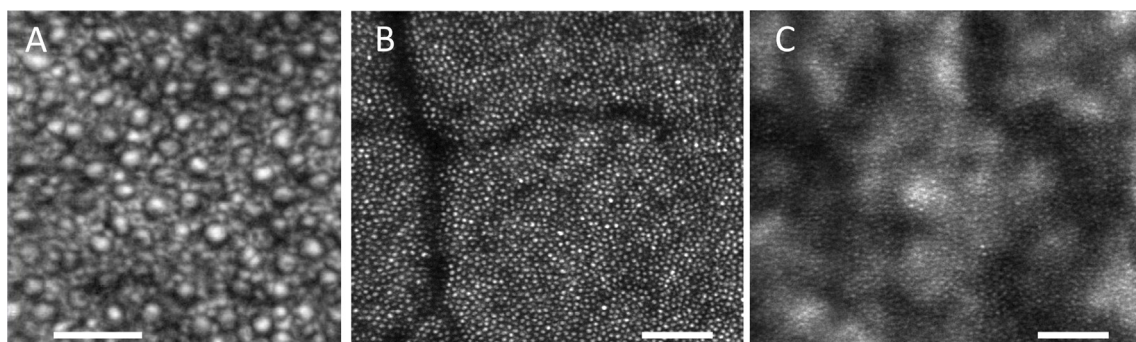


Fig. 11. Example of rod imaging and cone imaging with both confocal and multiply scattered light. A: Photoreceptor image in the near periphery of the retina. Here the cones (larger cells) are surrounded with smaller rods. B: Confocal image with a 2° field. C: The same region, imaged simultaneously with B, but using a half annular aperture for multiply scattered light detection. For the multiply scattered light image the cone inner segments are clearly visible as dots with a bright crescent opposite to the side of the half annular aperture. Note that while for the confocal image only cones are visible, for the multiply scattered light image the background of the image shows a strong contribution from choroidal scattering, most likely the site of the majority of second scattering events, when focused on the cones, with the dark regions representing the choroidal blood vessels. Scale bar in A 25 μm . Scale bars in B and C 100 μm .

many imaging systems can resolve foveal cones in most individuals, with measured densities in excess of 200,000 cones/mm² (Li et al., 2010b; Liang et al., 1997; Merino et al., 2011; Zhang et al., 2015b; Zou et al., 2011), but these systems have not found individuals with cone densities as high as the largest values measured using histology (Curcio et al., 1990) which occasionally exceed 300,000 cones/mm², (see discussion in Zhang et al. (2015b)). However these central cone densities are highly variable across individuals, perhaps due to individual differences controlling the formation of the fovea after birth. This hypothesis is consistent with the observation that the total number of cones in the central 14 degrees of retina is more constant across individuals than the density at a particular retinal location (Elsner et al., 2017; Zhang et al., 2015b). Elsner (Elsner et al., 2017) more directly tested this hypothesis by using a two factor analysis. The first is individual variations in the total number of cones, and the second factor is a relative increase in the number of cones in the fovea. The combination of factors explains the high level of variability in foveal cone density. Further, an exponential model fits the data of at least young adults sufficiently that the density of cones at any particular location can be computed from two locations differing enough in eccentricity. This analysis shows why foveal cone density may not be a good target for clinical studies, in addition to being both more variable and more difficult to measure.

3.1.3. Cone changes in aging and myopia

This increased variability for the central fovea is also apparent in aging and myopia. Thus, with increasing age, the number of cones in central 2 degrees of the retina decreases (Chui et al., 2012a; Legras et al., 2018; Song et al., 2011b). There are significantly fewer cones outside this region but the largest changes are central but the number of cones outside this region is relatively stable. The lower values in older eyes in numbers of cones outside 5 deg is readily overlooked, since the starting cone density values of young adult eyes is low. It has also been shown that thickness of the outer nuclear and Henle layer does not accurately reflect cone number (Chui et al., 2012a; Menghini et al., 2015). It is not thinned with lower cone density for either the region < 5 deg eccentricity, which is cone dominated, or for the region > 5 deg, which includes both rods and cones. A thinned layer would report loss of photoreceptor cell bodies, but instead the older eyes have thicker layers, consistent with neural remodeling. These results emphasize the need to actually count cones, such as with AO measurements, rather than obtain layer thicknesses, which may reflect neural remodeling as the cones died (Jones et al., 2016).

The lower number of foveal cones in older subjects is consistent with other measurements that suggest that with aging the center of the fovea changes shape (Gorrand and Delori, 1999), loses photopigment (Elsner et al., 1998a; Keunen et al., 1987; Nelson et al., 2005) shows

changes in macular pigment distribution (Delori et al., 2006; Elsner et al., 1998a), undergoes changes in Henle fiber distribution and central birefringence (VanNasdale et al., 2011) while the foveal avascular zone increases in size (Gong et al., 2016; Laatikainen and Larinkari, 1977). The overall picture is consistent with the fovea remodeling, perhaps as the vitreous liquefies and the inner limiting membrane becomes less elastic, flattening out, and in a sense reversing some of its structural and mechanical changes and perhaps including photoreceptor migration that occurred during foveal development in the first few years of life.

The fovea also appears to be unique in regards its response to myopic eye growth. While beyond about 2° retinal eccentricity, all quadrants of the retina (except between the disc and fovea) increase cone spacing with increasing eye length (Chui et al., 2008b; Legras et al., 2018), this is not the case in the center of the fovea (Li et al., 2010b). This suggests an interaction of the development of the foveal specialization during the first few years of life and the growth of the eye, although detailed studies of the interaction between cone packing and age of myopia onset have not yet been carried out. The nasal cone density, between the fovea and the optic nerve head also changes less than expected from a simple expansion of the posterior pole (Chui et al., 2008b). This deviation seems to be associated with the increase in the zone of peripapillary atrophy in myopic patients which tends to keep the linear distance from the fovea to the temporal edge of the retina at the disc relatively constant (Chui et al., 2011; Jonas et al., 2015) and thus the expansion of the posterior segment of the eye is not fully reflected between the optic nerve and fovea. The AOSLO can also clearly show cones surviving in myopic eyes over regions of peripapillary atrophy (Fig. 12B.) These findings are consistent with OCT data that show an external limiting membrane and outer nuclear layer within the region of peripapillary atrophy in myopic eyes (Jonas et al., 2015) and this survival of cones is similar to what is seen in outer retinal tubulations (Fig. 12C.) raising the possibility of better cone survival in retinal degenerations than might be expected from the health of the retinal pigment epithelium.

3.1.4. Retinal degenerations

As new cell and gene based therapies for retinal degenerations move from the lab to the clinic there is an increasing need for improved, cell-specific, measures of retinal damage. AO retinal imaging is an excellent candidate for this. First, AO imaging can make precise measurements of numbers and locations of cones in patients with retinal disease (Boretsky et al., 2012; Choi et al., 2006; Duncan et al., 2007; Land et al., 2014; Morgan et al., 2014; Vincent et al., 2013; Wolfing et al., 2006; Zhang et al., 2014). Second, the ability to also measure rods (Dubra et al., 2011; Merino et al., 2011; Song et al., 2018; Wells-Gray et al., 2018) (Fig. 11.) adds to the ability to see damage that is closely related to the cause of the retinal degeneration. Third, AO retinal imaging

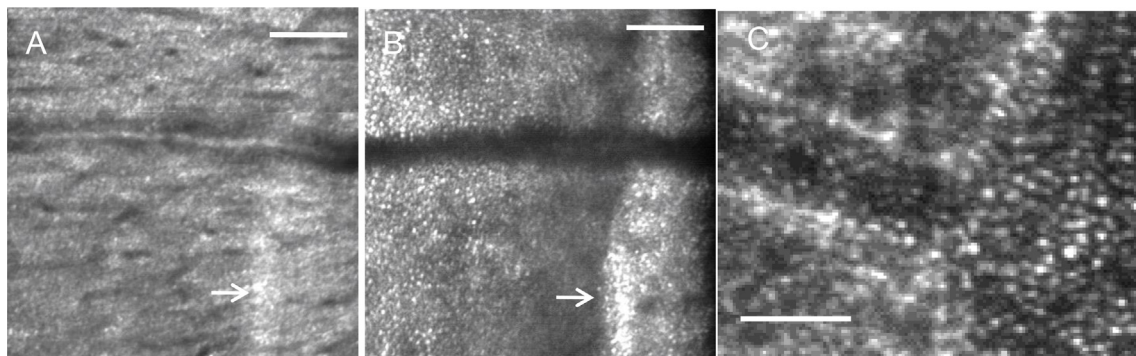


Fig. 12. Cones are seen extending out onto atrophic regions or the retina. A: An image of the nerve fiber layer at the edge of the optic nerve. B: The same retinal region as in A but now focused at the cones, showing cones extending onto the peripapillary crescent. Data replotted from Chui et al. (Chui et al., 2011), C: Cones in an outer retinal tubulation showing the bright cones extending out across a regions of atrophy. Data replotted from King et al. (King et al., 2017). Scale bars in A and B 100 μ m. Scale bar in C 25 μ m.

systems can either directly test visual sensitivity or alternatively can be related easily to other measures of sensitivity to compare structural and functional changes (Chen et al., 2011; Choi et al., 2006; Talcott et al., 2011). Fourth, AO imaging can be used to discriminate cone loss from abnormalities leading to loss or abnormalities of the cone outer segments. For instance, in some phenotypic color deficiencies, the genetic defect results in the formation of cones, but the outer segments are abnormal and the cones appear dark, whereas in other genotypes the cones are missing (Carroll et al., 2004). This ability has been enhanced by the development of multiply scattered light imaging of cones (Figs. 11C and 12), which reveals the inner segments even when outer segments are lost (King et al., 2017; Langlo et al., 2016; Scoles et al., 2014, 2016, 2017; Tanna et al., 2017). Another important advantage is that AO imaging has shown that in the normal population cone numbers are stable over the time course expected for clinical trials (Bruce et al., 2015; Talcott et al., 2011) and thus, cell loss can be measured with exquisite sensitivity. Since many of the retinal degenerations also are intimately related to RPE defects, multi-modal AOSLO systems are able to measure RPE cells (see below) in the same system used for photoreceptor imaging (Chen et al., 2011; Morgan et al., 2009; Rossi et al., 2013; Tam et al., 2016). And these can also be directly related to OCT measures, which are increasingly being integrated into the same system (Zhang et al., 2014). This ability is being increasingly incorporated into clinical studies, most notably into studies of the efficacy of gene therapy and other interventions (Morgan, 2016; Morgan et al., 2014; Talcott et al., 2011) and a number of recent reviews (Carroll et al., 2013; Godara et al., 2010; Lombardo et al., 2013b; Paques et al., 2017) have summarized the promise of this approach. In the case of gene therapy or other approaches attempting to either rescue or prevent further loss of photoreceptors, directly quantifying photoreceptors is desirable for measuring outcomes.

3.1.5. Diabetes

While diabetes has often been considered to primarily affect the inner retina, there is growing evidence that the outer retina is also majorly involved in diabetic eye disease (Du et al., 2013; Elsner et al., 1987; Kern and Berkowitz, 2015; Lammer et al., 2016; Lombardo et al., 2014a; Sawides et al., 2017b; Scarinci et al., 2016; Soliman et al., 2016; Tan et al., 2015; Zaleska-Zmijewska et al., 2017). This is seen as either decreases in cone numbers (Lombardo et al., 2014a; Soliman et al., 2016), or as increased irregularity of cones (Lammer et al., 2016; Nesper et al., 2017) in eyes with diabetes. While some cone changes seem to be related to changes in the deep vascular plexus of the inner retina (Scarinci et al., 2016), this is clearly not always the case. We have found areas of less reflective cones in about 25% of diabetics (Sawides et al., 2017b) (Fig. 13C.). These areas are not directly related to

overlying vascular changes in the inner retina, and many are in the foveal avascular zone, i.e. no retinal vessels near them. Rather, because the photoreceptors exist at the watershed between choroidal and retinal circulations, abnormalities in either, or even in the intervening environments can put the cones at risk. The retinal circulation is not the only ocular circulation impacted in diabetes. The blood brain barrier properties of the RPE are impacted (Cao et al., 1998; Kirber et al., 1980; Xu and Le, 2011) as well as changes to the choroid and choriocapillaris (Enzsoy et al., 2014; McLeod and Luty, 1994; Murakami and Yoshimura, 2013). Thus, there seems to be influences of both the high metabolic demand of the photoreceptors and limited support circulation, making them sensitive to changes in both the retina and choroid. In addition diabetes is also neurodegenerative (Antonetti et al., 2006; Barber, 2003; De Clerck et al., 2015; Lieth et al., 2000; Moran et al., 2016) and changes to the cones and RPE may arise from this aspect of diabetes and AO retinal imaging has the ability to tie together changes across both neural and vascular systems in the retina.

3.2. Retinal vasculature

The retina represents a prime target for looking at the impact of both systemic and retinal disease on the vasculature of the central nervous system (CNS) (Bosetti et al., 2016; Ikram et al., 2013; Rizzoni et al., 2018). For this reason the retinal blood vessels are a major target for developing biomarkers for systemic diseases such as hypertension and diabetes with target measurements including vessel caliber, vascular perfusion, blood velocity or flow, oxygen saturation or uptake as well as the autoregulation of vascular parameters (Agabiti-Rosei and Rizzoni, 2017; Antonetti et al., 2006; Cheung and Wong, 2008; Elsner and King, 2015; Ikram et al., 2013; Klein et al., 2004, 2010; Lin et al., 2016; Ong et al., 2013; Rizzoni et al., 2012; Roy et al., 2011; Sun et al., 2009; Witt et al., 2006; Wong et al., 2002).

A critical factor in understanding the results of vascular measurements in the retina is that the small size of retinal vessels puts them in the domain of the systemic microvasculature. In this size domain the relative size of the red blood cells, the influence of the vascular walls, and the viscosity of the blood become important. Many of the assumptions that allow simplifications for larger vessels are not valid in the retina (for a recent review see Secomb, 2017). Thus, in the retina the variation of velocity within a blood vessel is much blunter than expected from the parabolic profile predicted by Poiseuille flow (Logean et al., 2003; Zhong et al., 2011), and the velocity profile within a given vessel varies with the phase of the cardiac cycle (Zhong et al., 2011) showing a strong interaction of velocity and hemodynamics. In addition, viscosity of blood for these vessels is effectively lower than for bulk blood, because cells tend to separate into channels, an effect

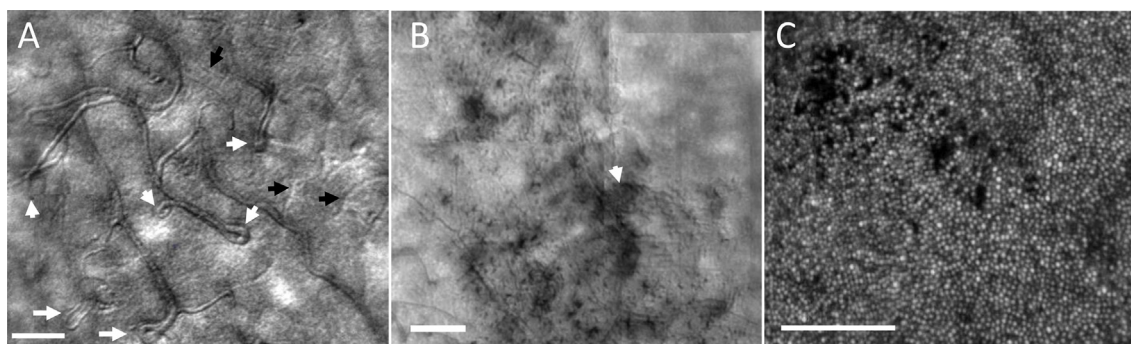


Fig. 13. A comparison of some of the structural changes in diabetic retinopathy. While typically we grade the retina on inner retinal changes, there are also changes occurring deeper. A: An example of a region of multiple vascular anomalies, including looping and doubling of capillaries (white arrows) and non-perfused capillaries (black arrows) in early diabetic retinopathy. B: A region of microcystic changes (dark regions), not visible at normal magnification but seen with AO retinal imaging. There is a small capillary loop present at the edge of the foveal avascular zone. C: The localized regions of dark cones apparent in about 25% of diabetic patients. The failure to guide light is consistent with an early stage of failure of the outer blood retinal barrier. The large region in the top center has been present for 3 years (Sawides et al., 2017b). All images have been scaled for display, with the cones imaging using a logarithmic reflectance scale. Scale bars for all panels 100 μm .

known as the Fahraeus-Lindquist effect (Fahraeus and Lindqvist, 1931; Pries et al., 1992; Pries and Secomb, 2005). The decreasing viscosity has an impact on vascular branching patterns (Luo et al., 2017), causing the branching pattern to deviate from the predictions of Murray's Law (Murray, 1926a; b) and making it sensitive to changes in the blood composition. For even smaller vessels the viscosity increases again, because the red blood cells begin to interact significantly with the walls of the capillaries (the reverse Fahraeus-Lindquist effect). Because of these differences in behavior for microvessels, the retina represents a powerful testbed for examining the impact of systemic disease on the microcirculation in the central nervous system. Factors changing the endothelial cells, hematocrit, and red blood cell rigidity can all be expected to cause major changes in the vascular properties. AO imaging now allows us to investigate these processes in detail, as well as the biological impact of disease on the structure of the microcirculation (Fig. 13). Measurements of vascular wall structure are sensitive to hypertension (Arichika et al., 2015; Burns et al., 2014b; Hillard et al., 2016; Koch et al., 2014; Meixner and Michelson, 2015) and diabetes (Burns et al., 2014b). With AOSLO these microvessels can be studied over time in humans during treatment, which enables improved understanding of the changes in perfusion at the capillary level (Chui et al., 2016; Tam et al., 2012). Interpretation of the relation between vascular wall measurements, blood pressure, and retinal blood flow is complicated by the somewhat unique environment of the eye. This is because the flow of blood out of the eye, through the central retina vein, is controlled by a variable resistance arising from venous pulsations (Morgan et al., 2016). These pulsations cause the overall resistance to flow to arise from an interaction of cerebrospinal fluid pressure, blood pressure, and the interocular pressure and this may contribute to venous pulsatility in flow.

3.2.1. Morphological and functional measures of retinal vasculature

One of the primary functions of the retinal vasculature is the distribution of the blood across the retina, allowing retinal tissue to be perfused. Because blood and blood vessels scatter light significantly, and also filter wavelengths, decreasing visual sensitivity (Remky et al., 1996), there is a need to displace the majority of inner retinal cells away from the center of the fovea (Fig. 14). Thus, the size of the foveal avascular zone is closely related to the amount of inner retinal tissue present at the edge (Chui et al., 2014a). When the tissue reaches a thickness of approximately 60 μm , there is a need to provide blood vessels to support that tissue. This supports the concept that evolution has balanced the need to provide nutrients to neural tissue, and the need to minimize light scattering from red blood cells and vessel walls. Thus, the retina seems to operate near a critical density of vascularity (Fu et al., 2016) and this makes it very sensitive to vascular diseases. While this sensitivity has been long-recognized, it was not until the

development of fluorescein angiography that it was possible to routinely visualize and measure retinal perfusion. This was first accomplished with a fundus camera (Novotny and Alvis, 1961). With the later development of video fluorescein, angiography, especially when accomplished with an SLO (Gabel et al., 1988; Wolf et al., 1989), it became possible to combine vascular distribution with flow dynamics (see below). However, fluorescein requires injection or drinking of the dye, and there have been ongoing efforts to develop non-invasive measures of retinal perfusion. Early attempts used speckle reduction (Briers and Fercher, 1982; Fercher and Briers, 1981), a technique that has been used with both small field SLO measurements (Michelson and Schmauss, 1995; Michelson et al., 1996) and wider field stabilized SLO measurements (Ferguson et al., 2004). This technique, when performed with OCT has now become widespread, implemented as OCT angiography (OCTA) (Kashani et al.; Makita et al., 2006; Spaide et al., 2018). AO retinal imaging provides much of the same capability by using moving blood cells as a contrast agent, and thus allows mapping perfused retinal vessels at high resolution (Chui et al., 2012b, 2012c, 2014b; Sulai et al., 2014; Tam et al., 2011a). However, while these maps provide more detail and often better spatial resolution than available with OCTA (Fig. 14), they require more time to acquire due to the small field size of AO-corrected imaging and thus are most appropriate for focused questions and detailed analysis of capillary changes in disease. It is possible to combine direct AO visualization of structural blood vessels with perfusion mapping (Figs. 6C, 14 and 15, 16) to identify non-perfused capillaries (Fig. 15), which can be common even in early diabetic retinopathy (Burns et al., 2014b). It is also possible to use dual channel imaging to measure blood velocity within the capillaries (de Castro et al., 2016) (Fig. 16).

Another commonly used measure of vascular health is the change in vascular wall thickness, since hypertension and diabetes increase vascular wall thickness. (Izzard et al., 1996; Rizzoni and Agabiti-Rosei, 2012). Clinically this has often been done by estimating the width of the bright stripe seen down the center of retinal arteries (Fig. 17). The width of this bright stripe is often used as a sign for vascular disease, since in severe disease it changes significantly. Because of this appearance, the arterial light reflex can be mis-interpreted as an estimate of the size of vascular lumen and the walls of the blood vessels to correspond to the darker regions. However, this is clearly not the case, as has been demonstrated with fluorescein angiography and advanced imaging techniques including flowmetry (Michelson et al., 2007; Rizzoni et al., 2012) and polarimetry (Weber et al., 2004). The bright stripe is also not as straightforward as a simple reflective image of the pupil. The reflection from the surface actually forms a narrow stripe (Brinckmannhansen, 1986). AO imaging clarifies that much of the central bright region of the blood vessel arises from reflections from moving erythrocytes as they flow through the vessel (Fig. 17). The

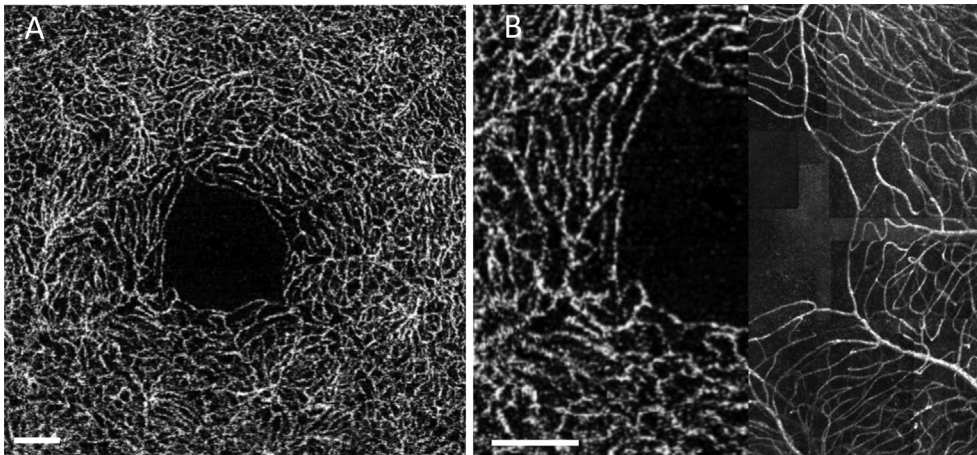


Fig. 14. Foveal avascular zone maps from a normal subject obtained using clinical OCT-A and adaptive optics imaging. A: Heidelberg Spectralis OCTA imaging. B: Split image with the left region being a magnification of the central fovea from panel A and the right being the vascular map obtained using a laboratory based AOSLO using offset pinhole detection. In both cases the superficial vascular plexus was used. Almost all vessels are visible using the OCT-A, however the exact locations and some vessels which are within 20 μm are not well resolved with the clinical instrumentation. Scale bars are 200 μm .

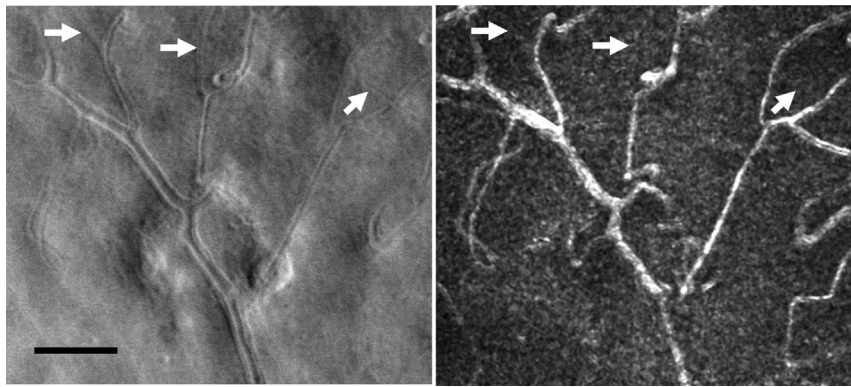


Fig. 15. Detection of non-perfused capillaries with half annulus contrast image (Sapoznik et al., 2018). Left: AOSLO image of a diabetic subject. Right: the vascular map obtained simultaneously. White arrows point to capillaries visible in the structural image but lacking flow. Scale bar 100 μm .

reflection from the cells is dependent on velocity, and thus it can be seen that the width varies with the cardiac cycle (Fig. 17). This variation in the velocity profile was investigated in detail (Zhong et al., 2011) and is discussed below.

Blood vessel wall thickness co-varies with the vessel size, with large lumens requiring thicker walls (Fig. 18). This is typically expressed as the wall to lumen ratio (WLR). WLR is related to severity of disease. AO retinal imaging has improved WLR measurements in several ways. First, it has improved the precision of the measurements. With the increased resolution, and the ability to average at several locations along a small region of blood vessel provides sub-micron accuracy. This increased accuracy, as well as the improved visibility provided by AO retinal imaging (Fig. 18), allows WLR measurements even in human small blood vessels (Arichika et al., 2015; Burns et al., 2014a; Hillard et al., 2016; Koch et al., 2014; Meixner and Michelson, 2015). Second, because the retina presents a range of more than a log unit of lumen diameters, it is possible to fit the relation between diameter and wall thickness. This relation has very little variability in normal eyes (Fig. 18C). Thus patient data can be compared to the function, controlling for variations in vessel size. This decreases the impact of individual variations in the branching pattern as well as the size of vessels, WLR and related measures such as the inner diameter can significantly vary when made at a standard retinal location. Computing a functional relation between diameter and wall thickness allows derivation of a wall index, and this allows combining measurements across a larger number of blood vessels within eyes, giving more robust measures of differences between individuals (Hillard et al., 2016). Finally, the use of improved imaging techniques also allows the identification of individual mural cells (Chui et al., 2013; Sapoznik et al., 2018) (Fig. 17). While this has not yet been used for clinical investigations, both pericytes and vascular endothelial cells are impacted by diabetes (Kern and Engerman, 1995; Lorenzi and Gerhardinger, 2001; Mizutani et al., 1996; Yamagishi and Imaizumi, 2005).

The range of vascular changes in the diabetic eye is much greater for some patients than is anticipated from the broad clinical classification such as mild non-proliferative diabetic retinopathy (Burns et al.,

2014a). Even in mild nonproliferative retina, AO reveals a wide range of changes to the blood vessels of the retina. These include small microaneurysms (Fig. 13), not resolved with wide field techniques, capillary loops and tangles, non-perfused capillaries, increased wall thickness, and vessel diameter changes (Figs. 18 and 19), along with changes to larger vessels that are seen on wide field images. The development of capillary loops and tangles, which require not only endothelial cell proliferation but also migration and tubule formation provides an outcome measure of more severe damage than microaneurysms, which indicate endothelial cell proliferation. Microcysts (Fig. 13B) are readily seen on AOSLO, which cannot be readily detected with wide field imaging. Using multiply scattered light imaging, subtle fluid leakage is seen on AOSLO that is not always detected with OCT, which is insensitive to multiply scattered light. Many of these can be seen in a 2 deg retinal region (Fig. 19). These results argue for better clinical classifications. In addition, more precise outcome measures are available with AOSLO imaging for targeted treatments, requiring fewer patients and available for *in vivo*, human studies.

3.3. Retinal ganglion cells and the nerve fiber layer

AOSLO imaging gives superb visualization of the retinal nerve fiber layer allowing identification of fibers as they interdigitate at the raphe (Huang et al., 2014) as well as the variations in reflectance with glaucomatous damage, even when visual function loss is mild (Hood et al., 2017; Huang et al., 2015). AO also can show sequelae of glaucoma occurring in the deeper retina (Choi et al., 2011) whether from retrograde affects or other causes. AOSLO allows imaging across the extent of fiber damage using montaging (Huang et al., 2014). AO-OCT can provide full 3D measurements on individual bundles (Dong et al., 2017; Kocaoglu et al., 2011) as well as of individual ganglion cells (Liu et al., 2017c), AOSLO multiply scattered light imaging also allow enface imaging of cells in the ganglion cell layer of the retina (Rossi et al., 2017; Sapoznik et al., 2018). In diseases causing acute damage to the nerve fiber layer, such as a cotton wool spot, this imaging mode can reveal the sequential development of small cell damage, presumed to be

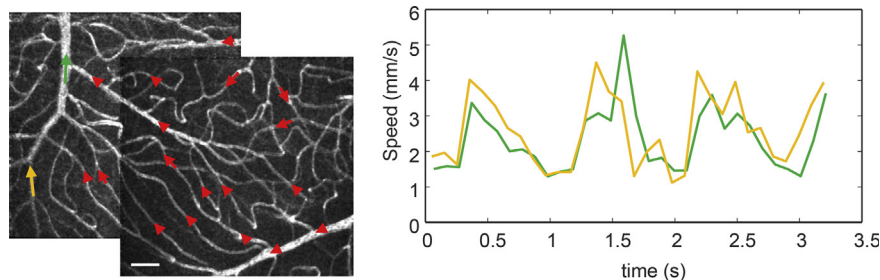


Fig. 16. Combining perfusion maps with time resolved velocity measurements. Left: An example of a region of the superior vascular plexus where vessels determined by the motion of red blood cells. Arrows indicate the direction of flow from the arteriole (bottom right) towards the venule (top left). Right: Blood velocity measurement in two venules (indicated by the color of the arrows). The pulsatility and velocity in these two venules are similar, even though they are at different levels of the vascular tree, presumably because the increase in size of the venule is sufficient to carry the converging flows from the capillaries. Scale bar 50 μm .

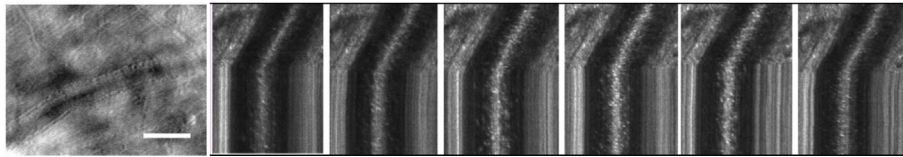


Fig. 17. Left: The walls of the retinal vessels and even the cellular components of the walls can be visualized with multiply scattered light imaging. Right image sequence: With confocal imaging and many clinical instruments however a bright stripe is often seen in the center of the arteries. This arterial reflex appears to be related to the velocity of red blood cells. As

shown here the stripe varies during a single cardiac cycle starting at a velocity minimum (diastolic) on the left, through a peak at the systolic phase and back to a trough, as seen by the slope of individual red blood cells moving across the stabilized line (see discussion under blood flow). Scale bar 100 μm .

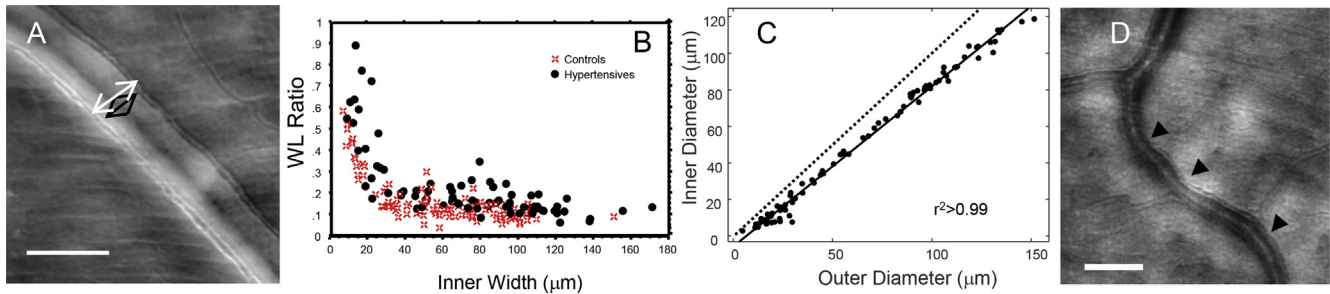


Fig. 18. Examples of wall to lumen ratio measurements using AOSLO measurements. A: An arteriole in a subject with hypertension measured using a split annular aperture. Arrows indicate the outer and inner edges of the walls. B: A set of measurements in control and hypertensive subjects showing the strong covariance between the vessel lumen (inner width) and the wall to lumen ratio. This covariance adds noise to clinical measurements unless matched samples are used. C: For normal subjects measuring the walls over the entire range of sizes available demonstrates that inner and outer arterial diameters are tightly controlled. The dashed line shows a slope of 1, so the deviation from that slope illustrates the relative increase in wall thickness with increasing vessel size. Comparing patient results to the linear fit (solid line) normalize the data, increasing the statistical power of measurements (Hillard et al., 2016, data replotted from Hillard et al., 2016). D: The walls of diabetic subject are also thickened and similar techniques can be used to reduce the data but in addition they often show variability in the mural cells (black arrows). Scale bars 100 μm .

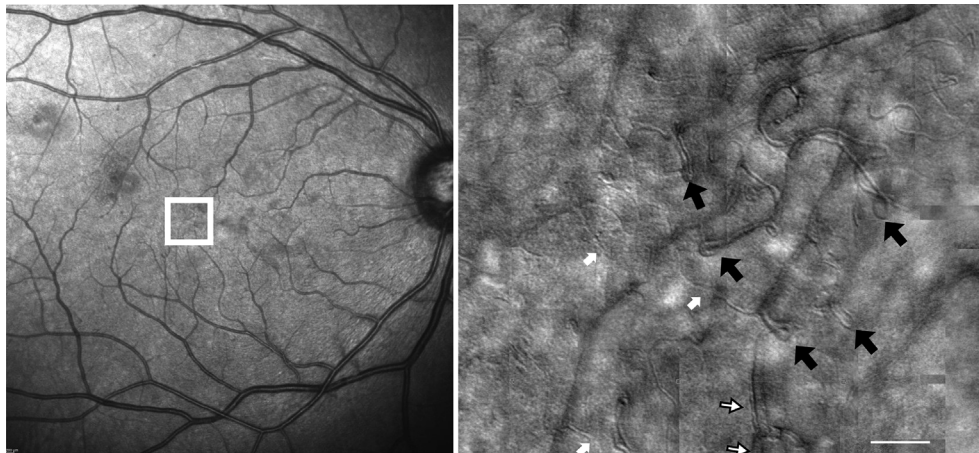


Fig. 19. Comparison of standard fundus view and AO retinal imaging of a diabetic retina. Left: Heidelberg near infrared SLO image of the retina of a 36 year old diabetic female showing a few local changes. Right: the highly magnified AOSLO image of a small region of the retina shown in the white box. Here a single region shows abnormal vessel walls (open black arrows), capillary loops and tangles (black arrows), and non-perfused capillaries (white arrows). Also shown are areas of wall thickening (white arrows with black outlines), which seems to co-locate with other retinal changes. Scale bar 100 μm .

apoptotic ganglion cells (Fig. 20) that peak at about 9–10 days after the insult and are gone in about a month.

3.4. Retinal pigment epithelium

While RPE can be seen in some patients using multiply scattered light (Scoles et al., 2013), routine reflectance based clinical imaging of RPE has not been possible with the AOSLO. The reason for this is not clear, although it is apparently related to the interdigitation of the photoreceptors with the RPE, since when photoreceptors are either not present (Chui et al., 2011; Roorda et al., 2007), or are separated from the photoreceptors by a fluid layer (Fig. 21), the RPE cells can be readily visualized. While reflectance based AO-OCT imaging has demonstrated RPE reliably (Liu et al., 2016), it has not been reliable with the AOSLO. With the AOSLO the most reliable methods for RPE visualization has been to use fluorescence as a contrast mechanism. There are two ways to do this, using the intrinsic fluorescence of lipofuscin (Morgan et al., 2009; Rossi et al., 2013; Song et al., 2014), and using ICG to stain the RPE cells (Tam et al., 2016).

3.5. Mural, glial and other retinal cells

It has long been recognized that glial cells and some of their processes can be visualized in the retina. While precise histological confirmation is generally not available, the Gunn dots are generally believed to represent reflections from the endfeet of a population of Muller cells near the optic nerve. Also visible in this region are small bright cells along the surface of the retina that appear to be microglia, as well as subcellular specializations contacting the arteries, that appear to be glial processes (Fig. 22).

4. AO based measurements of retinal function

4.1. Changes in reflectance with visual stimulation

The best studied imaging approach for measuring the physiology of the eye is retinal densitometry. In retinal densitometry the change in reflectance of the retina from dark adapted to light adapted conditions is measured. If the only change is due to the action spectrum of

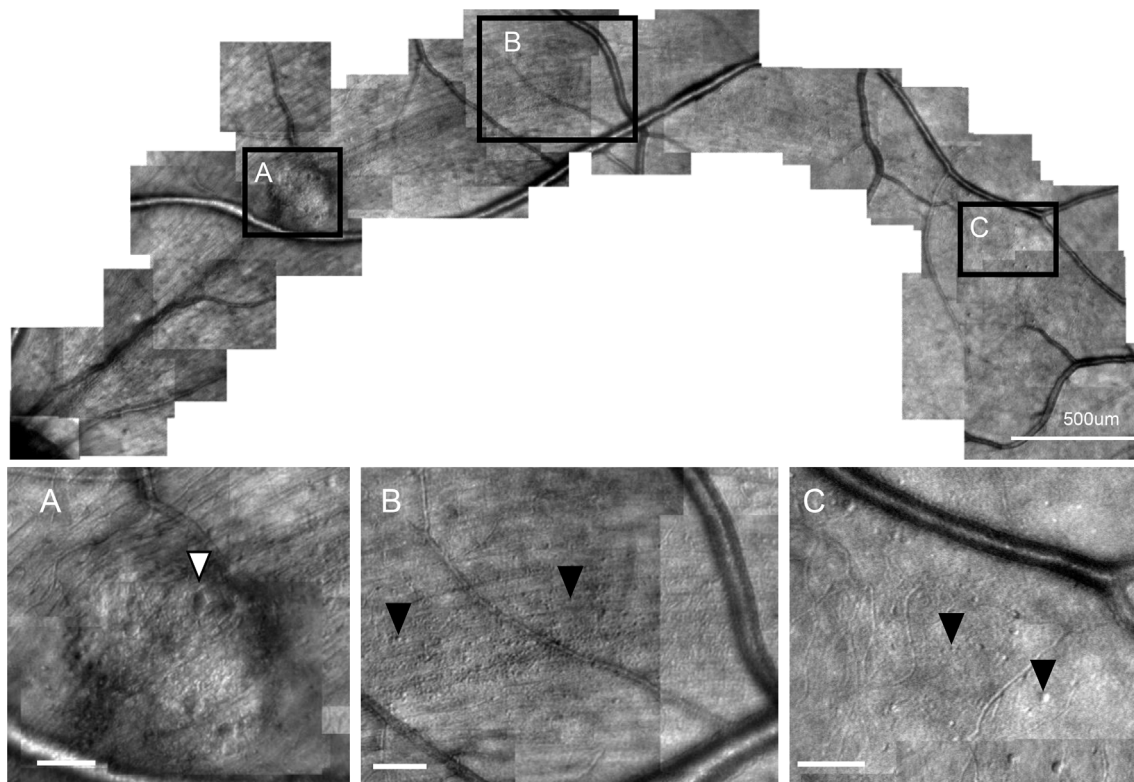


Fig. 20. Examples of cotton wool spot (CWS) eleven days after the initial vascular event. Top: the extent of the damage can be seen coursing from the optic nerve, up to the CWS (small box A), and out across the retina. Scale bar 500 μm . A: At the location of the CWS cytooid bodies can be seen (white arrow). Further from the CWS fields of small round spots were seen (boxes B and C, black arrows). These are presumed apoptotic ganglion cells and the fall solely along the nerve fiber bundles passing through the CWS and peaked about 9 days after the CWS spot occurred and then decreased in number to close to zero at 30 days after the insult. Scale bars for A, B and C 100 μm .

photopigment absorption and activation, then one can use such measurements to determine the relative change in photopigment. This was done first with spot reflectometers (Krauskopf, 1965; Norren and van der Kraats, 1981; Rushton, 1958) and starting in the 1980's with imaging systems (Elsner et al., 1992a; Faulkner and Kemp, 1984; Kilbride et al., 1983; Norren and van der Kraats, 1989). With the development of AO assisted imaging it became possible to use this differential change in reflectivity to identify the types of cones, and to study the distribution of long wavelength sensitive (LWS), middle wavelength sensitive (MWS), and short wavelength sensitive (SWS) cones at the single cell level within the living retina (Hofer et al., 2005; Roorda and Williams, 1999). While it had been known since the work of Rushton and Baker (1964) that there were large individual differences the AO studies were able to identify the cells and to investigate aspects of the spatial distribution of groups of photoreceptors and the potential impact on vision (Brainard et al., 2000).

The change in light absorption, and thus reflectance of the retina

with bleaching is not the only change that occurs with light impinging on the retina. It has been well recognized that there are changes in infrared reflectance with visual stimulation (Bedggood and Metha, 2013; Grieve and Roorda, 2008; Pepperberg et al., 1988) arising from changes related to the phototransduction cascade. In addition there seem to be changes in the effective path length of light through the outer segments with light exposure (Hillmann et al., 2016; Jonnal et al., 2007; Srinivasan and Dubra, 2016). Such changes may be arising from either changes in optical density or physical changes within the cones arising from ion flux. That the changes are related to photopigment absorption is clear, since the spectral sensitivity is most similar to the spectral luminosity function (Cooper et al., 2017). However there are also other changes that seem to occur with other visually related responses, such as increased blood flow (Pournaras and Riva, 2013; Riva et al., 1991; Zhong et al., 2012). Thus, there seem to be multiple causes of reflectance change with light exposure, and the interplay of these causes is not fully understood (Masella et al., 2014) with some being

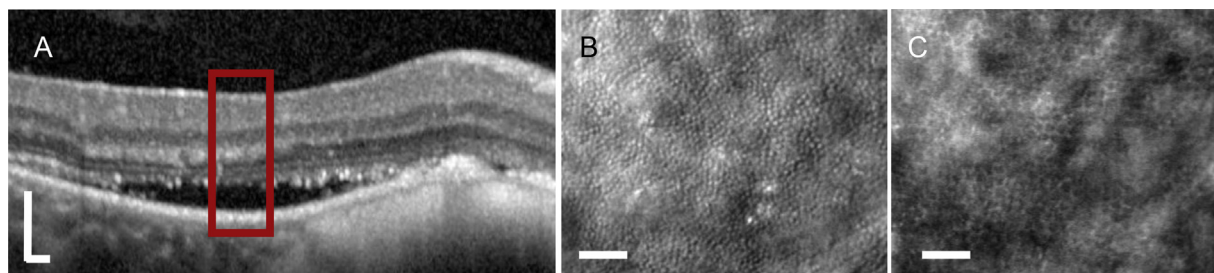


Fig. 21. Example of changes in deep retinal images in a serous detachment of the retina. A: OCT b-scan of a patient with a serous detachment secondary to a nevus. The red box indicates the approximate locations of panels B and C. B: Offset aperture images focused on the cones, showing regularly arranged mosaic of inner segments. C: Offset aperture images focused on the RPE, showing an array of RPE cells. Scale bars: A, 200 μm , B and C, 50 μm .

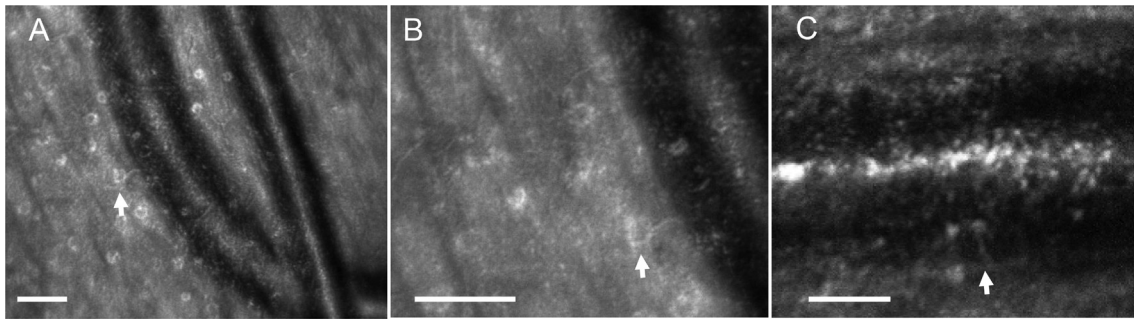


Fig. 22. Examples of putative glial cells near the optic disc. A: A series of Gunn dots imaged with a slightly offset aperture configuration. B: A more densely sampled image using a half annulus aperture, showing the cell outline and extensions to the nearby vein. C: A confocal image showing putative glial connections to a vessel. These types of connections are most common near the optic nerve. Scale bars 50 μm .

relatively slow (DeLint et al., 2000).

4.2. Stabilizing AO retinal imaging and measuring visual sensitivity

The advent of the SLO also allowed modulation of the imaging light to directly impose stimuli on the retina, while simultaneously allowing measurements of eye movements (Chen et al., 1992; Remky et al., 1996; Timberlake et al., 1982, 1986).

The advent of AO retinal imaging made controlling for the impact of eye movements critical because AO assisted SLO's have the potential to improve stimulus control (Arathorn et al., 2007; Raghunandan et al., 2008). Doing this, as well as improving the averaging and signal extraction from retinal images thus requires both knowing where the eye is pointing and how to control for motion during imaging. There are three main approaches that have been used, hardware assisted AO retinal tracking, software tracking and corrections post-acquisition. Hardware tracking (Burns et al., 2007; Ferguson et al., 2010; Hammer et al., 2003, 2006; Kocaoglu et al., 2014) has typically used measurements of a retinal feature (typically the optic nerve) at high rates, and then used close loop control of deflection galvanometers to maintain a steady position. While hardware tracking can be effective in greatly decreasing the impact of eye motions (Burns et al., 2007; Ferguson et al., 2010; Kocaoglu et al., 2014) it has not proven to be as effective as software approaches. The limitation arise from two sources. First, by adding additional control inputs and additional galvanometers, the positioning noise of the overall imaging system is increased. The second problem is that there is typically some distance between the feature being tracked (such as the optic nerve) and the region of interest. Any motions that are not compensated, such as cyclotorsion of the eye, will have an increasing impact on the stabilization of the retinal image with increasing distance. Similarly, since the tracking beam and the imaging beam will typically be at different wavelengths, there will be a variable impact of chromatic aberration on the relative locations of the two images both in terms of best focus and lateral displacement.

Software approaches, or combined hardware software approaches seem to provide the best results. In software tracking the fine scale motions of the eye are measured relative to a template image, and the displacement of small regions of the image are measured in strips, such that multiple motion estimates are made within each frame of the video (Stevenson and Roorda, 2005; Vogel et al., 2006). The system can then correct for these motions, either using a software offset (Arathorn et al., 2007; Vogel et al., 2006; Yang et al., 2010) or a combination of a software offset and hardware deflectors (Yang et al., 2014). However, the software approach also has limitations. While problems of speed have been solved, the overall degree of compensation is dependent on image quality. Thus the best stabilization tends to occur for images with a high signal to noise ratio, such as for cone imaging or nerve fiber layer imaging and where eye movements are not so large that there is insufficient overlap with the reference frame. Real time correction of retinal position in post-processing, while used extensively with wide

field fundus perimetry and microperimetry, has not been used extensively to date, despite the potential to remove responses during inaccurate tracking.

4.2.1. Stimulus presentation

One of the major uses for AO is to provide diffraction corrected visual stimuli (see Marcos et al. for a discussion (Marcos et al., 2017)). However, there is also a strong role for using stimuli not corrected with AO, but knowing where the stimulus falls. This has allowed an improved understanding that there is not a close correspondence between the point of fixation and either the center of the fovea or the peak in cone packing density (Putnam et al., 2005; Wilk et al., 2017) and investigations of small scotoma (Makous et al., 2006). It is also possible to use the AOSLO itself to present aberration corrected visual stimuli by modulating either the imaging light or another optical channel to place a stimulus on the retina (Arathorn et al., 2007; Yang et al., 2010) and target specific retinal structures (Fig. 23). This allows precise targeting of cells and testing of hypothesis about visual sensitivity. This is being used to investigate details of spatial and chromatic processing (Bruce et al., 2015; Harmening et al., 2014; Rossi and Roorda, 2010; Tuten et al., 2017) that are rapidly developing but beyond the scope of the current review.

4.3. Blood flow

The retina represents a unique opportunity to use optical techniques

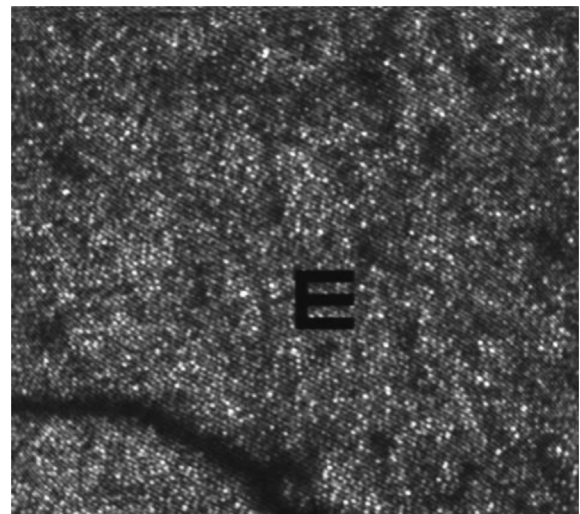


Fig. 23. An example of an AOSLO being used to present a stimulus directly to the retina by modulating the light beam. Here an AOM is modulating the light, while the retina is being stabilized using a strip based image alignment technique (Arathorn et al., 2007).

for measuring blood flow and flow regulation in the human central nervous system, shedding light on vascular hemodynamics in health and disease. AO retinal imaging is providing an improved ability to precisely characterize capillary velocity and diameter, which together determine blood flow. These measurements hold forth the promise of improved retinal capillary blood flow and shear stress and improved understanding of how they impact the eye (Fu et al., 2016; Gast et al., 2016; Lu et al., 2016b).

Initial measures of blood velocity using AOSLO arose from the realization that when imaging cone photoreceptors there are striking motions of dark and light regions which are readily visualized beneath the retinal capillaries. These moving particles allow direct measurement of the dynamics of blood flow near the fovea (Martin and Roorda, 2005, 2009) and later refinements of this technique now allow blood velocity measurements across most of the macula in vessels ranging in size from more than 100 μm to just a few μm . Imaging over the wide range of velocities and vessel sizes is done using several different techniques. Early approaches used the passage of the dye front of injected dyes, typically fluorescein (Jung et al., 1983; Wolf et al., 1994), Doppler (Leitgeb et al., 2014) velocimetry (Riva et al., 1972, 1986), Doppler flowmetry (Ferguson et al., 2004; Riva et al., 1992), OCT based Doppler velocimetry (Leitgeb et al., 2003, 2014; Yazdanfar et al., 2003) and even psychophysical techniques (Petrig et al., 1997). Most of these techniques require robust signals, and thus, other than psychophysical and fluorescein studies, have been restricted to blood vessels larger than about 50 μm . AO retinal imaging has removed that constraint. The ability to visualize individual red blood cells enables high accuracy and better understanding of the variation in blood velocity across vessels.

There are a number of AO techniques for measuring blood flow in the retina and the best technique depends on the vessels. This need for versatility arises from the dual constraints required by imaging awake behaving humans and from sampling theory. For small vessels, slight eye movements can limit what can be measured. For all vessels there is a need to consider sampling theory. This is because blood velocity in the retina ranges from less than 1 mm/s in small capillaries to more than 50 mm/s for larger vessels. Since a velocity of 1 mm/s is 1 $\mu\text{m}/\text{ms}$ it is clear that if one has a frame rate of 30 frames per second, then to use particle tracking one needs to accurately identify objects that move 30 μm . Since this is much larger than a red blood cell, the cells either need to be irregularly spaced, so one can track larger objects, such as aggregates of red blood cells, such as can occur with rouleaux, or large leukocytes. If this is not the case then an approach to use high sampling rates is needed. Both conditions occur in the human retina, as shown in Fig. 24. Here we show a single region of the retina in a normal eye. Image frames were acquired at a rate of 29 frames per second. In a region of the retina with a series of regularly spaced red blood cells (Fig. 24A, white arrows), faster sampling of the motion than 29 Hz is required because it is not possible to identify individual cells and thus motion can be aliased. However cells also aggregate into groups of red

blood cells (rouleaux) and these are often followed by plasma gaps (Arichika et al., 2014; Tam et al., 2011b). These large, irregularly spaced items as well as sparse single red blood cells and leukocytes, can be accurately followed (called particle tracking velocimetry) across AOSLO frames to obtain accurate estimates of blood velocity by examining the time vs intensity variation along a vessel (Martin and Roorda, 2005, 2009; Tam and Roorda, 2011; Tam et al., 2011b). For raster scan systems such as the AOSLO or OCT the fixed fast scan rate, using it either in one or both directions (Grieve et al., 2006; Zhong et al., 2008), provides a fundamental measurement rate for particle tracking. In practice, for large imaging angles a 30 Hz frame rate may or may not be limiting. For individual or irregularly spaced cells the cells can be tracked well at video rates. However, for a steady stream of red blood cells aliasing can occur. For instance the vessel pointed to in Fig. 24A has a steady stream of red blood cells. Since the cells are moving at approximately 1 mm/s, or 1 $\mu\text{m}/\text{ms}$, they will move on the order of 30 μm between frames. Thus, it is not possible to identify the same cell in succeeding frames, and the velocities can be aliased. Avoiding aliasing requires sampling at higher rates. This can be accomplished in several ways. Bedggood et al. used high speed flood illuminated imaging (Bedggood and Metha, 2012a, 2014). This method to date has required very small fields, much smaller than the isoplanatic angle, but has allowed detailed measurements of velocity. In an AOSLO the number of fast scan lines for each slow scan frame, can also be decreased, providing a higher frame rate but at the tradeoff of a smaller imaging field. We have used this in an AOSLO up to 120 Hz in a typical ramp scan image without major problems, and to even higher rates using a sawtooth (so each frame proceeds in the opposite direction, decreasing rebound in the slow scan mirror). The logical end point for shrinking the field is to actually stop the slow scan momentarily and to allow the motion of cells within the blood column to provide the spatial measurements. Zhong used this approach to make accurate measurements of flow with a sampling rate at the fast scan frequency. That is, if the slow scan is stopped momentarily, then the image is built up of repeated scans at the same retinal location. This generates an image with horizontal position on the x-axis and time on the y-axis, known as an XT scan. When the beam is focused on the blood vessel, the XT scan reveals bright diagonal streaks, which represent moving red blood cells. The slope of the streaks represent the change in horizontal position with time, that is, the horizontal velocity. In this approach the scan does not move, and it is the motion of cells across the scanning beam that generates the motion information (Fig. 25). Using this approach Zhong et al. (2008) measured blood flow velocity over a range of vessel sizes but the smallest sizes measured required very good fixational stability on the part of the subjects, since for vessels smaller than about 15–20 μm , even small fixational eye movements can move the vessel off of the imaging line. These authors were able to measure both the velocity profile within a vessel, documenting how the shear stress changed velocity profiles even within the cardiac cycle (Zhong et al.,

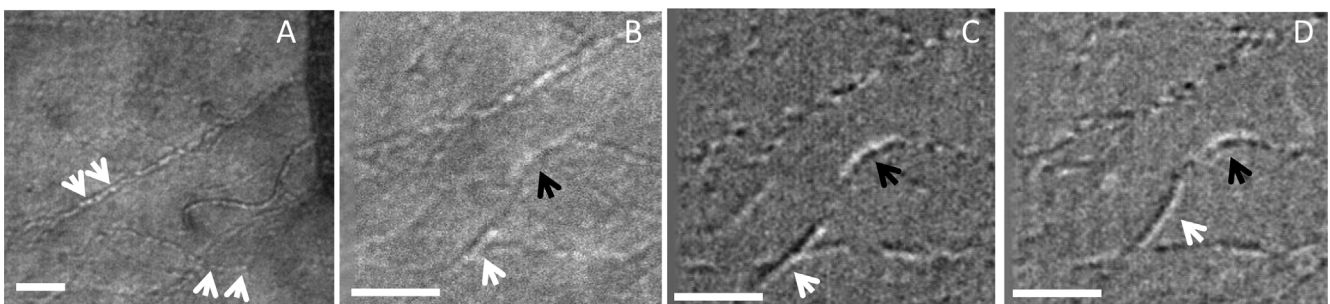


Fig. 24. AOSLO image frames collected at 29 Hz using an offset aperture. A: reflectance image showing two regions where there are continuous sequences of red blood cells moving through two capillaries (white arrows). B: A single frame subregion of A, showing both a group of red blood cells in rouleaux (black arrow) followed by a plasma gap (white arrow). C and D: Same region as in B, but now showing two sequential frames, computed by calculating the difference from the mean of 100 frames (in standard deviations). Here we can see that the motion of the rouleaux is readily measured by its change in position. Scale bars are 50 μm .

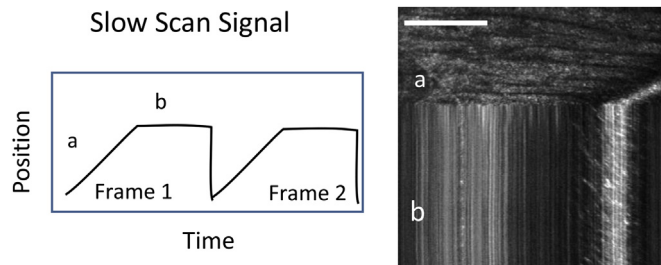


Fig. 25. AOSLO image in line scan mode. Here the slow scan position is controlled by a temporally changing voltage. Left: This voltage is programmed such that over part of the frame it follows a normal ramp (time period a), for the second part of the frame the slow scan is stopped (b). Right, the resulting slow scan pattern creates a retinal image where the top (a) is a normal view of the retina, and this allows detection of gross eye motions. The bottom portion of the image (b in right side image) has a stationary slow scan, and during this time period generates a xt image (x-position vs time) image (b). For a blood vessel that crosses the line scan, motion of particles in the x-direction create slanted lines, where the slope of the line is the horizontal component of the cell velocity. Retinal features that are not moving appear as vertical lines during this time period, allowing correction of horizontal eye motion, but not vertical motions within the frame. Scale bar 100 μm .

2011), and also to show how flickering visual stimuli as small as 2° in diameter could cause changes in blood velocity for stimuli that fell within the vascular branches of the measured vessel, but not if it was on the opposite side of the raphe (Zhong et al., 2012).

For capillaries this line scan approach is limited by small eye movements which can move the vessel on and off the scanning line. To capture the change in velocity across the cardiac cycle in a wide selection of patients, the retinal position either needs to be stabilized in real time, or a different approach is needed. A related approach without this limitation but with a somewhat lower sample rate is to generate a line illumination of the retina, and use either a linear array of detectors (Ferguson et al., 2004; Hammer et al., 2002), or an area detector with a rolling shutter configuration (Muller et al., 2013) to detect the light, an approach often referred to as line scanning. Because line scanning collects an entire row (or column) of an image at once, line rates can be much higher than with a raster scanning approach. A line scanning system can achieve high frame rates and generate near confocal

performance. A recent investigation of blood cell velocity used line scanning to capture images at 800 Hz for small fields. This high speed allowed precise measurements of cell movements (Gu et al., 2018).

Another approach to increasing the effective sampling rate is to use a dual channel offset approach (de Castro et al., 2016). Here a two channel AOSLO is used. The two channels use slightly different wavelengths, but both use an offset aperture so that detection properties (and thus images) are similar. The two channels enter the pupil at the same location but at slightly different angles such that the images at any given instant are of partially overlapping regions in the retina. For blood flow this difference is typically in the direction of the slow scan (a vertical displacement in Fig. 26), although even faster events could be captured using displacements in the fast scan direction. In Fig. 26 the two images are vertically displaced by 81 scan lines (Fig. 26 panels A and B). This means the same retinal location is imaged in each of the two channels separated by a time of roughly 5 msec. Changes between the images in the two channels represent motion or other events that have occurred within that time interval. Each frame from the two channels is then processed by computing the z-score for a change relative to the entire video sequence, for each location as shown in Fig. 26C and D). Here the red blood cells in the specified capillary for the first channel are readily detected (Fig. 26C, white arrows). The location of cells in the first channel are then found. Regions around each of these putative erythrocytes are extracted and the same region is averaged for each channel. For the first channel this produces an estimated position of the cell located in the center of the region of interest (Fig. 26E). For the other channel the same region was imaged, but due to the 5 msec delay between the two channels, the red blood cell will have moved and therefore the averaged regions will have the bright spot displaced (Fig. 26F). The displacement divided by the time is therefore the velocity in the plane of the retina along the blood vessel. In practice the progressive motion of the slow scan across the retina also has to be accounted for in the calculation. When this is done, this method gives a direct readout of velocity along the capillary (Fig. 26G). Here we see that in this pre venule capillary velocity is pulsatile because of the cardiac cycle. Within each cycle velocity ranges from 0.5 mm/s to about 1.5 mm/s.

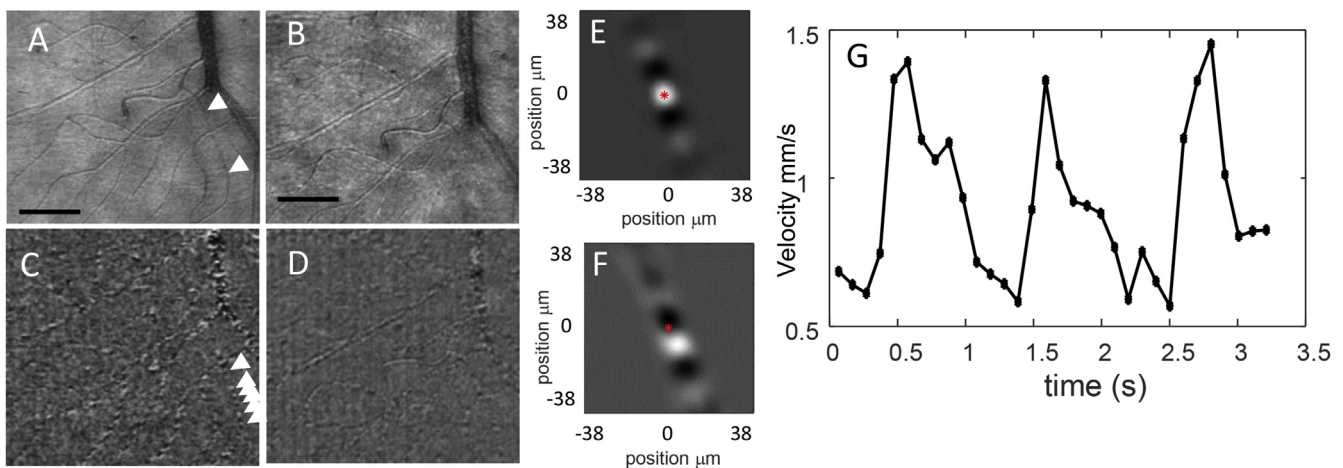


Fig. 26. AOSLO blood flow imaging using dual scanning. A: single frame offset aperture image from channel 1. B: Single frame from channel 2, captured simultaneously with A. The two channels are slightly displaced from each other at the retina, resulting in a given location being imaged at two slightly different times. In this case about 5 msec apart. C: For every pixel a z-score is computed at each point in time for the likelihood of a change. Here the z-score for the frame in A is shown. The white arrows show a group of erythrocytes in a capillary. D: The z-scores for B. E: For each detected cell in a given capillary, a region of interest is extracted with the cell at the center. These regions of interests are averaged, producing image E. F: Average of the same ROI's calculated for channel 2. Here the average shows a bright cell that is not centered, but is rather displaced from the center, with the amount of displacement indicating the difference traveled in 5 msec. G: The average velocity for the cell, averaged over 3 consecutive video frames, for the entire 3 s video, showing the pulsatile change in velocity which is at the same frequency as the cardiac cycle. Scale bars in A and B, 50 μm .

5. Current status and future directions

AO imaging has a proven ability to make research grade measurements in the normal and pathological retina. Obstacles to routine clinical measurements that existed in the first generation of instruments have mostly been overcome. It is now commonplace to make measurements quickly and effectively in patients over most of the range of refractive errors and ages. Moderate dry eye is a problem but is routinely overcome with tear substitutes. While moderate cataract remains an issue, eyes with localized cataract or irregular pupils can be imaged to good effect. Thus, at the present time AO retinal imaging can improve our understanding of the normal retina and the impact on visual system of retinal diseases. This ability will continue to be extended rapidly into clinical research. AO retinal imaging is playing an important role in monitoring both the progression and treatment of retinal degenerations. AO retinal imaging will continue to be used to investigate diabetes, AMD and glaucoma, but moving from descriptive measurements to longitudinal studies of progression. In diabetes the subclinical changes in capillary structure occurring early in the disease have been well documented and hold promise for identifying those individual most likely to progress. In glaucoma small defects in the nerve fiber layer as well as actual ganglion cells loss are being imaged and imaging will improve our understanding of the early stage of glaucoma, as well as improve the monitoring of disease progression. Similarly, AO imaging has the potential to improve our understanding and perhaps the monitoring of cerebrovascular and neurodegenerative changes occurring in the retina (Cheung et al., 2017). Finally, the ability to routinely image cones, rods and RPE cells will be an important factor in evaluating progression in macular degeneration as well as the impact of therapeutic interventions.

The noninvasive nature of AO retinal imaging means that the time course for almost any clinical intervention aimed at reducing an ongoing pathological process in the retina can be shortened and hopefully reduced in cost by the superior imaging abilities of adaptive optics. The largest remaining challenge for AO retinal imaging is to move out of the research labs and clinics and into more widespread usage. This will require continued improvements in three areas. First, while imaging sessions can now be just tens of minutes, especially if the region to be imaged is well defined, the limited field of view of AO retinal imaging restricts its use as a generalized imaging system. Second, the realization that there is much more information available than was being captured by confocal images (Chui et al., 2012b), has led to a wide range of approaches to capturing light that falls outside the center of the PSF (Rossi et al., 2017; Sulai et al., 2014). Increasingly research systems are capturing multiple channels simultaneously (Chui et al., 2012b; Sapoznik et al., 2018; Sulai et al., 2014) and because these extra detection systems do not require additional light exposure, they do not negatively impact light safety considerations. Third, the technology is inherently costly. Even though component costs are manageable, especially if suitable trade-offs in capabilities are made, the systems themselves require more components than a typical retinal imaging device and this will always impose a cost penalty. This cost penalty could be minimized, but it requires economies of scale, and for these economies to be realized will require the development of important roles for AO retinal imaging in some of the most common retinal and systemic diseases, such as diabetes and hypertension.

The technology of AO will continue to develop. As the speed of imaging and the speed of computation increases, hardware AO will continue to improve and be more capable. In addition to multiply-scattered light imaging, there is growing excitement concerning the use of single and multiphoton fluorescence imaging (Marcos et al., 2017; Pinhas et al., 2013; Sharma et al., 2016; Tam et al., 2016) to access even more cell specific information. In addition the same improvement in speed, coupled with the existing clinical acceptance of OCT provide room for computational AO to play a larger role. Because CAO techniques could be applied to clinical OCT systems, there is the possibility

of hybrid systems being developed that, while not as effective as full hardware AO, improves the current OCT in terms of the lateral resolution.

Finally, the role of AO retinal imaging in bridging research from animal models into human studies will be critical for both fundamental vision science and translational science. While beyond the scope of the current review, new modes modalities of *in vivo* imaging, including using fluorescence to follow the function and fate of cells, and to improve our understanding of basic processes are being developed and tested in other species. With the growing versatility of human imaging these advancements will allow much more direct and efficient translation of results in other species to humans.

Acknowledgments

This work was supported by National Eye Institute, United States grant EY024315.

References

- Adie, S.G., Graf, B.W., Ahmad, A., Carney, P.S., Boppart, S.A., 2012. Computational adaptive optics for broadband optical interferometric tomography of biological tissue. *Proc. Natl. Acad. Sci. U.S.A.* 109, 7175–7180.
- Agabiti-Rosei, E., Rizzoni, D., 2017. Microvascular structure as a prognostically relevant endpoint. *J. Hypertens.* 35, 914–921.
- Antonetti, D.A., Barber, A.J., Bronson, S.K., Freeman, W.M., Gardner, T.W., Jefferson, L.S., Kester, M., Kimball, S.R., Krady, J.K., LaNoue, K.F., Norbury, C.C., Quinn, P.G., Sandirasegarane, L., Simpson, I.A., Grp, J.D.R.C., 2006. Diabetic retinopathy - seeing beyond glucose-induced microvascular disease. *Diabetes* 55, 2401–2411.
- Arathorn, D.W., Yang, Q., Vogel, C.R., Zhang, Y., Tiruveedhula, P., Roorda, A., 2007. Retinally stabilized cone-targeted stimulus delivery. *Optic Express* 15, 13731–13744.
- Arichika, S., Uji, A., Ooto, S., Miyamoto, K., Yoshimura, N., 2014. Adaptive optics-assisted identification of preferential erythrocyte aggregate pathways in the human retinal microvasculature. *PLoS One* 9, e89679.
- Arichika, S., Uji, A., Ooto, S., Muraoka, Y., Yoshimura, N., 2015. Effects of age and blood pressure on the retinal arterial wall, analyzed using adaptive optics scanning laser ophthalmoscopy. *Sci. Rep.* 5, 12283.
- Arnulf, A., Dupuy, O., 1960. La transmission des contrastes par le système optique de l'œil et les seuils de contrastes rétinien. *Comptes Rendus Hebdomadaires Des Seances De L'Académie Des Sciences* 250, 2757–2759.
- Artal, P., Benito, A., Taberner, J., 2006. The human eye is an example of robust optical design. *J. Vis.* 6, 1–7.
- Artal, P., Guirao, A., 1998. Contributions of the cornea and the lens to the aberrations of the human eye. *Optic Lett.* 23, 1713–1715.
- Artal, P., Guirao, A., Berrio, E., Williams, D.R., 2001. A model to explain how the lens compensates for corneal aberrations. *Invest. Ophthalmol. Vis. Sci.* 42, 4804.
- Atchison, D.A., Smith, G., 2005. Chromatic dispersions of the ocular media of human eyes. *J. Opt. Soc. Am. a-Opt. Image Sci. Vision* 22, 29–37.
- Babcock, H., 1953. The Possibility of Compensating Astronomical Seeing, vol. 65. Publications of the Astronomical Society of the Pacific, pp. 229–236.
- Barber, A.J., 2003. A new view of diabetic retinopathy: a neurodegenerative disease of the eye. *Prog. Neuro Psychopharmacol. Biol. Psychiatr.* 27, 283–290.
- Baumann, B., Gotzinger, E., Pircher, M., Hitzinger, C.K., 2009. Measurements of depolarization distribution in the healthy human macula by polarization sensitive OCT. *J. Biophot.* 2, 426–434.
- Beckers, J.M., 1993. Adaptive optics for astronomy - principles, performance, and applications. *Annu. Rev. Astron. Astrophys.* 31, 13–62.
- Bedford, R.E., Wyszecki, G.W., 1957. Axial chromatic aberration of the human eye. *J. Opt. Soc. Am.* 47, 564–565.
- Bedggood, P., Daaboul, M., Ashman, R., Smith, G., Metha, A., 2008. Characteristics of the human isoplanatic patch and implications for adaptive optics retinal imaging. *J. Biomed. Optic.* 13, 024008.
- Bedggood, P., Metha, A., 2012a. Direct visualization and characterization of erythrocyte flow in human retinal capillaries. *Biomed. Optic Express* 3, 3264–3277.
- Bedggood, P., Metha, A., 2012b. Variability in bleach kinetics and amount of photopigment between individual foveal cones. *Invest. Ophthalmol. Vis. Sci.* 53, 3673–3681.
- Bedggood, P., Metha, A., 2013. Optical imaging of human cone photoreceptors directly following the capture of light. *PLoS One* 8, e79251.
- Bedggood, P., Metha, A., 2014. Analysis of contrast and motion signals generated by human blood constituents in capillary flow. *Optic Lett.* 39, 610–613.
- Bedggood, P.A., Ashman, R., Smith, G., Metha, A.B., 2006. Multiconjugate adaptive optics applied to an anatomically accurate human eye model. *Optic Express* 14, 8019–8030.
- Benedetti, P.A., Evangelista, V., Guidarini, D., Vestri, S., 1992. Confocal-line microscopy. *J. Microscopy-Oxford* 165, 119–129.
- Berendschot, T., DeLint, P.J., van Norren, D., 2003. Fundus reflectance - historical and present ideas. *Prog. Retin. Eye Res.* 22, 171–200.
- Berendschot, T., van de Kraats, J., Kanis, M.J., van Norren, D., 2010. Directional model analysis of the spectral reflection from the fovea and para-fovea. *J. Biomed. Optic.* 15, 065005.
- Bille, J.F., Grimm, B., Liang, J., Muller, K., 1990. Active-optical improvement of the

- spatial resolution of the laser tomographic scanner. In: Nasemann, E., Burk, R.O.W. (Eds.), *Laser Scanning Ophthalmoscopy and Tomography Quintessenz*, Munich, pp. 265.
- Blokland, G.J.V., 1986a. Directionality and alignment of the foveal receptors assessed with light scattered from the human fundus in vivo. *Vis. Res.* 26, 495–500.
- Blokland, G.J.V., 1986b. *The Optics of the Human Eye with Respect to Polarized Light*. University of Utrecht, pp. 49–79.
- Blokland, G.J.V., Norren, D.V., 1986. Intensity and polarization of light scattered at small angles from the human fovea. *Vis. Res.* 26, 485–494.
- Booth, M.J., Neil, M.A.A., Juskaitis, R., Wilson, T., 2002. Adaptive aberration correction in a confocal microscope. *Proc. Natl. Acad. Sci. U.S.A.* 99, 5788–5792.
- Boretzky, A., Khan, F., Burnett, G., Hammer, D.X., Ferguson, R.D., van Kuijk, F., Motamedi, M., 2012. In vivo imaging of photoreceptor disruption associated with age-related macular degeneration: a pilot study. *Laser Surg. Med.* 44, 603–610.
- Bosetti, F., Galis, Z.S., Bynoe, M.S., Charette, M., Cipolla, M.J., Del Zoppo, G.J., Gould, D., Hatsukami, T.S., Jones, T.L., Koenig, J.I., Luty, G.A., Maric-Bilkan, C., Stevens, T., Tolunay, H.E., Koroshetz, W., Small Blood Vessels: Big Health Problems Workshop, P., 2016. Small blood vessels: big health problems? scientific recommendations of the national institutes of health workshop. *J Am Heart Assoc* 5.
- Brainard, D.H., Roorda, A., Yamauchi, Y., Calderone, J.B., Metha, A., Neitz, M., Neitz, J., Williams, D.R., Jacobs, G.H., 2000. Functional consequences of the relative numbers of L and M cones (vol 17, pg 607, 2000). *J. Opt. Soc. Am. a-Opt. Image Sci. Vision* 17 1684-1684.
- Briers, J.D., Fercher, A.F., 1982. Retinal blood-flow visualization by means of laser speckle photography. *Invest. Ophthalmol. Vis. Sci.* 22, 255–259.
- Brinchnannhansen, O., 1986. The light reflex on retinal arteries and veins - a theoretical study and a new technique for measuring width and intensity profiles across retinal vessels. *Acta Ophthalmol.* 64, 5–8.
- Brink, H.B.K., 1991. Birefringence of the human crystalline lens in vivo. *J. Opt. Soc. Am. a-Opt. Image Sci. Vision* 8, 1788–1793.
- Bruce, K.S., Harmening, W.M., Langston, B.R., Tuten, W.S., Roorda, A., Sincich, L.C., 2015. Normal perceptual sensitivity arising from weakly reflective cone photoreceptors. *Invest. Ophthalmol. Vis. Sci.* 56, 4431–4438.
- Bueno, J.M., 2000. Measurement of parameters of polarization in the living human eye using imaging polarimetry. *Vis. Res.* 40, 3791–3799.
- Burns, S.A., Elsner, A.E., Chui, T.Y., VanNasdale, D.A., Clark, C.A., Gast, T.J., Malinovsky, V.E., Phan, A.D.T., 2014a. In vivo adaptive optics microvascular imaging in diabetic patients without clinically severe diabetic retinopathy. *Biomed. Optic Express* 5, 961–974.
- Burns, S.A., Elsner, A.E., Chui, T.Y., Vannasdale Jr., D.A., Clark, C.A., Gast, T.J., Malinovsky, V.E., Phan, A.D., 2014b. In vivo adaptive optics microvascular imaging in diabetic patients without clinically severe diabetic retinopathy. *Biomed. Optic Express* 5, 961–974.
- Burns, S.A., Elsner, A.E., Mellem-Kairala, M.B., Simmons, R.B., 2003. Improved contrast of subretinal structures using polarization analysis. *Invest. Ophthalmol. Vis. Sci.* 44, 4061–4068.
- Burns, S.A., Marcos, S., Elsner, A.E., Bara, S., 2002. Contrast improvement of confocal retinal imaging by use of phase-correcting plates. *Optic Lett.* 27, 400–402.
- Burns, S.A., Tumber, R., Elsner, A.E., Ferguson, D., Hammer, D.X., 2007. Large-field-of-view, modular, stabilized, adaptive-optics-based scanning laser ophthalmoscope. *J. Opt. Soc. Am. A, Opt. Image Sci. Vision* 24, 1313–1326.
- Burns, S.A., Wu, S., Delori, F., Elsner, A.E., 1995a. Direct measurement of human-cone photoreceptor alignment. *J. Opt. Soc. Am. a-Opt. Image Sci. Vision* 12, 2329–2338.
- Burns, S.A., Wu, S., Delori, F.C., Elsner, A.E., 1995b. Direct measurement of human cone photoreceptor alignment. *J. Opt. Soc. Am. A* 12, 2329–2338.
- Campbell, F.W., Green, D.G., 1965. Optical and retinal factors affecting visual resolution. *J. Physiol.-London* 181, 576–593.
- Cao, J.T., McLeod, D.S., Merges, C.A., Luty, G.A., 1998. Choriocapillaris degeneration and related pathologic changes in human diabetic eyes. *Arch. Ophthalmol.* 116, 589–597.
- Carroll, J., Kay, D.B., Scoles, D., Dubra, A., Lombardo, M., 2013. Adaptive optics retinal imaging - clinical opportunities and challenges. *Curr. Eye Res.* 38, 709–721.
- Carroll, J., Neitz, M., Hofer, H., Neitz, J., Williams, D.R., 2004. Functional photoreceptor loss revealed with adaptive optics: an alternate cause of color blindness. *Proc. Natl. Acad. Sci. U.S.A.* 101, 8461–8466.
- Catlin, D., Dainty, C., 2002. High-resolution imaging of the human retina with a Fourier deconvolution technique. *J. Opt. Soc. Am. a-Opt. Image Sci. Vision* 19, 1515–1523.
- Cense, B., Gao, W.H., Brown, J.M., Jones, S.M., Jonnal, R.S., Mujat, M., Park, B.H., de Boer, J.F., Miller, D.T., 2009. Retinal imaging with polarization-sensitive optical coherence tomography and adaptive optics. *Optic Express* 17, 21634–21651.
- Cense, B., Miller, D.T., King, B.J., Theelen, T., Elsner, A.E., 2018. Measuring polarization changes in the human outer retina with polarization-sensitive optical coherence tomography. *J. Biophot.* 11, e201700134.
- Chamot, S.R., Dainty, C., Esposito, S., 2006. Adaptive optics for ophthalmic applications using a pyramid wavefront sensor. *Optic Express* 14, 518–526.
- Chen, D.C., Jones, S.M., Silva, D.A., Olivier, S.S., 2007. High-resolution adaptive optics scanning laser ophthalmoscope with dual deformable mirrors. *J. Opt. Soc. Am. a-Opt. Image Sci. Vision* 24, 1305–1312.
- Chen, J.F., Elsner, A.E., Burns, S.A., Hansen, R.M., Lou, P.L., Kwong, K.K., Fulton, A.B., 1992. The effect of eye shape on retinal responses. *Clin. Vis. Sci.* 7, 521.
- Chen, Y.M., Ratnam, K., Sundquist, S.M., Lujan, B., Ayyagari, R., Gudiseva, V.H., Roorda, A., Duncan, J.L., 2011. Cone photoreceptor abnormalities correlate with vision loss in patients with stargardt disease. *Invest. Ophthalmol. Vis. Sci.* 52, 3281–3292.
- Cheung, C.Y.L., Ikram, M.K., Chen, C., Wong, T.Y., 2017. Imaging retina to study dementia and stroke. *Prog. Retin. Eye Res.* 57, 89–107.
- Cheung, N., Wong, T.Y., 2008. Diabetic retinopathy and systemic vascular complications. *Prog. Retin. Eye Res.* 27, 161–176.
- Choi, S.S., Doble, N., Hardy, J.L., Jones, S.M., Keltner, J.L., Olivier, S.S., Werner, J.S., 2006. In vivo imaging of the photoreceptor mosaic in retinal dystrophies and correlations with visual function. *Invest. Ophthalmol. Vis. Sci.* 47, 2080–2092.
- Choi, S.S., Doble, N., Lin, J., Christou, J., Williams, D.R., 2005. Effect of wavelength on in vivo images of the human cone mosaic. *J. Opt. Soc. Am. a-Opt. Image Sci. Vision* 22, 2598–2605.
- Choi, S.S., Zawadzki, R.J., Lim, M.C., Brandt, J.D., Keltner, J.L., Doble, N., Werner, J.S., 2011. Evidence of outer retinal changes in glaucoma patients as revealed by ultra-high-resolution in vivo retinal imaging. *Br. J. Ophthalmol.* 95, 131–141.
- Christou, J.C., Roorda, A., Williams, D.R., 2004. Deconvolution of adaptive optics retinal images. *J. Opt. Soc. Am. A, Opt. Image Sci. Vision* 21, 1393–1401.
- Chu, Z.D., Chen, C.L., Zhang, Q.Q., Pepple, K., Durbin, M., Gregori, G., Wang, R.K.K., 2017. Complex signal-based optical coherence tomography angiography enables in vivo visualization of choriocapillaris in human choroid. *J. Biomed. Optic.* 22, 1–10.
- Chui, T.Y., Gast, T.J., Burns, S.A., 2013. Imaging of vascular wall fine structure in the human retina using adaptive optics scanning laser ophthalmoscopy. *Invest. Ophthalmol. Vis. Sci.* 54, 7115–7124.
- Chui, T.Y., Song, H., Burns, S.A., 2008a. Adaptive-optics imaging of human cone photoreceptor distribution. *J. Opt. Soc. Am. A, Opt. Image Sci. Vision* 25, 3021–3029.
- Chui, T.Y., VanNasdale, D.A., Elsner, A.E., Burns, S.A., 2014a. The association between the foveal avascular zone and retinal thickness. *Invest. Ophthalmol. Vis. Sci.* 55, 6870–6877.
- Chui, T.Y.P., Dubow, M., Pinhas, A., Shah, N., Gan, A., Weitz, R., Sulai, Y.N., Dubra, A., Rosen, R.B., 2014b. Comparison of adaptive optics scanning light ophthalmoscopic fluorescein angiography and offset pinhole imaging. *Biomed. Optic Express* 5, 1173–1189.
- Chui, T.Y.P., Pinhas, A., Gan, A., Razeen, M., Shah, N., Cheang, E., Liu, C.L., Dubra, A., Rosen, R.B., 2016. Longitudinal imaging of microvascular remodeling in proliferative diabetic retinopathy using adaptive optics scanning light ophthalmoscopy. *Ophthalmic Physiol. Optic.* 36, 290–302.
- Chui, T.Y.P., Song, H., Burns, S.A., 2008b. Individual variations in human cone photoreceptor packing density: variations with refractive error. *Invest. Ophthalmol. Vis. Sci.* 49, 4679–4687.
- Chui, T.Y.P., Song, H.X., Burns, S.A., 2008c. Adaptive-optics imaging of human cone photoreceptor distribution. *J. Opt. Soc. Am. a-Opt. Image Sci. Vision* 25, 3021–3029.
- Chui, T.Y.P., Song, H.X., Clark, C.A., Papay, J.A., Burns, S.A., Elsner, A.E., 2012a. Cone photoreceptor packing density and the outer nuclear layer thickness in healthy subjects. *Invest. Ophthalmol. Vis. Sci.* 53, 3545–3553.
- Chui, T.Y.P., VanNasdale, D.A., Burns, S.A., 2012b. The use of forward scatter to improve retinal vascular imaging with an adaptive optics scanning laser ophthalmoscope. *Biomed. Optic Express* 3, 2537–2549.
- Chui, T.Y.P., Zhong, Z.Y., Burns, S.A., 2011. The relationship between peripapillary crescent and axial length: implications for differential eye growth. *Vis. Res.* 51, 2132–2138.
- Chui, T.Y.P., Zhong, Z.Y., Song, H.X., Burns, S.A., 2012c. Foveal avascular zone and its relationship to foveal pit shape. *Optom. Vis. Sci.* 89, 602–610.
- Collins, M., Davis, B., Wood, J., 1995. Microfluctuations of steady-state accommodation and the cardiopulmonary system. *Vis. Res.* 35, 2491–2502.
- Cooper, R.E., Wilk, M.A., Tarima, S., Carroll, J., 2016. Evaluating descriptive metrics of the human cone mosaic. *Invest. Ophthalmol. Vis. Sci.* 57, 2992–3001.
- Cooper, R.F., Tuten, W.S., Dubra, A., Brainard, D.H., Morgana, J.I.W., 2017. Non-invasive assessment of human cone photoreceptor function. *Biomed. Optic Express* 8, 5098–5112.
- Cope, W.T., Wolbarsht, M.L., Yamanashi, B.S., 1978. The corneal polarization cross. *J. Opt. Soc. Am.* 68, 1139–1141.
- Cunefare, D., Cooper, R.F., Higgins, B., Katz, D.F., Dubra, A., Carroll, J., Farsiou, S., 2016. Automatic detection of cone photoreceptors in split detector adaptive optics scanning light ophthalmoscope images. *Biomed. Optic Express* 7, 2036–2050.
- Cunefare, D., Fang, L.Y., Cooper, R.F., Dubra, A., Carroll, J., Farsiou, S., 2017. Open source software for automatic detection of cone photoreceptors in adaptive optics ophthalmoscopy using convolutional neural networks. *Sci. Rep.* 7, 6620.
- Curcio, C.A., Sloan, K.R., 1992. Packing geometry of human cone photoreceptors - variation with eccentricity and evidence for local anisotropy. *Vis. Neurosci.* 9, 169–180.
- Curcio, C.A., Sloan Jr., K.R., Packer, O., Hendrickson, A.E., Kalina, R.E., 1987. Distribution of cones in human and monkey retina: individual variability and radial asymmetry. *Science* 236, 579–582.
- Curcio, C.A., Sloan, K.R., Kalina, R.E., Hendrickson, A.E., 1990. Human photoreceptor topography. *J. Comp. Neurol.* 292, 497–523.
- Dalimier, E., Dainty, C., 2005. Comparative analysis of deformable mirrors for ocular adaptive optics. *Optic Express* 13, 4275–4285.
- de Boer, J.F., Milner, T.E., 2002. Review of polarization sensitive optical coherence tomography and Stokes vector determination. *J. Biomed. Optic.* 7, 359–371.
- de Castro, A., Huang, G., Sawides, L., Luo, T., Burns, S.A., 2016. Rapid high resolution imaging with a dual-channel scanning technique. *Opt. Lett.* 41, 1881–1884.
- de Castro, A., Sawides, L., Qi, X.F., Burns, S.A., 2017. Adaptive optics retinal imaging with automatic detection of the pupil and its boundary in real time using Shack-Hartmann images. *Appl. Optic.* 56, 6748–6754.
- De Clerck, E.E.B., Schouten, J., Berendschot, T., Kessels, A.G.H., Nuijts, R., Beckers, H.J.M., Schram, M.T., Stehouwer, C.D.A., Webers, C.A.B., 2015. New ophthalmologic imaging techniques for detection and monitoring of neurodegenerative changes in diabetes: a systematic review. *Lancet Diabetes & Endocrinology* 3, 653–663.
- Debarre, D., Booth, M.J., Wilson, T., 2007. Image based adaptive optics through optimisation of low spatial frequencies. *Optic Express* 15, 8176–8190.
- DeLint, P.J., Berendschot, T., van de Kraats, J., van Norren, D., 2000. Slow optical changes in human photoreceptors induced by light. *Invest. Ophthalmol. Vis. Sci.* 41,

- 282–289.
- Delori, F.C., 1988. Noninvasive technique for oximetry of blood in retinal-vessels. *Appl. Optic.* 27, 1113–1125.
- Delori, F.C., Goger, D.G., Keilhauer, C., Salvetti, P., Staurengi, G., 2006. Bimodal spatial distribution of macular pigment: evidence of a gender relationship. *J. Opt. Soc. Am. a-Opt. Image Sci. Vision* 23, 521–538.
- Delori, F.C., Pflibsen, K.P., 1989. Spectral reflectance of the human ocular fundus. *Appl. Optic.* 28, 1061–1077.
- Diaz-Santana, L., Torti, C., Munro, I., Gasson, P., Dainty, C., 2003. Benefit of higher closed-loop bandwidths in ocular adaptive optics. *Optic Express* 11, 2597–2605.
- Doble, N., Miller, D.T., Yoon, G., Williams, D.R., 2007. Requirements for discrete actuator and segmented wavefront correctors for aberration compensation in two large populations of human eyes. *Appl. Optic.* 46, 4501–4514.
- Doble, N., Williams, D.R., 2004. The application of MEMS technology for adaptive optics in vision science. *IEEE J. Sel. Top. Quant. Electron.* 10, 629–635.
- Doble, N., Yoon, G., Chen, L., Bierden, P., Singer, B., Olivier, S., Williams, D.R., 2002. Use of a microelectromechanical mirror for adaptive optics in the human eye. *Optic Lett.* 27, 1537–1539.
- Dong, Z.M., Wollstein, G., Wang, B., Schuman, J.S., 2017. Adaptive optics optical coherence tomography in glaucoma. *Prog. Retin. Eye Res.* 57, 76–88.
- Donnelly, W.J., Roorda, A., 2003. Optimal pupil size in the human eye for axial resolution. *J. Opt. Soc. Am. a-Opt. Image Sci. Vision* 20, 2010–2015.
- Dreher, A.W., Bille, J.F., Weinreb, R.N., 1989. Active optical depth resolution improvement of the laser tomographic scanner. *Appl. Optic.* 28, 804–808.
- Dreher, A.W., Reiter, K., 1992. Retinal laser ellipsometry - a new method for measuring the retinal nerve-fiber layer thickness distribution. *Clin. Vis. Sci.* 7, 481–488.
- Dreher, A.W., Reiter, K., Weinreb, R.N., 1992. Spatially resolved birefringence of the retinal nerve-fiber layer assessed with a retinal laser ellipsometer. *Appl. Optic.* 31, 3730–3735.
- Drexler, W., Fernandez, E.J., Hermann, B., Unterhuber, B., Sattmann, H., Prieto, P.M., Fercher, A.F., Artal, P., 2004. Adaptive optics ultrahigh resolution optical coherence tomography. *Invest. Ophthalmol. Vis. Sci.* 45 U929-U929.
- Du, Y., Veenstra, A., Palczewski, K., Kern, T.S., 2013. Photoreceptor cells are major contributors to diabetes-induced oxidative stress and local inflammation in the retina. *Proc. Natl. Acad. Sci. U.S.A.* 110, 16586–16591.
- Dubow, M., Pinhas, A., Shah, N., Cooper, R.F., Gan, A., Gentile, R.C., Hendrix, V., Sulai, Y.N., Carroll, J., Chui, T.Y.P., Walsh, J.B., Weitz, R., Dubra, A., Rosen, R.B., 2014. Classification of human retinal microaneurysms using adaptive optics scanning light ophthalmoscope fluorescein angiography. *Invest. Ophthalmol. Vis. Sci.* 55, 1299–1309.
- Dubra, A., Sulai, Y., Norris, J.L., Cooper, R.F., Dubis, A.M., Williams, D.R., Carroll, J., 2011. Noninvasive imaging of the human rod photoreceptor mosaic using a confocal adaptive optics scanning ophthalmoscope. *Biomed. Optic Express* 2, 1864–1876.
- Duncan, J.L., Zhang, Y., Gandhi, J., Nakanishi, C., Othman, M., Branham, K.E., Swaroop, A., Roorda, A., 2007. High-resolution imaging with adaptive optics in patients with inherited retinal degeneration. *Invest. Ophthalmol. Vis. Sci.* 48, 3283–3291.
- Dyshi, C., Wolf, S., Berezin, M.Y., Sauer, L., Hammer, M., Zinkernagel, M.S., 2017. Fluorescence lifetime imaging ophthalmoscopy. *Prog. Retin. Eye Res.* 60, 120–143.
- Elsner, A.E., Burns, S.A., Beausencourt, E., Weiter, J.J., 1998a. Foveal cone photopigment distribution: small alterations associated with macular pigment distribution. *Invest. Ophthalmol. Vis. Sci.* 39, 2394–2404.
- Elsner, A.E., Burns, S.A., Hughes, G.W., Webb, R.H., 1992a. Reflectometry with a scanning laser ophthalmoscope. *Appl. Optic.* 31, 3697–3710.
- Elsner, A.E., Burns, S.A., Lobes Jr., L.A., Doft, B.H., 1987. Cone photopigment abnormalities in diabetes. *IOVS (Investig. Ophthalmol. Vis. Sci.)* 718–724.
- Elsner, A.E., Burns, S.A., Webb, R.W., Hughes, G.W., 1992b. Reflectometry with a scanning laser ophthalmoscope. *Appl. Optic.* 31, 3697–3710.
- Elsner, A.E., Burns, S.A., Weiter, J.J., Delori, F.C., 1996. Infrared imaging of sub-retinal structures in the human ocular fundus. *Vis. Res.* 36, 191–205.
- Elsner, A.E., Chui, T.Y., Feng, L., Song, H.X., Papay, J.A., Burns, S.A., 2017. Distribution differences of macular cones measured by AOSLO: variation in slope from fovea to periphery more pronounced than differences in total cones. *Vis. Res.* 132, 62–68.
- Elsner, A.E., Dreher, A., Beausencourt, E., Burns, S., Zhou, Q., Webb, R.H., 1998b. Multiply scattered light tomography: vertical cavity surface emitting laser array used for imaging subretinal structures. *Laser Light Ophthalmol.* 8, 193–202.
- Elsner, A.E., King, B.J., 2015. Screening for macular disorders: the optometrist's perspective. *Clin. Optom.* 7, 15–38.
- Elsner, A.E., Miura, M., Burns, S.A., Beausencourt, E., Kunze, C., Kelley, L.M., Walker, J.P., Wing, G.L., Raskauskas, P.A., Fletcher, D.C., Zhou, Q., Dreher, A.W., 2000. Multiply scattered light tomography and confocal imaging: detecting neovascularization in age-related macular degeneration. *Optic Express* 7, 95–106.
- Elsner, A.E., Weber, A., Cheney, M.C., VanNasdale, D.A., Miura, M., 2007. Imaging polarimetry in patients with neovascular age-related macular degeneration. *J. Opt. Soc. Am. a-Opt. Image Sci. Vision* 24, 1468–1480.
- Elsner, A.E., Zhou, Q., Beck, F., Tornambe, P.E., Burns, S.A., Weiter, J.J., Dreher, A.W., 2001. Detecting AMD with multiply scattered light tomography. *Int. Ophthalmol.* 23, 245–250.
- Enzoly, A., Szabo, A., Kantor, O., David, C., Szalay, P., Szabo, K., Szel, A., Nemeth, J., Lukats, A., 2014. Pathologic alterations of the outer retina in streptozotocin-induced diabetes. *Invest. Ophthalmol. Vis. Sci.* 55, 3686–3699.
- Fahraeus, R., Lindqvist, T., 1931. The viscosity of the blood in narrow capillary tubes. *Am. J. Physiol.* 96, 562–568.
- Faulkner, D.J., Kemp, C.M., 1984. Human rhodopsin measurement using a T.V. based imaging fundus reflectometer. *Vis. Res.* 24, 221.
- Feeks, J.A., Hunter, J.J., 2017. Adaptive optics two-photon excited fluorescence lifetime imaging ophthalmoscopy of exogenous fluorophores in mice. *Biomed. Optic Express* 8, 2483–2495.
- Felberer, F., Kroisamer, J.S., Baumann, B., Zotter, S., Schmidt-Erfurth, U., Hitznerberger, C.K., Pircher, M., 2014. Adaptive optics SLO/OCT for 3D imaging of human photoreceptors in vivo. *Biomed. Optic Express* 5, 439–456.
- Fercher, A.F., Briers, J.D., 1981. Flow visualization by means of single-exposure speckle photography. *Optic Commun.* 37, 326–330.
- Fercher, A.F., Mengedocht, K., Werner, W., 1988. Eye-length measurement by interferometry with partially coherent light. *Opt. Lett.* 13, 186–188.
- Ferguson, R.D., Hammer, D.X., Elsner, A.E., Webb, R.H., Burns, S.A., 2004. Wide-field retinal hemodynamic imaging with the tracking scanning laser ophthalmoscope. *Optic Express* 12, 5198–5208.
- Ferguson, R.D., Zhong, Z., Hammer, D.X., Mujat, M., Patel, A.H., Deng, C., Zou, W., Burns, S.A., 2010. Adaptive optics scanning laser ophthalmoscope with integrated wide-field retinal imaging and tracking. *J. Opt. Soc. Am. A, Opt. Image Sci. Vision* 27, A265–A277.
- Fernandez, E.J., Iglesias, I., Antequera, N., Artal, P., 2001. Closed-loop adaptive optics in the human eye. *Invest. Ophthalmol. Vis. Sci.* 42, 544.
- Fernandez, E.J., Unterhuber, A., Povazay, B., Hermann, B., Artal, P., Drexler, W., 2006a. Chromatic aberration correction of the human eye for retinal imaging in the near infrared. *Optic Express* 14, 6213–6225.
- Fernandez, E.J., Vabre, L., Hermann, B., Unterhuber, A., Povazay, B., Drexler, W., 2006b. Adaptive optics with a magnetic deformable mirror: applications in the human eye. *Optic Express* 14, 8900–8917.
- Fienup, J.R., 1982. Phase retrieval algorithms - a comparison. *Appl. Optic.* 21, 2758–2769.
- Fu, X., Gens, J.S., Glazier, J.A., Burns, S.A., Gast, T.J., 2016. Progression of diabetic capillary occlusion: a model. *PLoS Comput. Biol.* 12, e1004932.
- Gabel, V.P., Nasemann, J., Birngruber, R., 1988. Fluorescein angiography with the laser-scanning ophthalmoscope. *Klinische Monatsblätter Fur Augenheilkunde* 193 438–438.
- Gast, T.J., Fu, X., Gens, J.S., Glazier, J.A., 2016. A computational model of peripheral photocoagulation for the prevention of progressive diabetic capillary occlusion. *J. Diabetes Res* 2016, 2508381.
- Godara, P., Dubis, A.M., Roorda, A., Duncan, J.L., Carroll, J., 2010. Adaptive optics retinal imaging: emerging clinical applications. *Optom. Vis. Sci.* 87, 930–941.
- Gomez-Vieyra, A., Dubra, A., Malacara-Hernandez, D., Williams, D.R., 2009. First-order design of off-axis reflective ophthalmic adaptive optics systems using afocal telescopes. *Optic Express* 17, 18906–18919.
- Gong, D., Zou, X., Zhang, X., Yu, W.H., Qu, Y., Dong, F.T., 2016. The influence of age and central foveal thickness on foveal zone size in healthy people. *Ophthalmic Surgery Lasers & Imaging Retina* 47, 142–148.
- Gonsalves, R.A., 1982. Phase retrieval and diversity in adaptive optics. *Opt. Eng.* 21, 829–832.
- Gonsalves, R.A., 1983. Fundamentals of wavefront sensing by phase retrieval. *Proc. Soc. Photo Opt. Instrum. Eng.* 351, 56–65.
- Gorrand, J.-M., Delori, F.C., 1995. A reflectometric technique for assessing photoreceptor alignment. *Vis. Res.* 35, 999–1010.
- Gorrand, J.M., Delori, F.C., 1999. Reflectance and curvature of the inner limiting membrane at the foveola. *J. Opt. Soc. Am. A, Opt. Image Sci. Vision* 16, 1229–1237.
- Gray, D.C., Merigan, W., Wolfig, J.L., Gee, B.P., Porter, J., Dubra, A., Twietmeyer, T.H., Ahmad, K., Tumber, R., Reinholz, F., Williams, D.R., 2006. In vivo fluorescence imaging of primate retinal ganglion cells and retinal pigment epithelial cells. *Optic Express* 14, 7144–7158.
- Grieve, K., Roorda, A., 2008. Intrinsic signals from human cone photoreceptors. *Invest. Ophthalmol. Vis. Sci.* 49, 713–719.
- Grieve, K., Tiruveedhula, P., Zhang, Y.H., Roorda, A., 2006. Multi-wavelength imaging with the adaptive optics scanning laser ophthalmoscope. *Optic Express* 14, 12230–12242.
- Gruppetta, S., Lacombe, F., Puget, P., 2005. Study of the dynamic aberrations of the human tear film. *Optic Express* 13, 7631–7636.
- Gu, B.Y., Wang, X.L., Twa, M.D., Tam, J., Girkin, C.A., Zhang, Y.H., 2018. Noninvasive in vivo characterization of erythrocyte motion in human retinal capillaries using high-speed adaptive optics near-confocal imaging. *Biomed. Optic Express* 9.
- Hammer, D.X., Ferguson, R.D., Bigelow, C.E., Ifitimia, N.V., Ustun, T.E., Burns, S.A., 2006. Adaptive optics scanning laser ophthalmoscope for stabilized retinal imaging. *Optic Express* 14, 3354–3367.
- Hammer, D.X., Ferguson, R.D., Magill, J.C., Elsner, A.F., Webb, R.H., 2002. Tracking scanning laser ophthalmoscope (TSLO): initial human subject testing. *Invest. Ophthalmol. Vis. Sci.* 43 U1260-U1260.
- Hammer, D.X., Ferguson, R.D., Magill, J.C., White, M.A., Elsner, A.E., Webb, R.H., 2003. Compact scanning laser ophthalmoscope with high-speed retinal tracker. *Appl. Optic.* 42, 4621–4632.
- Hampson, K.M., Mallen, E.A.H., 2012. Chaos in ocular aberration dynamics of the human eye. *Biomed. Optic Express* 3, 863–877.
- Harmening, W.M., Tuten, W.S., Roorda, A., Sincich, L.C., 2014. Mapping the perceptual grain of the human retina. *J. Neurosci.* 34, 5667–5677.
- Helmholtz, H.v., 1866. *Treatise on Physiological Optics*, second ed. Dover, New York.
- Hendrickson, A.E., Yuodelis, C., 1984. The morphological development of the human fovea. *Ophthalmology* 91, 603–612.
- Hermann, B., Fernandez, E.J., Unterhuber, A., Sattmann, H., Fercher, A.F., Drexler, W., Prieto, P.M., Artal, P., 2004. Adaptive-optics ultrahigh-resolution optical coherence tomography. *Optic Lett.* 29, 2142–2144.
- Hillard, J.G., Gast, T.J., Chui, T.Y., Sapir, D., Burns, S.A., 2016. Retinal arterioles in hypo-, normo-, and hypertensive subjects measured using adaptive optics. *Trans. Vis. Sci. Technol.* 5, 16.
- Hillmann, D., Spahr, H., Pfaffle, C., Sudkamp, H., Franke, G., Huttmann, G., 2016. In vivo

- optical imaging of physiological responses to photostimulation in human photoreceptors. *Proc. Natl. Acad. Sci. U.S.A.* 113, 13138–13143.
- Hofer, H., Artal, P., Singer, B., Aragon, J.L., Williams, D.R., 2001. Dynamics of the eye's wave aberration. *J. Opt. Soc. Am. a-Opt. Image Sci. Vision* 18, 497–506.
- Hofer, H., Carroll, J., Neitz, J., Neitz, M., Williams, D.R., 2005. Organization of the human trichromatic cone mosaic. *J. Neurosci.* 25, 9669–9679.
- Hofer, H., Sredar, N., Queener, H., Li, C.H., Porter, J., 2011. Wavefront sensorless adaptive optics ophthalmoscopy in the human eye. *Optic Express* 19, 14160–14171.
- Hood, D.C., Lee, D., Jarukasetphon, R., Nunez, J., Mavrommatis, M.A., Rosen, R.B., Ritch, R., Dubra, A., Chui, T.Y.P., 2017. Progression of local glaucomatous damage near fixation as seen with adaptive optics imaging. *Translational vision science & technology* 6, 6.
- Howarth, P.A., Bradley, A., 1986. The longitudinal chromatic aberration of the human eye, and its correction. *Vis. Res.* 26, 361–366.
- Howland, H.C., Howland, B., 1977. A subjective method for the measurement of monochromatic aberrations of the eye. *J. Opt. Soc. Am.* 67, 1508–1518.
- Huang, G., Gast, T.J., Burns, S.A., 2014. In vivo adaptive optics imaging of the temporal raphe and its relationship to the optic disc and fovea in the human retina. *Invest. Ophthalmol. Vis. Sci.* 55, 5952–5961.
- Huang, G., Luo, T., Gast, T.J., Burns, S.A., Malinovsky, V.E., Swanson, W.H., 2015. Imaging glaucomatous damage across the temporal raphe. *Invest. Ophthalmol. Vis. Sci.* 56, 3496–3504.
- Huang, G., Qi, X., Chui, T.Y., Zhong, Z., Burns, S.A., 2012. A clinical planning module for adaptive optics SLO imaging. *Optom. Vis. Sci.: official publication of the American Academy of Optometry* 89, 593–601.
- Hunter, J.J., Masella, B., Dubra, A., Sharma, R., Yin, L., Merigan, W.H., Palczewska, G., Palczewski, K., Williams, D.R., 2011. Images of photoreceptors in living primate eyes using adaptive optics two-photon ophthalmoscopy. *Biomed. Optic Express* 2, 139–148.
- Iglesias, I., Artal, P., 2000. High-resolution retinal images obtained by deconvolution from wave-front sensing. *Optic Lett.* 25, 1804–1806.
- Iglesias, I., Ragazzoni, R., Julien, Y., Artal, P., 2002. Extended source pyramid wave-front sensor for the human eye. *Optic Express* 10, 419–428.
- Ikram, M.K., Cheung, C.Y., Lorenzi, M., Klein, R., Jones, T.L.Z., Wong, T.Y., Retinal, N.J.W., 2013. Retinal vascular caliber as a biomarker for diabetes microvascular complications. *Diabetes Care* 36, 750–759.
- Ivanoff, A., 1946. Sur une methode de mesure des aberrations chromatique et spheriques de l'oeil en lumiere dirigee. *Comptes rendus de l'Academie de Sciences* 231 562–528.
- Ivanoff, A., 1947. On the influence of accommodation on spherical aberration in the human eye, an attempt to interpret night myopia. *J. Opt. Soc. Am.* 37, 730–731.
- Izzard, A.S., Bund, S.J., Heagerty, A.M., 1996. Increased wall-lumen ratio of mesenteric vessels from the spontaneously hypertensive rat is not associated with increased contractility under isobaric conditions. *Hypertension* 28, 604–608.
- Jacob, J., Paques, M., Krivosic, V., Dupas, B., Erginay, A., Tadayoni, R., Gaudric, A., 2017. Comparing parafoveal cone photoreceptor mosaic metrics in younger and older age groups using an adaptive optics retinal camera. *Ophthalmic Surgery Lasers & Imaging Retina* 48, 45–50.
- Jian, Y.F., Lee, S., Ju, M.J., Heisler, M., Ding, W.G., Zawadzki, R.J., Bonora, S., Sarunic, M.V., 2016. Lens-based wavefront sensorless adaptive optics swept source OCT. *Sci. Rep.* 6, 27620.
- Jian, Y.F., Xu, J., Gadowski, M.A., Bonora, S., Zawadzki, R.J., Sarunic, M.V., 2014. Wavefront sensorless adaptive optics optical coherence tomography for in vivo retinal imaging in mice. *Biomed. Optic Express* 5, 547–559.
- Jonas, J.B., Wang, Y.X., Zhang, Q., Liu, Y., Xu, L., Wei, W.B., 2015. Macular bruch's membrane length and axial length. The Beijing eye study. *PLoS One* 10.
- Jones, B.W., Pfeiffer, R.L., Ferrell, W.D., Watt, C.B., Tucker, J., Marc, R.E., 2016. Retinal remodeling and metabolic alterations in human AMD. *Front. Cell. Neurosci.* 10.
- Jonnal, R.S., Kocaoglu, O.P., Wang, Q., Lee, S., Miller, D.T., 2012. Phase-sensitive imaging of the outer retina using optical coherence tomography and adaptive optics. *Biomed. Optic Express* 3, 104–124.
- Jonnal, R.S., Kocaoglu, O.P., Zawadzki, R.J., Liu, Z.L., Miller, D.T., Werner, J.S., 2016. A review of adaptive optics optical coherence tomography: technical advances, scientific applications, and the future. *Invest. Ophthalmol. Vis. Sci.* 57, OCT51–OCT68.
- Jonnal, R.S., Rha, J., Zhang, Y., Cense, B., Gao, W.H., Miller, D.T., 2007. In vivo functional imaging of human cone photoreceptors. *Optic Express* 15, 16141–16160.
- Ju, M.J., Heisler, M., Wahl, D., Jian, Y.F., Sarunic, M.V., 2017. Multiscale sensorless adaptive optics OCT angiography system for in vivo human retinal imaging. *J. Biomed. Optic.* 22, 1–10.
- Jung, F., Kiesewetter, H., Koerber, N., Wolf, S., Reim, M., Mueller, G., 1983. Quantification of characteristic blood flow parameters in the vessels of the retina with a picture analysis system for video fluorescence angiograms initial findings. *Graefes Arch. Clin. Exp. Ophthalmol.* 221, 133–136.
- Kashani, A.H., Chen, C.L., Gahm, J.K., Zheng, F., Richter, G.M., Rosenfeld, P.J., Shi, Y.G., Wang, R.K.K., 2017. Optical coherence tomography angiography: a comprehensive review of current methods and clinical applications. *Prog. Retin. Eye Res.* 60, 66–100.
- Kelly, J.E., Mihashi, T., Howland, H.C., 2004. Compensation of corneal horizontal/vertical astigmatism, lateral coma, and spherical aberration by internal optics of the eye. *J. Vis.* 4, 262–271.
- Kern, T.S., Berkowitz, B.A., 2015. Photoreceptors in diabetic retinopathy. *Journal of Diabetes Investigation* 6, 371–380.
- Kern, T.S., Engerman, R.L., 1995. Vascular-lesions in diabetes are distributed non-uniformly within the retina. *Exp. Eye Res.* 60, 545–549.
- Keunen, J.E.E., Norren, D.v., Meel, G.J.v., 1987. Density of foveal cone pigments at older age. *Invest. Ophthalmol. Vis. Sci.* 28, 985–991.
- Kilbride, P.E., Read, J.S., Fishman, G.A., Fishman, M., 1983. Determination of human cone pigment density difference spectra in spatially resolved regions of the fovea. *Vis. Res.* 23, 1341–1350.
- King, B.J., Sapoznik, K.A., Elsner, A.E., Gast, T.J., Papay, J.A., Clark, C.A., Burns, S.A., 2017. SD-OCT and adaptive optics imaging of outer retinal tubulation. *Optom. Vis. Sci.* 94, 411–420.
- Kirber, W.M., Nichols, C.W., Grimes, P.A., Winegrad, A.I., Laties, A.M., 1980. A permeability defect of the retinal-pigment epithelium - occurrence in early streptozocin diabetes. *Arch. Ophthalmol.* 98, 725–728.
- Klein, R., Klein, B.E.K., Moss, S.E., Wong, T.Y., Hubbard, L., Cruickshanks, K.J., Palta, M., 2004. The relation of retinal vessel caliber to the incidence and progression of diabetic retinopathy - XIX: the Wisconsin epidemiologic study of diabetic retinopathy. *Arch. Ophthalmol.* 122, 76–83.
- Klein, R., Knudtson, M.D., Klein, B.E.K., Zinman, B., Gardiner, R., Suissa, S., Sinaiko, A.R., Donnelly, S.M., Goodyer, P., Strand, T., Maurer, M., 2010. The relationship of retinal vessel diameter to changes in diabetic nephropathy structural variables in patients with type 1 diabetes. *Diabetologia* 53, 1638–1646.
- Knighton, R.W., Huang, X., Zhou, Q., 1998. Microtubule contribution to the reflectance of the retinal nerve fiber layer. *Invest. Ophthalmol. Vis. Sci.* 39, 189–193.
- Kocaoglu, O.P., Cense, B., Jonnal, R.S., Wang, Q., Lee, S.Y., Gao, W.H., Miller, D.T., 2011. Imaging retinal nerve fiber bundles using optical coherence tomography with adaptive optics. *Vis. Res.* 51, 1835–1844.
- Kocaoglu, O.P., Ferguson, R.D., Jonnal, R.S., Liu, Z.L., Wang, Q., Hammer, D.X., Miller, D.T., 2014. Adaptive optics optical coherence tomography with dynamic retinal tracking. *Biomed. Optic Express* 5, 2262–2284.
- Kocaoglu, O.P., Liu, Z.L., Zhang, F.R., Kurokawa, K., Jonnal, R.S., Miller, D.T., 2016. Photoreceptor disc shedding in the living human eye. *Biomed. Optic Express* 7, 4554–4568.
- Koch, E., Rosenbaum, D., Brolly, A., Sahel, J.A., Chaumet-Riffaud, P., Girerd, X., Rossant, F., Paques, M., 2014. Morphometric analysis of small arteries in the human retina using adaptive optics imaging: relationship with blood pressure and focal vascular changes. *J. Hypertens.* 32, 890–898.
- Koester, C.J., 1980. Scanning mirror microscope with optical sectioning characteristics - applications in ophthalmology. *Appl. Optic.* 19, 1749–1757.
- Krauskopf, J., 1965. Some experiments with a photoelectric ophthalmoscope. *Excerpta Med. Int. Congr. Ser.* 125, 171–181.
- Kumar, A., Drexler, W., Leitgeb, R.A., 2013. Subaperture correlation based digital adaptive optics for full field optical coherence tomography. *Optic Express* 21, 10850–10866.
- Kumar, A., Kamali, T., Platzer, R., Unterhuber, A., Drexler, W., Leitgeb, R.A., 2015. Anisotropic aberration correction using region of interest based digital adaptive optics in Fourier domain OCT. *Biomed. Optic Express* 6, 1124–1134.
- Kurokawa, K., Sasaki, K., Makita, S., Yamanari, M., Cense, B., Yasuno, Y., 2010. Simultaneous high-resolution retinal imaging and high-penetration choroidal imaging by one-micrometer adaptive optics optical coherence tomography. *Optic Express* 18, 8515–8527.
- Laatikainen, L., Larinkari, J., 1977. Capillary-free area of fovea with advancing age. *Invest. Ophthalmol. Vis. Sci.* 16, 1154–1156.
- Lammer, J., Prager, S.G., Cheney, M.C., Ahmed, A., Radwan, S.H., Burns, S.A., Silva, P.S., Sun, J.K., 2016. Cone photoreceptor irregularity on adaptive optics scanning laser ophthalmoscopy correlates with severity of diabetic retinopathy and macular edema. *Invest. Ophthalmol. Vis. Sci.* 57, 6624–6632.
- Land, M.E., Cooper, R.F., Young, J., Berg, E., Kitchner, T., Xiang, Q., Szabo, A., Ivacic, L.C., Stepien, K.E., Page, C.D., Carroll, J., Connor, T., Brilliant, M., 2014. Cone structure in subjects with known genetic relative risk for AMD. *Optom. Vis. Sci.* 91, 939–949.
- Langlo, C.S., Patterson, E.J., Higgins, B.P., Summerfelt, P., Razeen, M.M., Erker, L.R., Parker, M., Collison, F.T., Fishman, G.A., Kay, C.N., Zhang, J., Weleber, R.G., Yang, P., Wilson, D.J., Pennesi, M.E., Lam, B.L., Chiang, J., Chulay, J.D., Dubra, A., Hauswirth, W.W., Carroll, J., Grp, A.-S., 2016. Residual foveal cone structure in CNGB3-associated achromatopsia. *Invest. Ophthalmol. Vis. Sci.* 57, 3984–3995.
- Le Gargasson, J.F., Glanc, M., Lena, P., 2001. Retinal imaging with adaptive optics. *Comptes Rendus De L Academie Des Sciences Serie Iv Physique Astrophysique* 2, 1131–1138.
- Legras, R., Gaudric, A., Woog, K., 2018. Distribution of cone density, spacing and arrangement in adult healthy retinas with adaptive optics flood illumination. *PLoS One* 13, e0191141.
- Leitgeb, R.A., Schmetterer, L., Drexler, W., Fercher, A.F., Zawadzki, R.J., Bajraszewski, T., 2003. Real-time assessment of retinal blood flow with ultrafast acquisition by color Doppler Fourier domain optical coherence tomography. *Optic Express* 11, 3116–3121.
- Leitgeb, R.A., Werkmeister, R.M., Blatter, C., Schmetterer, L., 2014. Doppler optical coherence tomography. *Prog. Retin. Eye Res.* 41, 26–43.
- Lerne, N., Rossant, F., Bloch, I., Paques, M., Koch, E., IEEE, 2014. Segmentation of retinal arteries in adaptive optics images. In: 2014 22nd International Conference on Pattern Recognition, pp. 574–579.
- Lewis, A.L., M, K., C, O., 1982. A modified achromatizing lens. *Am. J. Optom.* 59, 909–911.
- Li, C.H., Sredar, N., Ivers, K.M., Queener, H., Porter, J., 2010a. A correction algorithm to simultaneously control dual deformable mirrors in a woofer-tweeter adaptive optics system. *Optic Express* 18, 16671–16684.
- Li, K.Y., Roorda, A., 2007. Automated identification of cone photoreceptors in adaptive optics retinal images. *J. Opt. Soc. Am. A, Opt. Image Sci. Vision* 24, 1358–1363.
- Li, K.Y., Tiruveedhula, P., Roorda, A., 2010b. Intersubject variability of foveal cone photoreceptor density in relation to eye length. *Invest. Ophthalmol. Vis. Sci.* 51, 6858–6867.
- Liang, J., Grimm, B., Goetz, S., Bille, J.F., 1994. Objective measurements of wave aberrations of the human eye with the use of a Hartmann-Shack wave-front sensor. *J. Opt.*

- Soc. Am. A 11, 1949–1957.
- Liang, J., Williams, D.R., Miller, D.T., 1997. Supernormal vision and high-resolution retinal imaging through adaptive optics. *J. Opt. Soc. Am. A* 14, 2884–2892.
- Lieth, E., Gardner, T.W., Barber, A.J., Antonetti, D.A., Penn State Retina Res. G., 2000. Retinal neurodegeneration: early pathology in diabetes. *Clin. Exp. Ophthalmol.* 28, 3–8.
- Lin, A.D., Lee, A.Y., Zhang, Q., Rezaei, K.A., Kinyoun, J., Wang, R.K., Lee, C.S., 2016. Association between OCT-based microangiography perfusion indices and diabetic retinopathy severity. *Br. J. Ophthalmol.* <https://doi.org/10.1136/bjophthalmol-2016-309514>.
- Liu, J.F., Jung, H., Dubra, A., Tam, J., 2017a. Automated photoreceptor cell identification on nonconfocal adaptive optics images using multiscale circular voting. *Invest. Ophthalmol. Vis. Sci.* 58, 4477–4489.
- Liu, Y.Z., South, F.A., Xu, Y., Carney, P.S., Boppart, S.A., 2017b. Computational optical coherence tomography invited. *Biomed. Optic Express* 8, 1549–1574.
- Liu, Z.L., Kocaoglu, O.P., Miller, D.T., 2016. 3D imaging of retinal pigment epithelial cells in the living human retina. *Invest. Ophthalmol. Vis. Sci.* 57, OCT533–OCT543.
- Liu, Z.L., Kurokawa, K., Zhang, F.R., Lee, J.J., Miller, D.T., 2017c. Imaging and quantifying ganglion cells and other transparent neurons in the living human retina. *Proc. Natl. Acad. Sci. U.S.A.* 114, 12803–12808.
- Logean, E., Schmetterer, L., Riva, C.E., 2003. Velocity profile of red blood cells in human retinal vessels by confocal scanning laser Doppler velocimetry (vol 13, pg 45, 2003). *Laser Phys.* 13 804–804.
- Lombardo, M., Lombardo, G., 2009. New methods and techniques for sensing the wave aberrations of human eyes. *Clin. Exp. Optom.* 92, 176–186.
- Lombardo, M., Lombardo, G., Lomoriello, D.S., Ducoi, P., Stirpe, M., Serrao, S., 2013a. Interocular symmetry of parafoveal photoreceptor cone density distribution. *Retina: The Journal of Retinal and Vitreous Diseases* 33, 1640–1649.
- Lombardo, M., Parravano, M., Lombardo, G., Varano, M., Boccassini, B., Stirpe, M., Serrao, S., 2014a. Adaptive optics imaging of parafoveal cones in type 1 diabetes. *Retina: The Journal of Retinal and Vitreous Diseases* 34, 546–557.
- Lombardo, M., Serrao, S., Devaney, N., Parravano, M., Lombardo, G., 2013b. Adaptive optics technology for high-resolution retinal imaging. *Sensors* 13, 334–366.
- Lombardo, M., Serrao, S., Ducoi, P., Lombardo, G., 2013c. Eccentricity dependent changes of density, spacing and packing arrangement of parafoveal cones. *Ophthalmic Physiol. Optic.* 33, 516–526.
- Lombardo, M., Serrao, S., Lombardo, G., 2014b. Technical factors influencing cone packing density estimates in adaptive optics fundus illuminated retinal images. *PLoS One* 9, e107402.
- Lorenzi, M., Gerhardinger, C., 2001. Early cellular and molecular changes induced by diabetes in the retina. *Diabetologia* 44, 791–804.
- Lu, J., Gu, B.Y., Wang, X.L., Zhang, Y.H., 2016a. Adaptive optics parallel near-confocal scanning ophthalmoscopy. *Optic Lett.* 41, 3852–3855.
- Lu, Y., Bernabeu, M.O., Lammer, J., Cai, C.C., Jones, M.L., Franco, C.A., Aiello, L.P., Sun, J.K., 2016b. Computational fluid dynamics assisted characterization of parafoveal hemodynamics in normal and diabetic eyes using adaptive optics scanning laser ophthalmoscopy. *Biomed. Optic Express* 7, 4958–4973.
- Luo, T., Gast, T.J., Vermeer, T.J., Burns, S.A., 2017. Retinal vascular branching in healthy and diabetic subjects. *Invest. Ophthalmol. Vis. Sci.* 58, 2685–2694.
- Mainster, M.A., Timberlake, G.T., Webb, R.H., Hughes, G.W., 1982. Scanning laser ophthalmoscopy - clinical-applications. *Ophthalmology* 89, 852–857.
- Makita, S., Hong, Y., Yamanari, M., Yatagai, T., Yasuno, Y., 2006. Optical coherence angiography. *Optic Express* 14, 7821–7840.
- Makous, W., Carroll, J., Wolfing, J.I., Lin, J., Christie, N., Williams, D.R., 2006. Retinal microscotomas revealed with adaptive-optics microflashes. *Invest. Ophthalmol. Vis. Sci.* 47, 4160–4167.
- Marcos, S., Burns, S.A., He, J.C., 1998. Model for cone directionality reflectometric measurements based on scattering. *J. Opt. Soc. Am. a-Opt. Image Sci. Vision* 15, 2012–2022.
- Marcos, S., Burns, S.A., Prieto, P.M., Navarro, R., Baraibar, B., 2001. Investigating sources of variability of monochromatic and transverse chromatic aberrations across eyes. *Vis. Res.* 41, 3861–3871.
- Marcos, S., Navarro, R., Artal, P., 1996. Coherent imaging of the cone mosaic in the living human eye. *J. Opt. Soc. Am. A* 13, 897–905.
- Marcos, S., Tornow, R.P., Elsner, A.E., Navarro, R., 1997. Foveal cone spacing and cone photopigment density difference: objective measurements in the same subjects. *Vis. Res.* 37, 1909–1915.
- Marcos, S., Werner, J.S., Burns, S.A., Merigan, W.H., Artal, P., Atchison, D.A., Hampson, K.M., Legras, R., Lundstrom, L., Yoon, G., Carroll, J., Choi, S.S., Doble, N., Dubis, A.M., Dubra, A., Elsner, A., Jonnal, R., Miller, D.T., Paques, M., Smithson, H.E., Young, L.K., Zhang, Y., Campbell, M., Hunter, J., Metha, A., Palczewska, G., Schallek, J., Sincich, L.C., 2017. Vision science and adaptive optics, the state of the field. *Vis. Res.* 132, 3–33.
- Marsh, P.N., Burns, D., Girkin, J.M., 2003. Practical implementation of adaptive optics in multiphoton microscopy. *Optic Express* 11, 1123–1130.
- Martin, J.A., Roorda, A., 2005. Direct and noninvasive assessment of parafoveal capillary leukocyte velocity. *Ophthalmology* 112, 2219–2224.
- Martin, J.A., Roorda, A., 2009. Pulsatility of parafoveal capillary leukocytes. *Exp. Eye Res.* 88, 356–360.
- Masella, B.D., Hunter, J.J., Williams, D.R., 2014. New wrinkles in retinal densitometry. *Invest. Ophthalmol. Vis. Sci.* 55, 7525–7534.
- McLeod, D.S., Luty, G.A., 1994. High-resolution histologic analysis of the human choroidal vasculature. *Invest. Ophthalmol. Vis. Sci.* 35, 3799–3811.
- Meixner, E., Michelson, G., 2015. Measurement of retinal wall-to-lumen ratio by adaptive optics retinal camera: a clinical research. *Graefes Arch. Clin. Exp. Ophthalmol.* 253, 1985–1995.
- Mellem-Kairala, M.B., Elsner, A.E., Weber, A., Simmons, R.B., Burns, S.A., 2005. Improved contrast of peripapillary hyperpigmentation using polarization analysis. *Invest. Ophthalmol. Vis. Sci.* 46, 1099–1106.
- Menghini, M., Lujan, B.J., Zayit-Soudry, S., Syed, R., Porco, T.C., Bayabo, K., Carroll, J., Roorda, A., Duncan, J.L., 2015. Correlation of outer nuclear layer thickness with cone density values in patients with retinitis pigmentosa and healthy subjects. *Invest. Ophthalmol. Vis. Sci.* 56, 372–381.
- Merino, D., Duncan, J.L., Tiruveedhula, P., Roorda, A., 2011. Observation of cone and rod photoreceptors in normal subjects and patients using a new generation adaptive optics scanning laser ophthalmoscope. *Biomed. Optic Express* 2, 2189–2201.
- Michelson, G., Schmauss, B., 1995. Two dimensional mapping of the perfusion of the retina and optic nerve head. *Br. J. Ophthalmol.* 79, 1126–1132.
- Michelson, G., Schmauss, B., Langhans, M.J., Harazny, J., Groh, M.J.M., 1996. Principle, validity, and reliability of scanning laser Doppler flowmetry. *J. Glaucoma* 5, 99–105.
- Michelson, G., Warntges, S., Baleanu, D., Welzenbach, J., Ohno-Jinno, A., Pogorelov, P., Harazny, J., 2007. Morphometric age-related evaluation of small retinal vessels by scanning laser Doppler flowmetry - determination of a vessel wall index. *Retina-the Journal of Retinal and Vitreous Diseases* 27, 490–498.
- Miller, D.T., Thibos, L.N., Hong, X., 2005. Requirements for segmented correctors for diffraction-limited performance in the human eye. *Optic Express* 13, 275–289.
- Miller, D.T., Williams, D.R., Morris, G.M., Liang, J., 1996. Images of cone photoreceptors in the living human eye. *Vis. Res.* 36, 1067–1079.
- Miura, M., Makita, S., Sugiyama, S., Hong, Y.J., Yasuno, Y., Elsner, A.E., Tamiya, S., Tsukahara, R., Iwasaki, T., Goto, H., 2017. Evaluation of intraretinal migration of retinal pigment epithelial cells in age-related macular degeneration using polarimetric imaging. *Sci. Rep.* 7.
- Miyagawa, S., Fukuyama, H., Hirota, M., Yamaguchi, T., Kitamura, K., Endo, T., Kanda, H., Morimoto, T., Fujikado, T., 2017. Automated measurements of human cone photoreceptor density in healthy and degenerative retina by region-based segmentation. *Clin. Ophthalmol.* 11, 781–790.
- Mizutani, M., Kern, T.S., Lorenzi, M., 1996. Accelerated death of retinal microvascular cells in human and experimental diabetic retinopathy. *J. Clin. Invest.* 97, 2883–2890.
- Moran, E.P., Wang, Z.X., Chen, J., Sapieha, P., Smith, L.E.H., Ma, J.X., 2016. Neurovascular cross talk in diabetic retinopathy: pathophysiological roles and therapeutic implications. *Am. J. Physiol. Heart Circ. Physiol.* 311, H738–H749.
- Morgan, J.I., Hunter, J.J., Masella, B., Wolfe, R., Gray, D.C., Merigan, W.H., Delori, F.C., Williams, D.R., 2008. Light-induced retinal changes observed with high-resolution autofluorescence imaging of the retinal pigment epithelium. *Invest. Ophthalmol. Vis. Sci.* 49, 3715–3729.
- Morgan, J.I.W., 2016. The fundus photo has met its match: optical coherence tomography and adaptive optics ophthalmoscopy are here to stay. *Ophthalmic Physiol. Optic.* 36, 218–239.
- Morgan, J.I.W., Dubra, A., Wolfe, R., Merigan, W.H., Williams, D.R., 2009. In vivo autofluorescence imaging of the human and macaque retinal pigment epithelial cell mosaic. *Invest. Ophthalmol. Vis. Sci.* 50, 1350–1359.
- Morgan, J.I.W., Han, G., Klinman, E., Maguire, W.M., Chung, D.C., Maguire, A.M., Bennett, J., 2014. High-resolution adaptive optics retinal imaging of cellular structure in choroideremia. *Invest. Ophthalmol. Vis. Sci.* 55, 6381–6397.
- Morgan, W.H., Hazelton, M.L., Yu, D.Y., 2016. Retinal venous pulsation: expanding our understanding and use of this enigmatic phenomenon. *Prog. Retin. Eye Res.* 55, 82–107.
- Mujat, M., Ferguson, R.D., Iftimia, N., Hammer, D.X., 2009. Compact adaptive optics line scanning ophthalmoscope. *Optic Express* 17, 10242–10258.
- Muller, M.S., Elsner, A.E., 2018. Confocal Retinal Imaging Using a Digital Light Projector with a Near Infrared VCSEL Source. *SPIE OPTO. SPIE*, pp. 9.
- Muller, M.S., Elsner, A.E., Ozawa, G.Y., 2013. Non-Mydriatic confocal retinal imaging using a digital light projector. In: Manns, F., Soderberg, P.G., Ho, A. (Eds.), *Ophthalmic Technologies Xxiii*.
- Muller, M.S., Green, J.J., Baskaran, K., Ingling, A.W., Clendenon, J.L., Gast, T.J., Elsner, A.E., 2015. Non-mydratric confocal retinal imaging using a digital light projector. In: *Emerging Digital Micromirror Device Based Systems and Applications Vii 9376*.
- Murakami, T., Yoshimura, N., 2013. Structural changes in individual retinal layers in diabetic macular edema. *J. Diab. Res.* <https://doi.org/10.1155/2013/920713>.
- Muramatsu, M., Eiju, T., Shirai, T., Matsuda, K., 1997. Application of a liquid crystal spatial light modulator on optical roughness measurements by a speckle correlation method using two refractive indices. *Optic Laser. Technol.* 29, 271–273.
- Murray, C.D., 1926a. The physiological principle of minimum work applied to the angle of branching of arteries. *J. Gen. Physiol.* 9, 835–841.
- Murray, C.D., 1926b. The physiological principle of minimum work I The vascular system and the cost of blood volume. *Proc. Natl. Acad. Sci. U.S.A.* 12, 207–214.
- Nelson, D.A., Krupsky, S., Pollack, A., Aloni, E., Belkin, M., Vanzetta, I., Rosner, M., Grinvald, A., 2005. Special report: noninvasive multi-parameter functional optical imaging of the eye. *Ophthalmic Surg. Laser. Imag.* 36, 57–66.
- Nesper, P.L., Scarinci, F., Fawzi, A.A., 2017. Adaptive optics reveals photoreceptor abnormalities in diabetic macular ischemia. *PLoS One* 12, e0169926.
- Nirmaier, T., Pudasaini, G., Bille, J., 2003. Very fast wave-front measurements at the human eye with a custom CMOS-based Hartmann-Shack sensor. *Optic Express* 11, 2704–2716.
- Norren, D., van der Kraats, J., 1981. A continuously recording retinal densitometer. *Vis. Res.* 21, 897–905.
- Norren, D.V., van der Kraats, J., 1989. Imaging retinal densitometry with a confocal scanning laser ophthalmoscope. *Vis. Res.* 29, 1825–1830.
- Novotny, H.R., Alvis, D.L., 1961. A method of photographing fluorescence in circulating blood in human retina. *Circulation* 24, 82.
- Obata, R., Yanagi, Y., 2014. Quantitative analysis of cone photoreceptor distribution and its relationship with axial length, age, and early age-related macular degeneration.

- PLoS One 9, e91873.
- Ong, Y.T., Wong, T.Y., Klein, R., Klein, B.E.K., Mitchell, P., Sharrett, A.R., Couper, D.J., Ikram, M.K., 2013. Hypertensive retinopathy and risk of stroke. *Hypertension* 62, 706–711.
- Pallikaris, A., Williams, D.K., Hofer, H., 2003. The reflectance of single cones in the living human eye. *Invest. Ophthalmol. Vis. Sci.* 44, 4580–4592.
- PandaJonas, S., Jonas, J.B., JakobczykZmija, M., 1995. Retinal photoreceptor density decreases with age. *Ophthalmology* 102, 1853–1859.
- Paques, M., Meimon, S., Grieve, K., Rossant, F., 2017. Adaptive optics for in-vivo exploration of human retinal structures. In: Ferraro, P., Grilli, S., RitschMarte, M., Hitznerberger, C.K. (Eds.), *SPIE Optical Metrology*. SPIE, pp. 8.
- Pepperberg, D.R., Kahlert, M., Krause, A., Hofmann, K.P., 1988. Photic modulation of a highly sensitive, near-infrared light-scattering signal recorded from intact retinal photoreceptors. *Proc. Natl. Acad. Sci. U.S.A.* 85, 5531–5535.
- Petrig, B.L., Lorenz, B., Cranstoun, S.D., Riva, C.E., 1997. Measurement of leukocyte velocity in macular capillaries by means of a miniaturized blue field simulator: effect of pupil aperture size. *Klinische Monatsblätter Für Augenheilkunde* 210, 305–307.
- Pinhas, A., Dubow, M., Shah, N., Chui, T.Y., Scoles, D., Sulai, Y.N., Weitz, R., Walsh, J.B., Carroll, J., Dubra, A., Rosen, R.B., 2013. In vivo imaging of human retinal microvasculature using adaptive optics scanning light ophthalmoscope fluorescein angiography. *Biomed. Optic Express* 4, 1305–1317.
- Pircher, M., Gotzinger, E., Leitgeb, R., Sattmann, H., Findl, O., Hitznerberger, C.K., 2004. Imaging of polarization properties of human retina in vivo with phase resolved transversal PS-OCT. *Optic Express* 12, 5940–5951.
- Pircher, M., Zawadzki, R.J., 2017. Review of adaptive optics OCT (AO-OCT): principles and applications for retinal imaging. *Invest. Ophthalmol. Vis. Sci.* 58, 2536–2562.
- Platt, B.C., Shack, R., 2001. History and principles of Shack-Hartmann wavefront sensing. *J. Refract. Surg.* 17, S573–S577.
- Plesch, A., Klingbeil, U., Bille, J., 1987. Digital laser scanning fundus camera. *Appl. Optic* 26, 1480–1486.
- Polans, J., Keller, B., Carrasco-Zevallos, O.M., LaRocca, F., Cole, E., Whitson, H.E., Lad, E.M., Farsiu, S., Izatt, J.A., 2017. Wide-field retinal optical coherence tomography with wavefront sensorless adaptive optics for enhanced imaging of targeted regions. *Biomed. Optic Express* 8, 16–37.
- Popovic, Z., Knutsson, P., Thuang, J., Owner-Petersen, M., Sjostrand, J., 2011. Noninvasive imaging of human foveal capillary network using dual-conjugate adaptive optics. *Invest. Ophthalmol. Vis. Sci.* 52, 2649–2655.
- Pourmaras, C.J., Riva, C.E., 2013. Retinal blood flow evaluation. *Ophthalmologica* 229, 61–74.
- Powell, I., 1981. Lenses for correcting chromatic aberration of the eye. *Appl. Optic* 20, 4152–4155.
- Pries, A.R., Neuhaus, D., Gaetgens, P., 1992. Blood-viscosity in tube flow - dependence on diameter and hematocrit. *Am. J. Physiol.* 263, H1770–H1778.
- Pries, A.R., Secomb, T.W., 2005. Microvascular blood viscosity in vivo and the endothelial surface layer. *Am. J. Physiol. Heart Circ. Physiol.* 289, H2657–H2664.
- Prieto, P.M., Vargas-Martin, F., Goelz, S., Artal, P., 2000. Analysis of the performance of the Hartmann-Shack sensor in the human eye. *J. Opt. Soc. Am. a-Opt. Image Sci. Vision* 17, 1388–1398.
- Putnam, N.M., Hofer, H.J., Doble, N., Chen, L., Carroll, J., Williams, D.R., 2005. The locus of fixation and the foveal cone mosaic. *J. Vis.* 5, 632–639.
- Ragazzoni, R., 1996. Pupil plane wavefront sensing with an oscillating prism. *J. Mod. Optic* 43, 289–293.
- Ragunandan, A., Frasier, J., Poonja, S., Roorda, A., Stevenson, S.B., 2008. Psychophysical measurements of referenced and unreferenced motion processing using high-resolution retinal imaging. *J. Vis.* 8, 14 11–11.
- Remky, A., Beausencourt, E., Elsner, A.E., 1996. Angioscotometry with the scanning laser ophthalmoscope. Comparison of the effect of different wavelengths. *Invest. Ophthalmol. Vis. Sci.* 37, 2350–2355.
- Rha, J., Jonnal, R.S., Thorn, K.E., Qu, J.L., Zhang, Y., Miller, D.T., 2006. Adaptive optics flood-illumination camera for high speed retinal imaging. *Optic Express* 14, 4552–4569.
- Riva, C., Benedek, G.B., Ross, B., 1972. Laser Doppler measurements of blood-flow in capillary tubes and retinal arteries. *Invest. Ophthalmol.* 11, 936.
- Riva, C.E., Grunwald, J.E., Petrig, B.L., 1986. Autoregulation of human retinal blood-flow - an investigation with laser Doppler velocimetry. *Invest. Ophthalmol. Vis. Sci.* 27, 1706–1712.
- Riva, C.E., Harino, S., Petrig, B.L., Shonat, R.D., 1992. Laser Doppler flowmetry in the optic-nerve. *Exp. Eye Res.* 55, 499–506.
- Riva, C.E., Harino, S., Shonat, R.D., Petrig, B.L., 1991. Flicker evoked increase in optic-nerve head blood-flow in anesthetized cats. *Neurosci. Lett.* 128, 291–296.
- Rizzoni, D., Agabiti-Rosei, E., 2012. Structural abnormalities of small resistance arteries in essential hypertension. *Internal and Emergency Medicine* 7, 205–212.
- Rizzoni, D., Porteri, E., Duse, S., De Ciuceis, C., Rosei, C.A., La Boria, E., Semeraro, F., Costagliola, C., Sebastiani, A., Danzi, P., Tiberio, G.A.M., Giulini, S.M., Docchio, F., Sansoni, G., Sarkar, A., Rosei, E.A., 2012. Relationship between media-to-lumen ratio of subcutaneous small arteries and wall-to-lumen ratio of retinal arterioles evaluated noninvasively by scanning laser Doppler flowmetry. *J. Hypertens.* 30, 1169–1175.
- Rizzoni, D., Rosei, C.A., De Ciuceis, C., Semeraro, F., Rizzoni, M., Docchio, F., 2018. New methods to study the microcirculation. *Am. J. Hypertens.* 31, 265–273.
- Rodieck, R.W., 1991. The density recovery profile - a method for the analysis of points in the plane applicable to retinal studies. *Vis. Neurosci.* 6, 95–111.
- Roorda, A., Metha, A.B., Lennie, P., Williams, D.R., 2001. Packing arrangement of the three cone classes in primate retina. *Vis. Res.* 41, 1291–1306.
- Roorda, A., Romero-Borja, F., Donnelly, W.J., Queener, H., Hebert, T.J., Campbell, M.C.W., 2002. Adaptive optics scanning laser ophthalmoscopy. *Optic Express* 10, 405–412.
- Roorda, A., Williams, D.R., 1999. The arrangement of the three cone classes in the living human eye. *Nature* 397, 520–522.
- Roorda, A., Zhang, Y.H., Duncan, J.L., 2007. High-resolution in vivo imaging of the RPE mosaic in eyes with retinal disease. *Invest. Ophthalmol. Vis. Sci.* 48, 2297–2303.
- Rossi, E.A., Granger, C.E., Sharma, R., Yang, Q., Saito, K., Schwarz, C., Walters, S., Nozato, K., Zhang, J., Kawakami, T., Fischer, W., Latchney, L.R., Hunter, J.J., Chung, M.M., Williams, D.R., 2017. Imaging individual neurons in the retinal ganglion cell layer of the living eye. *Proc. Natl. Acad. Sci. U.S.A.* 114, 586–591.
- Rossi, E.A., Rangel-Fonseca, P., Parkins, K., Fischer, W., Latchney, L.R., Folwell, M.A., Williams, D.R., Dubra, A., Chung, M.M., 2013. In vivo imaging of retinal pigment epithelium cells in age related macular degeneration. *Biomed. Optic Express* 4, 2527–2539.
- Rossi, E.A., Roorda, A., 2010. The relationship between visual resolution and cone spacing in the human fovea. *Nat. Neurosci.* 13, 156–157.
- Roy, M.S., Klein, R., Janal, M.N., 2011. Retinal venular diameter as an early indicator of progression to proliferative diabetic retinopathy with and without high-risk characteristics in african americans with type 1 diabetes mellitus. *Arch. Ophthalmol.* 129, 8–15.
- Rushton, W.A.H., 1958. Kinetics of cone pigments measured objectively in the living human fovea. *Ann. N. Y. Acad. Sci.* 74 (Article 2), 291–304.
- Rushton, W.A.H., Baker, H.D., 1964. Red/green sensitivity in normal vision. *Vis. Res.* 4, 75–85.
- Sapoznik, K.A., Luo, T., De Castro, A., Sawides, L., Warner, R.L., Burns, S.A., 2018. Enhanced retinal vasculature imaging with a rapidly configurable aperture. *Biomed. Optic Express* 9, 1323–1333.
- Sawides, L., de Castro, A., Burns, S.A., 2017a. The organization of the cone photoreceptor mosaic measured in the living human retina. *Vis. Res.* 132, 34–44.
- Sawides, L., Sapoznik, K.A., de Castro, A., Walker, B.R., Gast, T.J., Elsner, A.E., Burns, S.A., 2017b. Alterations to the foveal cone mosaic of diabetic patients. *Invest. Ophthalmol. Vis. Sci.* 58, 3395–3403.
- Scarinci, F., Nesper, P.L., Fawzi, A.A., 2016. Deep retinal capillary nonperfusion is associated with photoreceptor disruption in diabetic macular ischemia. *Am. J. Ophthalmol.* 168, 129–138.
- Schwarz, C., Sharma, R., Fischer, W.S., Chung, M.N., Palczewska, G., Palczewski, K., Williams, D.R., Hunter, J.J., 2016. Safety assessment in macaques of light exposures for functional two-photon ophthalmoscopy in humans. *Biomed. Optic Express* 7, 5148–5169.
- Scoles, D., Flatter, J.A., Cooper, R.F., Langlo, C.S., Robison, S., Neitz, M., Weinberg, D.V., Pennesi, M.E., Han, D.P., Dubra, A., Carroll, J., 2016. Assessing photoreceptor structure associated with ellipsoid zone disruptions visualized with optical coherence tomography. *Retina-the Journal of Retinal and Vitreous Diseases* 36, 91–103.
- Scoles, D., Sulai, Y.N., Cooper, R.F., Higgins, B.P., Johnson, R.D., Carroll, J., Dubra, A., Stepien, K.E., 2017. Photoreceptor inner segment morphology in best vitelliform macular dystrophy. *Retina-the Journal of Retinal and Vitreous Diseases* 37, 741–748.
- Scoles, D., Sulai, Y.N., Dubra, A., 2013. In vivo dark-field imaging of the retinal pigment epithelium cell mosaic. *Biomed. Optic Express* 4, 1710–1723.
- Scoles, D., Sulai, Y.N., Langlo, C.S., Fishman, G.A., Curcio, C.A., Carroll, J., Dubra, A., 2014. In vivo imaging of human cone photoreceptor inner segments. *Invest. Ophthalmol. Vis. Sci.* 55, 4244–4251.
- Secomb, T.W., 2017. Blood flow in the microcirculation. In: Davis, S.H., Moin, P. (Eds.), *Annual Review of Fluid Mechanics*. vol. 49. pp. 443–461.
- Segiguchi, N., Williams, D.R., Brainard, D.H., 1993. Efficiency in detection of isoluminant and isochromatic interference fringes. *J. Opt. Soc. Am. A* 10, 2118–2133.
- Shack, R.V., Platt, B.C., 1971. Production and use of a lenticular hartmann screen. *J. Opt. Soc. Am.* 61, 656.
- Sharma, R., Williams, D.R., Palczewska, G., Palczewski, K., Hunter, J.J., 2016. Two-photon autofluorescence imaging reveals cellular structures throughout the retina of the living primate eye. *Invest. Ophthalmol. Vis. Sci.* 57, 632–646.
- Shemonski, N.D., Ahmad, A., Adie, S.G., Liu, Y.Z., South, F.A., Carney, P.S., Boppart, S.A., 2014. Stability in computed optical interferometric tomography (Part II): in vivo stability assessment. *Optic Express* 22, 19314–19326.
- Shirai, T., Barnes, T.H., Haskell, T.G., 2000. Adaptive wave-front correction by means of all-optical feedback interferometry. *Optic Lett.* 25, 773–775.
- Shirai, T., Takeno, K., Arimoto, H., Furukawa, H., 2009. Adaptive optics with a liquid-crystal-on-silicon spatial light modulator and its behavior in retinal imaging. *Jpn. J. Appl. Phys.* 48.
- Sincich, L.C., Sabesan, R., Tuten, W.S., Roorda, A., Harmening, W.M., 2016. Functional Imaging of Cone Photoreceptors.
- Sivak, J.G., Mandelman, T., 1982. Chromatic dispersion of the ocular media. *Vis. Res.* 22, 997–1003.
- Smirnov, M.S., 1961. Measurement of the wave aberration of the human eye. *Biofizika* 6, 687–703.
- Soliman, M.K., Sadiq, M.A., Agarwal, A., Sarwar, S., Hassan, M., Hanout, M., Graf, F., High, R., Do, D.V., Nguyen, Q.D., Sepah, Y.J., 2016. High-resolution imaging of parafoveal cones in different stages of diabetic retinopathy using adaptive optics fundus camera. *PLoS One* 11, e0152788.
- Sommer, A., Kues, H.A., Danna, S.A., Arkell, S., Robin, A., Quigley, H.A., 1984. Cross-polarization photography of the nerve-fiber layer. *Arch. Ophthalmol.* 102, 864–869.
- Song, H., Chui, T.Y., Zhong, Z., Elsner, A.E., Burns, S.A., 2011a. Variation of cone photoreceptor packing density with retinal eccentricity and age. *Invest. Ophthalmol. Vis. Sci.* 52, 7376–7384.
- Song, H.X., Chui, T.Y.P., Zhong, Z.Y., Elsner, A.E., Burns, S.A., 2011b. Variation of cone photoreceptor packing density with retinal eccentricity and age. *Invest. Ophthalmol. Vis. Sci.* 52, 7376–7384.
- Song, H.X., Latchney, L., Williams, D., Chung, M.N., 2014. Fluorescence adaptive optics scanning laser ophthalmoscope for detection of reduced cones and

- hyphae autofluorescent spots in fundus albipunctatus. *JAMA Ophthalmol* 132, 1099–1104.
- Song, H.X., Qi, X.F., Zou, W.W., Zhong, Z.Y., Burns, S.A., 2010. Dual electro-optical modulator polarimeter based on adaptive optics scanning laser ophthalmoscope. *Optic Express* 18, 21892–21904.
- Song, H.X., Rossi, E.A., Stone, E., Latchney, L., Williams, D., Dubra, A., Chung, M., 2018. Phenotypic diversity in autosomal-dominant cone-rod dystrophy elucidated by adaptive optics retinal imaging. *Br. J. Ophthalmol.* 102, 136–141.
- Song, H.X., Zhao, Y.M., Qi, X.F., Chui, Y.P.T., Burns, S.A., 2008. Stokes vector analysis of adaptive optics images of the retina. *Optic Lett.* 33, 137–139.
- Spaide, R.F., Fujimoto, J.G., Waheed, N.K., Sadda, S.R., Staurengi, G., 2018. Optical coherence tomography angiography. *Prog. Retin. Eye Res.* 64, 1–55.
- Sredar, N., Fagbemi, O.E., Dubra, A., 2018. Sub-airy confocal adaptive optics scanning ophthalmoscopy. *Translational vision science & technology* 7.
- Srinivasan, V.J., Dubra, A., 2016. Noninvasive imaging of the photoreceptor mosaic response to light stimulation. *Proc. Natl. Acad. Sci. U.S.A.* 113, 12902–12903.
- Stevenson, S.B., Roorda, A., 2005. Correcting for miniature eye movements in high resolution scanning laser ophthalmoscopy. *Ophthalmic Technologies XV* 5688, 145–151.
- Sulai, Y.N., Dubra, A., 2014. Non-common path aberration correction in an adaptive optics scanning ophthalmoscope. *Biomed. Optic Express* 5, 3059–3073.
- Sulai, Y.N., Scoles, D., Harvey, Z., Dubra, A., 2014. Visualization of retinal vascular structure and perfusion with a nonconfocal adaptive optics scanning light ophthalmoscope. *J. Opt. Soc. Am. A* 31, 569–579.
- Sun, C., Wang, J.J., Mackey, D.A., Wong, T.Y., 2009. Retinal vascular caliber: systemic, environmental, and genetic associations. *Surv. Ophthalmol.* 54, 74–95.
- Supriya, D., Shwetha, M., Anupama, K.K., Mathew, K.K., Berendschot, T., Schouten, J., Bharamshetter, R., Naresh, Y.K., Rohit, S., Hegde, B., 2015. Structural and function correlation of cone packing utilizing adaptive optics and micropolymerimetry. *BioMed Res. Int.* 2015, 968672.
- Talcott, K.E., Ratnam, K., Sundquist, S.M., Lucero, A.S., Lujan, B.J., Tao, W., Porco, T.C., Roorda, A., Duncan, J.L., 2011. Longitudinal study of cone photoreceptors during retinal degeneration and in response to ciliary neurotrophic factor treatment. *Invest. Ophthalmol. Vis. Sci.* 52, 2219–2226.
- Tam, J., Dhamdhere, K.P., Tiruveedhula, P., Lujan, B.J., Johnson, R.N., Bearnse, M.A., Adams, A.J., Roorda, A., 2012. Subclinical capillary changes in non-proliferative diabetic retinopathy. *Optom. Vis. Sci.* 89, E692–E703.
- Tam, J., Dhamdhere, K.P., Tiruveedhula, P., Manzanera, S., Barez, S., Bearnse, M.A., Adams, A.J., Roorda, A., 2011a. Disruption of the retinal parafoveal capillary network in type 2 diabetes before the onset of diabetic retinopathy. *Invest. Ophthalmol. Vis. Sci.* 52, 9257–9266.
- Tam, J., Liu, J.F., Dubra, A., Fariss, R., 2016. In vivo imaging of the human retinal pigment epithelial mosaic using adaptive optics enhanced indocyanine green ophthalmoscopy. *Invest. Ophthalmol. Vis. Sci.* 57, 4376–4384.
- Tam, J., Roorda, A., 2011. Speed quantification and tracking of moving objects in adaptive optics scanning laser ophthalmoscopy. *J. Biomed. Optic.* 16, 036002.
- Tam, J., Tiruveedhula, P., Roorda, A., 2011b. Characterization of single-file flow through human retinal parafoveal capillaries using an adaptive optics scanning laser ophthalmoscope. *Biomed. Optic Express* 2, 781–793.
- Tan, W., Wright, T., Rajendran, D., Garcia-Sanchez, Y., Finkelberg, L., Kislak, M., Campbell, M., Westall, C.A., 2015. Cone-photoreceptor density in adolescents with type 1 diabetes. *Invest. Ophthalmol. Vis. Sci.* 56, 6339–6343.
- Tanna, P., Kasilian, M., Strauss, R., Tee, J., Kalitzeos, A., Tarima, S., Visotcky, A., Dubra, A., Carroll, J., Michaelides, M., 2017. Reliability and repeatability of cone density measurements in patients with stargardt disease and RPGR-associated retinopathy. *Invest. Ophthalmol. Vis. Sci.* 58, 3608–3615.
- Thaung, J., Knutsson, P., Popovic, Z., Owner-Petersen, M., 2009. Dual-conjugate adaptive optics for wide-field high-resolution retinal imaging. *Optic Express* 17, 4454–4467.
- Thibos, L.N., Bradley, A., 1997. Use of liquid-crystal adaptive-optics to alter the refractive state of the eye. *Optom. Vis. Sci.: official publication of the American Academy of Optometry* 74, 581–587.
- Timberlake, G.T., Mainster, M.A., Peli, E., Augliere, R.A., Essock, E.A., Arend, L.E., 1986. Reading with a macular scotoma I. Retinal location of scotoma and fixation area. *Invest. Ophthalmol. Vis. Sci.* 27, 1137–1147.
- Timberlake, G.T., Mainster, M.A., Webb, R.H., Hughes, G.W., Trempe, C.L., 1982. Retinal localization of scotomata by scanning laser ophthalmoscopy. *Invest. Ophthalmol. Vis. Sci.* 22, 91–97.
- Tuten, W.S., Harmening, W.M., Sabesan, R., Roorda, A., Sincich, L.C., 2017. Spatiochromatic interactions between individual cone photoreceptors in the human retina. *J. Neurosci.* 37, 9498–9509.
- Twietmeyer, K.M., Chipman, R.A., Elsner, A.E., Zhao, Y., VanNasdale, D., 2008. Mueller matrix retinal imager with optimized polarization conditions. *Optic Express* 16, 21339–21354.
- Van Bloklund, G.J., Verhelst, S.C., 1987. Corneal polarization in the living human eye explained with a biaxial model. *J. Opt. Soc. Am. A* 4, 82–90.
- Van Loo Jr., J.A., Enoch, J.M., 1975. The scotopic Stiles-Crawford effect. *Vis. Res.* 15, 1005–1009.
- VanNasdale, D.A., Elsner, A.E., Hobbs, T., Burns, S.A., 2011. Foveal phase retardation changes associated with normal aging. *Vis. Res.* 51, 2263–2272.
- VanNasdale, D.A., Elsner, A.E., Kohne, K.D., Peabody, T.D., Malinovsky, V.E., Haggerty, B.P., Weber, A., Clark, C.A., 2012. Foveal localization in non-exudative AMD using scanning laser polarimetry. *Optom. Vis. Sci.* 89, 667–677.
- Vdovin, G., Sarro, P.M., 1995. Flexible mirror micromachined in silicon. *Appl. Optic.* 34, 2968–2972.
- Vincent, A., Wright, T., Garcia-Sanchez, Y., Kislak, M., Campbell, M., Westall, C., Heon, E., 2013. Phenotypic characteristics including in vivo cone photoreceptor mosaic in KCNV2-related "cone dystrophy with supernormal rod electroretinogram". *Invest. Ophthalmol. Vis. Sci.* 54, 898–908.
- Vogel, C.R., Arathorn, D.W., Roorda, A., Parker, A., 2006. Retinal motion estimation in adaptive optics scanning laser ophthalmoscopy. *Optic Express* 14, 487–497.
- Vorontsov, M.A., Sivokon, V.P., 1998. Stochastic parallel-gradient-descent technique for high-resolution wave-front phase-distortion correction. *J. Opt. Am. a-Opt. Image Sci. Vision* 15, 2745–2758.
- Wade, A.R., Fitzke, F.W., 1998. A fast, robust pattern recognition system for low light level image registration and its application to retinal imaging. *Optic Express* 3, 190–197.
- Walsh, G., Charman, W.N., 1985. Measurement of the axial wavefront aberration of the human eye. *Ophthalmic Physiol. Optic.: J. Brit. College Ophthalmic Opt. (Optom.)* 5, 23–31.
- Walsh, G., Charman, W.N., Howland, H.C., 1984. Objective technique for the determination of monochromatic aberrations of the human eye. *J. Opt. Soc. Am. A* 1, 987–992.
- Webb, R.H., 1984. Optics for laser rasters. *Appl. Optic.* 23, 3680–3683.
- Webb, R.H., 1996. Confocal optical microscopy. *Rep. Prog. Phys.* 59, 427–471.
- Webb, R.H., Albanese, M.J., Zhou, Y.P., Bifano, T., Burns, S.A., 2004. Stroke amplifier for deformable mirrors. *Appl. Optic.* 43, 5330–5333.
- Webb, R.H., Hughes, G.W., Delori, F.C., 1987. Confocal scanning laser ophthalmoscope. *Appl. Optic.* 26, 1492–1499.
- Webb, R.H., Hughes, G.W., Pomerantz, O., 1980. Flying spot tv ophthalmoscope. *Appl. Optic.* 19, 2991–2997.
- Webb, R.H., Penney, C.M., Thompson, K.P., 1992. Measurement of ocular wavefront distortion with a spatially resolved refractometer. *Appl. Optic.* 31, 3678–3686.
- Webb, R.H., Rogomentich, F.J., 1995. Microlaser microscope using self-detection for confocality. *Optic Lett.* 20, 533–535.
- Weber, A., Cheney, M.C., Smithwick, Q.Y.J., Elsner, A.E., 2004. Polarimetric imaging and blood vessel quantification. *Optic Express* 12, 5178–5190.
- Wells-Gray, E.M., Choi, S.S., Bries, A., Doble, N., 2016. Variation in rod and cone density from the fovea to the mid-periphery in healthy human retinas using adaptive optics scanning laser ophthalmoscopy. *Eye* 30, 1135–1143.
- Wells-Gray, E.M., Choi, S.S., Zawadzki, R.J., Finn, S.C., Greiner, C., Werner, J.S., Doble, N., 2018. Volumetric imaging of rod and cone photoreceptor structure with a combined adaptive optics-optical coherence tomography-scanning laser ophthalmoscope. *J. Biomed. Optic.* 23, 1–15.
- Wen, L.H., Ping, Y., Wang, S., Liu, W.J., Chen, S.Q., Bing, X., 2018. A high speed model-based approach for wavefront sensorless adaptive optics systems. *Optic Laser Technol.* 99, 124–132.
- Westheimer, G., 1960. Modulation thresholds for sinusoidal light distributions on the retina. *Journal of Physiology-London* 152, 67–74.
- Wilk, M.A., Dubis, A.M., Cooper, R.F., Summerfelt, P., Dubra, A., Carroll, J., 2017. Assessing the spatial relationship between fixation and foveal specializations. *Vis. Res.* 132, 53–61.
- Williams, D.R., 1985. Visibility of interference fringes near the resolution limit. *J. Opt. Soc. Am. A* 2, 1087–1093.
- Wilson, T., Carlini, A.R., 1987. Size of the detector in confocal imaging-systems. *Optic Lett.* 12, 227–229.
- Winn, B., Whitaker, D., Elliott, D.B., Phillips, N.J., 1994. Factors affecting light-adapted pupil size in normal human subjects. *Invest. Ophthalmol. Vis. Sci.* 35, 1132–1137.
- Witt, N., Wong, T.Y., Hughes, A.D., Chaturvedi, N., Klein, B.E., Evans, R., McNamara, M., Thom, S.A.M., Klein, R., 2006. Abnormalities of retinal microvascular structure and risk of mortality from ischemic heart disease and stroke. *Hypertension* 47, 975–981.
- Wolf, S., Arend, O., Reim, M., 1994. Measurement of retinal hemodynamics with scanning laser ophthalmoscopy: reference values and variation. *Surv. Ophthalmol.* 38 (Suppl. 1), S95–S100.
- Wolf, S., Jung, F., Kiesewetter, H., Korber, N., Reim, M., 1989. Video fluorescein angiography - method and clinical-application. *Graefes Arch. Clin. Exp. Ophthalmol.* 27, 145–151.
- Wolfgang, J.I., Chung, M., Carroll, J., Roorda, A., Williams, D.R., 2006. High-resolution retinal imaging of cone-rod dystrophy. *Ophthalmology* 113, 1014–1019.
- Wong, K.S.K., Jian, Y.F., Cua, M., Bonora, S., Zawadzki, R.J., Sarunic, M.V., 2015. In vivo imaging of human photoreceptor mosaic with wavefront sensorless adaptive optics optical coherence tomography. *Biomed. Optic Express* 6, 580–590.
- Wong, T.Y., Klein, R., Sharrett, A.R., Duncan, B.B., Couper, D.J., Tielsch, J.M., Klein, B.E.K., Hubbard, L.D., 2002. Retinal arteriolar narrowing and risk of coronary heart disease in men and women - the atherosclerosis risk in communities study. *Jama-Journal of the American Medical Association* 287, 1153–1159.
- Woog, K., Legras, R., 2018. Visual resolution and cone spacing in the nasal and inferior retina. *Ophthalmic Physiol. Optic.* 38, 66–75.
- Xu, H.Z., Le, Y.Z., 2011. Significance of outer blood-retina barrier breakdown in diabetes and ischemia. *Invest. Ophthalmol. Vis. Sci.* 52, 2160–2164.
- Xue, B., Choi, S.S., Doble, N., Werner, J.S., 2007. Photoreceptor counting and montaging of en-face retinal images from an adaptive optics fundus camera. *J. Opt. Soc. Am. a-Opt. Image Sci. Vision* 24, 1364–1372.
- Yamagishi, S., Imaizumi, T., 2005. Diabetic vascular complications: pathophysiology, biochemical basis and potential therapeutic strategy. *Curr. Pharmaceut. Des.* 11, 2279–2299.
- Yang, Q., Zhang, J., Nozato, K., Saito, K., Williams, D.R., Roorda, A., Rossi, E.A., 2014. Closed-loop optical stabilization and digital image registration in adaptive optics scanning light ophthalmoscopy. *Biomed. Optic Express* 5, 3174–3191.
- Yang, Q.A., Arathorn, D.W., Tiruveedhula, P., Vogel, C.R., Roorda, A., 2010. Design of an integrated hardware interface for AOSLO image capture and cone-targeted stimulus delivery. *Optic Express* 18, 17841–17858.
- Yazdanfar, S., Rollins, A.M., Izatt, J.A., 2003. In vivo imaging of human retinal flow

- dynamics by color Doppler optical coherence tomography. *Arch. Ophthalmol.* 121, 235–239.
- Yellott, J.I., 1982. Spectral analysis of spatial sampling by photoreceptors: topological disorder prevents aliasing. *Vis. Res.* 22, 1205–1210.
- Yu, Y., Zhang, T., Meadway, A., Wang, X., Zhang, Y., 2015. High-speed adaptive optics for imaging of the living human eye. *Optic Express* 23, 23035–23052.
- Zaleska-Zmijewska, A., Piatkiewicz, P., Smigielska, B., Sokolowska-Oracz, A., Wawrzyniak, Z.M., Romaniuk, D., Szaflik, J., Szaflik, J.P., 2017. Retinal photoreceptors and microvascular changes in prediabetes measured with adaptive optics (rtx1 (TM)): a case-control study. *J. Diab. Res.* <https://doi.org/10.1155/2017/4174292>.
- Zawadzki, R.J., Capps, A.G., Kim, D.Y., Panorgias, A., Stevenson, S.B., Hamann, B., Werner, J.S., 2014. Progress on developing adaptive optics-optical coherence tomography for in vivo retinal imaging: monitoring and correction of eye motion artifacts. *IEEE J. Sel. Top. Quant. Electron.* 20, 12.
- Zawadzki, R.J., Jones, S.M., Olivier, S.S., Zhao, M.T., Bower, B.A., Izatt, J.A., Choi, S., Laut, S., Werner, J.S., 2005. Adaptive-optics optical coherence tomography for high-resolution and high-speed 3D retinal in vivo imaging. *Optic Express* 13, 8532–8546.
- Zhang, J., Yang, Q., Saito, K., Nozato, K., Williams, D.R., Rossi, E.A., 2015a. An adaptive optics imaging system designed for clinical use. *Biomed. Optic Express* 6, 2120–2137.
- Zhang, T.J., Godara, P., Blanco, E.R., Griffin, R.L., Wang, X.L., Curcio, C.A., Zhang, Y.H., 2015b. Variability in human cone topography assessed by adaptive optics scanning laser ophthalmoscopy. *Am. J. Ophthalmol.* 160, 290–300.
- Zhang, X., Bradley, A., Thibos, L.N., 1991a. Achromatizing the human eye: the problem of chromatic parallax. *J. Opt. Soc. Am. A* 8, 686–691.
- Zhang, X.X., Thibos, L.N., Bradley, A., 1991b. Relation between the chromatic difference of refraction and the chromatic difference of magnification for the reduced eye. *Optom. Vis. Sci.: Off. Publ. Am. Acad. Optom.* 68, 456–458.
- Zhang, Y., Rha, J.T., Jonnal, R.S., Miller, D.T., 2005. Adaptive optics parallel spectral domain optical coherence tomography for imaging the living retina. *Optic Express* 13, 4792–4811.
- Zhang, Y.H., Poonja, S., Roorda, A., 2006. MEMS-based adaptive optics scanning laser ophthalmoscopy. *Optic Lett.* 31, 1268–1270.
- Zhang, Y.H., Wang, X.L., Rivero, E.B., Clark, M.E., Witherspoon, C.D., Spaide, R.F., Girkin, C.A., Owsley, C., Curcio, C.A., 2014. Photoreceptor perturbation around subretinal drusenoid deposits as revealed by adaptive optics scanning laser ophthalmoscopy. *Am. J. Ophthalmol.* 158, 584–596.
- Zhong, Z.Y., Huang, G., Chui, T.Y.P., Petrig, B.L., Burns, S.A., 2012. Local flicker stimulation evokes local retinal blood velocity changes. *J. Vis.* 12, 3.
- Zhong, Z.Y., Petrig, B.L., Qi, X.F., Burns, S.A., 2008. In vivo measurement of erythrocyte velocity and retinal blood flow using adaptive optics scanning laser ophthalmoscopy. *Optic Express* 16, 12746–12756.
- Zhong, Z.Y., Song, H.X., Chui, T.Y.P., Petrig, B.L., Burns, S.A., 2011. Noninvasive measurements and analysis of blood velocity profiles in human retinal vessels. *Invest. Ophthalmol. Vis. Sci.* 52, 4151–4157.
- Zhou, X.L., Bedggood, P., Bui, B., Nguyen, C.T.O., He, Z., Metha, A., 2015. Contrast-based sensorless adaptive optics for retinal imaging. *Biomed. Optic Express* 6, 3577–3595.
- Zommer, S., Ribak, E.N., Lipson, S.G., Adler, J., 2006. Simulated annealing in ocular adaptive optics. *Optic Lett.* 31, 939–941.
- Zou, W., Qi, X., Burns, S.A., 2008. Wavefront-aberration sorting and correction for a dual-deformable-mirror adaptive-optics system. *Opt. Lett.* 33, 2602–2604.
- Zou, W.Y., Qi, X.F., Burns, S.A., 2011. Woofer-tweeter adaptive optics scanning laser ophthalmoscopic imaging based on Lagrange-multiplier damped least-squares algorithm. *Biomed. Optic Express* 2, 1986–2004.